SAPIENZA
UNIVERSITÀ DI ROMA

Facoltà di Scienze Matematiche, Fisiche e Naturali
Dipartimento di Scienze della Terra
Dottorato di Ricerca in Scienze della Terra
XXI ciclo

FROM THE GLOBAL SCALE TO THE MEDITERRANEAN PLATE KINEMATICS

A DISSERTATION FOR THE DEGREE OF
DOCTOR OF PHILOSOPHY
FIELD IN GEODYNAMICS AND GEOPHYSICS

FEDERICA RIGUZZI

NOVEMBER 2008

SAPIENZA
UNIVERSITÀ DI ROMA

Ph.D. Thesis
From the global scale to the Mediterranean kinematics

With the advising of
Prof. Carlo Doglioni

Referees
Prof. Maurizio Battaglia
Prof. Fernando Sansò

Examiners
Prof. Barbara Betti
Prof. Maria Marsella
Prof. Susanna Zerbini

The research described in this thesis was carried out at
Department of Earth Sciences
La Sapienza University of Rome
P.le A. Moro 5
00185 Rome, Italy
and
Istituto Nazionale di Geofisica e Vulcanologia
via di Vigna Murata 605
00143 Rome, Italy

For further information
riguzzi@ingv.it

Theory is when we know everything but nothing works.
Practice is when everything works but no one knows why.
We have combined theory and practice:
nothing works and no one knows why!
(A. Maley, 1991)

… so even though we face the difficulties of today and tomorrow,
I still have a dream!
(M. L. King, 1963)

Contents

Abstract

Plate motions with respect to the mantle represent the most direct evidence to understand the origin of plate tectonic processes. The research here described has the aim to improve the knowledge on the global scale plate kinematics in "absolute" reference frames, or better, relative to the mantle, incorporating both geological–geophysical and space geodesy data. Geophysical and geological signatures of subduction and rift zones independently show a global polarity of current plate motions, suggesting a west-ward displacement of the whole lithosphere relative to the underlying mantle. We analytically modeled this tectonic pattern in a suitable selected hotspot framework, taking into account variable depths of the hotspot source, obtaining new plate angular velocities and their uncertainties, by least squares inversion. Then, we focused our attention on the Italian area estimating the velocity field from continuous GPS observations both relative to Eurasia, and relative to the mantle, applying the global model previously estimated. However, the presence of the Apennine subduction, having more or less the same extent of the investigated area, makes locally less reliable our global model. Consequently, we applied a simple kinematic model to estimate the rates and spatial pattern of the subduction along the Apennines. The variable rates inferred after our analysis, better reconcile if the subduction process is conceived as a passive rather than active feature. Then, the analysis came back again to the global scale and to the basic argument if plates are passively riding along on the top of a mantle convection cell, or whether the plates themselves are active drivers. On the other hand, if plate motion occurs as an ordered undulated west-directed flow, the net-rotation of the lithosphere emerges as a passive process active at global scale, and then, it can be driven only by external forces. Thus, the last part of this research has been dedicated to find the experimental evidences connecting the tectonic processes to the Earth's rotation and the tidal drag.

Introduction

The kinematics of the lithosphere constitutes a crucial constraint on its dynamics and on the kinematics and dynamics of the deeper solid Earth. Thus, the determination of plate motion has been a major research area since the formulation of plate tectonics (Chapter 1).

The recent advent of space geodesy constitutes a bridge between geological and geophysical researches, useful for modelling the lithosphere kinematics in suitable reference frames (Chapter 2). The main difficulty in describing plate kinematics is the choice of a reference system useful for geodynamics. Surface observations are mostly relative by nature, consequently relative plate motion models are estimated in reference frames anchored to the lithosphere. This means that the rotation vectors may be expressed with respect to plate pairs, with respect to one plate, or ultimately, with respect to the mean lithosphere.

In contrast, there is not a direct way to observe the so called absolute motions, the motions of plates with respect to the mantle, so that they can be only indirectly inferred by geologic evidences.

The classical definition of absolute plate kinematic models is based on the fact that it is sufficient to know with enough precision the absolute motion of one plate taken as reference, to obtain the absolute motion of all the other plates. To define these models it is possible following two different approaches: the first is based on the mechanical composition of the known relative motion between adjacent plates, imposing the closure conditions; the second, by a joint estimation of the kinematic unknowns and their statistical errors based on the least squares principle (Chapter 3). Following this last direction, we performed the inversion introducing the GPS velocities as known array and some tectonic features as constraints. The first constraint is the motion (rate and azimuth) of the Pacific plate with respect to the deep mantle. The second is based on the continuity conditions of the Eulerian equators across the plate boundaries, which provide an analytical representation of the westward drift of lithosphere.

Then, we focus our attention on the Italian area dominated by the interaction between the Eurasian, African and Adriatic plates along the

Apennines belt. We have estimated the velocity field from continuous GPS observations in the time interval 2003-2007 (Chapter 4). The GPS sites were installed by different institutions and for different purposes, they cover the whole country with a mean inter-site distance of about 60 km and provide a valuable source of data to map the present day kinematics of the region. Velocities are estimated both relative to Eurasia, and relative to the mantle, applying the global model previously estimated. This last representation is not completely satisfactory, since the directions of absolute motions do not match with the directions of mantle flow inferred by seismological evidences.

Since the Apennine subduction is an important feature having more or less the same scale of the investigated area, we believe not reliable applying the global model. Consequently, through a simple kinematic model, we have estimated the rates and spatial pattern of the subduction rates along the Apennines, keeping as reference the Corsica-Sardinia block, coherently moving as the Eurasian plate. We identify at least four different, independently moving, microplates, i.e., the Adriatic (diverging and internally segmented), Ionian, Sicilian and African (converging) plates with different subduction rates. These different patterns better reconcile if the subduction process is conceived as a passive feature controlled by the far field plate velocities and the relative "eastward" mantle flow acting on a disrupted slab.

Following our global model, plate motion occurs as an ordered undulated flow along which all the plates move at different velocities having a west-directed component. Then, the net-rotation of the lithosphere emerges as a process at global scale that cannot be easily interpreted as simply due to a balance of forces internal to the solid Earth. On the other hand, if we consider all the possible mechanisms generated within the Earth, nobody is able to account for a westward drift of the lithosphere. The argument is basically whether the plates are passively riding along on the top of a mantle convection cell, or whether the plates themselves are active drivers, dragging along with them the mantle below. The kinematic observations across subduction belts, together with other evidences reported in several papers, casts serious doubts on the slab negative buoyancy and mantle convection as the primary driving mechanisms of plate motions.

In our opinion, the two most compelling candidates acting at global scale are the Earth's rotation and the tidal drag. If plate kinematics is regulated by a combined action of the forces connected with these two processes, a signature should be evidenced in global tectonic processes too. Consequently, we have dedicated the last section of this dissertation (Chapter 5), to find

experimental evidences confirming our hypothesis. We have shown that the global seismicity depends on latitude and correlates with the decadal oscillations of the excess length of day (LOD). The solid Earth's budget seems to supply an adequate energy source to plate tectonics from the rotation's deceleration that could trigger the "westward" drift of the lithosphere. The geographical distribution of geological and geophysical asymmetric signatures along the undulated westerly polarized flow of plate motions occurs within the same latitude range of the maximum tidal action.

We are aware that these arguments alone do not unravel the questions regarding the causes and the engine that maintains active plate tectonics, but they can represent a first step to approach the problem.

Only the formulation of analytic and realistic models matching an amount of observations rather different by nature, can really give alternative answers on the plate tectonics mechanism.

1 Plate Tectonics

1.1 Introduction

The advent of the space geodesy techniques has widely increased the spectrum of Earth's science researches, reaching significance comparable to the contribution provided by the first seismological, paleomagnetic, marine geophysics and continental geology observations in developing a consistent plate tectonic theory. All these techniques contributed step by step to renew substantially the Earth sciences, opening the sight to a modern geodynamics.

The kinematics of the lithosphere constitutes a crucial constraint on its dynamics and on the kinematics and dynamics of the deeper solid Earth. Thus, the determination of plate motion has been a major research area since the formulation of plate tectonics.

Until the 1960s, before the diffusion of space geodesy, plate kinematic models were essentially based on the observation of relative motions detected across plate boundaries. This fact had two main limitations: the first is that plate boundaries suffer of deformations, then extrapolating a rigid plate motion only from boundary conditions has been a weak assumption; second, the data sets were composed by a mixture of observation referred to time intervals significantly different, from geologic to present day scales.

However, in spite of these limitations, the first plate motion models were not so far from current models and provided the basic constraints to several tectonic studies (see for instance DeMets et al., 1990; Forsyth and Uyeda, 1975).

Space geodesy techniques have accuracies useful to detect the motion between sites located on the Earth's surface even at great distances and belonging to different plates and, nowadays, within a few years of observations it has been possible to give answers to the main classical geodynamic questions:

- far from deformation area current and past plate motion models are in good agreement (Smith et al., 1994);
- the plates internal rigidity is an acceptable approximation when modelling global scale plate kinematics (Stein, 1993)

- the motion and the deformation rates along plate boundaries can be easily estimated (Kreemer et al., 2003).

Under this light, the advent of space geodesy constitutes a bridge between geological and geophysical researches, useful for modelling the lithosphere kinematics in suitable reference frames.

1.2 Continental Drift

The modern plate tectonics bases its origins on the theory of continental drift proposed by Alfred Wegener in 1912 and expanded in 1915 with the book *The Origin of Continents and Oceans*. He suggested that the continents once formed a single land mass which had drifted apart and separated in continents floating on a denser basaltic material. The idea of Wegener originated from a mosaic of paleo-topographical, climatologic and fossils evidences. However, he was not taken seriously by many geologists, who pointed out that there was no apparent mechanism for continental drift (Wegener, 1915; Holmes, 1928).

Since 1940 and after the II world war, using devices originally designed to identify the Russian submarines during the *cold war* period, researches on the seafloor topography (Ewing et al., 1964) and residual magnetism were extensively carried out. In this period the definition of the topographic shape of ridges and the discovery of the symmetric magnetic anomalies measured across them, reopened the discussion about the motion of continents. The process of the sea–floor spreading was interpreted as a consequence of the continental drift: as the continents move apart, new sea–floor material rise from the mantle along the mid-ocean ridges to fill the vacancy (Hess, 1962; Vine and Matthews, 1963).

Since the beginning of the century, the discovery of the radioactive decay (Rutherford, 1905a, b) and the consequent possibility to infer the rock ages from the isochrones of the initial isotopic rates, allowed to define the first temporal scale of the Earth's magnetic field (Cox et al., 1963) and then to interpret the symmetrical stripes around the crests of the mid-ocean ridges as geological clock records useful to estimate the plate opening rate across the ridges (Vine, 1966).

At the same time, during the 20th century, the seismic instrument improvements and the diffusion of large global standardized networks allowed more precise earthquake locations. It was possible to know that the occurrence of seismic events was mainly concentrated along narrow belts, the

oceanic trenches and spreading ridges, evidencing the fragmentation of the Earth's surface into plates (Gutenberg and Richter, 1942, 1954).

The identification of the Middle Atlantic Ridge with the process of seafloor spreading, the island arc subduction in the Aleutian Islands (Coats, 1962) and the spatial pattern of global seismicity, have posed the experimental bases to renew the original Wegener's idea of continental drift into the modern theory of Plate Tectonics.

From the 1960s, this theory rapidly developed thanks to numerous innovative papers, adding important pieces to the mosaic: the introduction of constraints to the plate motion on a flat Earth (Wilson, 1965); the hypothesis of Earth's surface composed by 12 rigid plates moving relative to each other (Morgan, 1967, talk at the annual AGU conference); the link between seismic slip vectors and rigid plate motion on a sphere (McKenzie and Parker, 1967); the rheological stratification of the Earth's outer shells (McKenzie, 1967; Oliver and Isacks, 1967); the first complete model based on 6 major plates with their relative motions (Le Pichon, 1968).

During this period, the theory was successfully developed thanks to the multidisciplinary approach based on both geological and geophysical observations, thus becoming the unifying factor in the study of geology and geophysics.

1.3 Plate tectonics

Plate tectonics is a theory according to which the Earth's outer shells are composed by the lithosphere, comprising the crust and the uppermost rigid part of the mantle, overlapping the asthenosphere, characterized by low values of viscosity and rigidity (shear strength).

The lithosphere is broken in tectonic plates moving on the asthenosphere with different relative velocities. The number and classification of tectonic plates is currently matter of debate; there is agreement on the identification of the largest 15 (Figure 1.1), whereas discussion is open if minor blocks can be identified as microplates, entities with their own kinematics (Figure 1.2), or as diffuse margins of deformation between major plates (Kreemer et al., 2000; Bird, 2003; Cuffaro and Jurdy, 2006 and references therein).

The seven major plates account for 94% of the surface area of the Earth (Table 1.1, Anderson, 2007).

The plates move around on the Earth's surface and interact with the near plates along their margins. The relative motions may reach several cm/yr, so

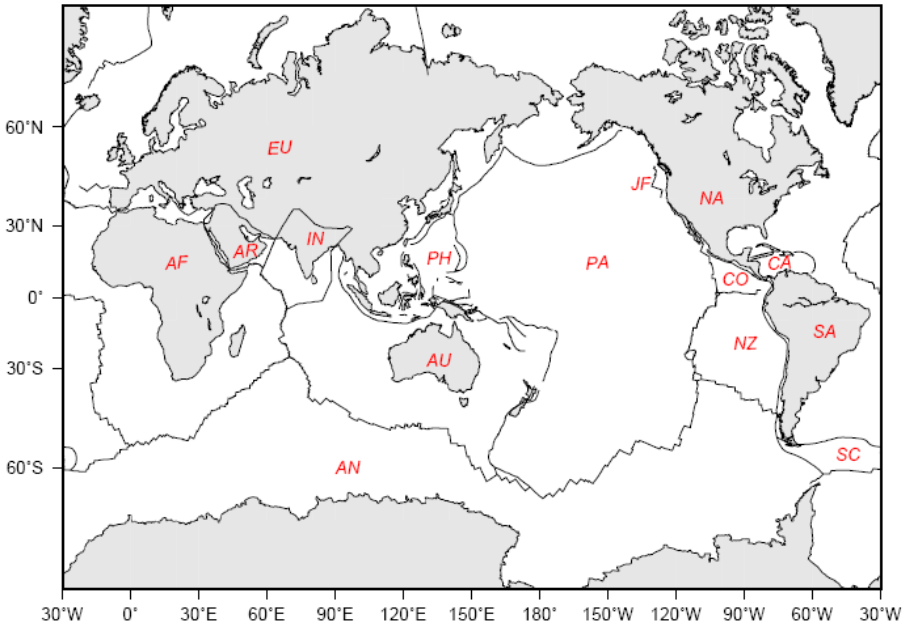

Figure 1.1: The lithosphere is composed by 15 main plates: AF (Africa), AN (Antarctica), AR (Arabia), AU (Australia), CA (Caribbean), CO (Cocos), EU (Eurasia), IN (India), JF (Juan De Fuca), NA (North America), NZ (Nazca), PA (Pacific), PH (Philippine), SA (South America), SC (Scotia).

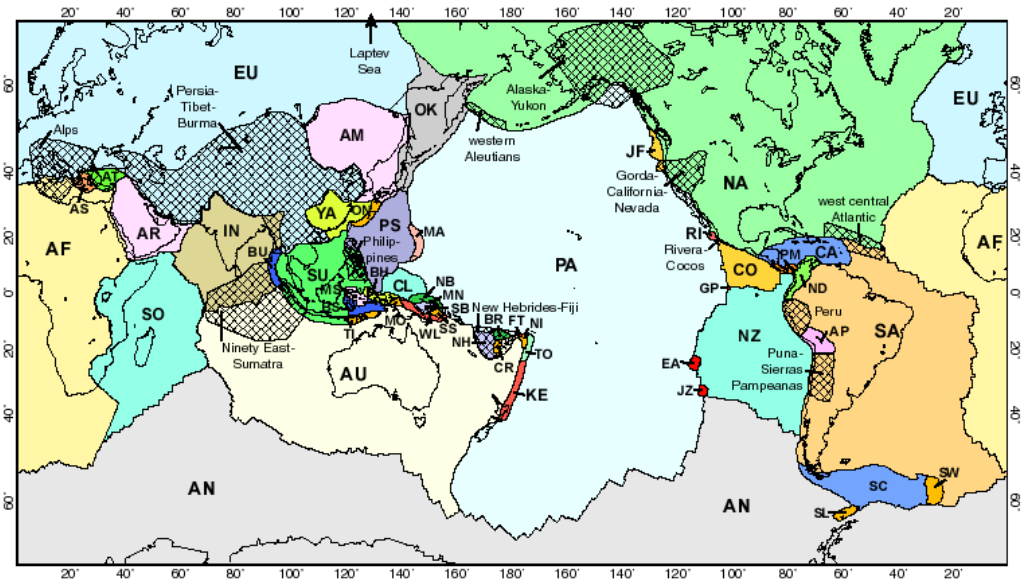

Figure 1.2: The model PB2002 lists 52 plates. The cross-hatched areas are orogens, diffuse zones of deformation (from Bird, 2003).

they are associated with volcanism, seismic activity (Figure 1.3) and deformations; however these effects are in general limited to a narrow band near the contact zones.

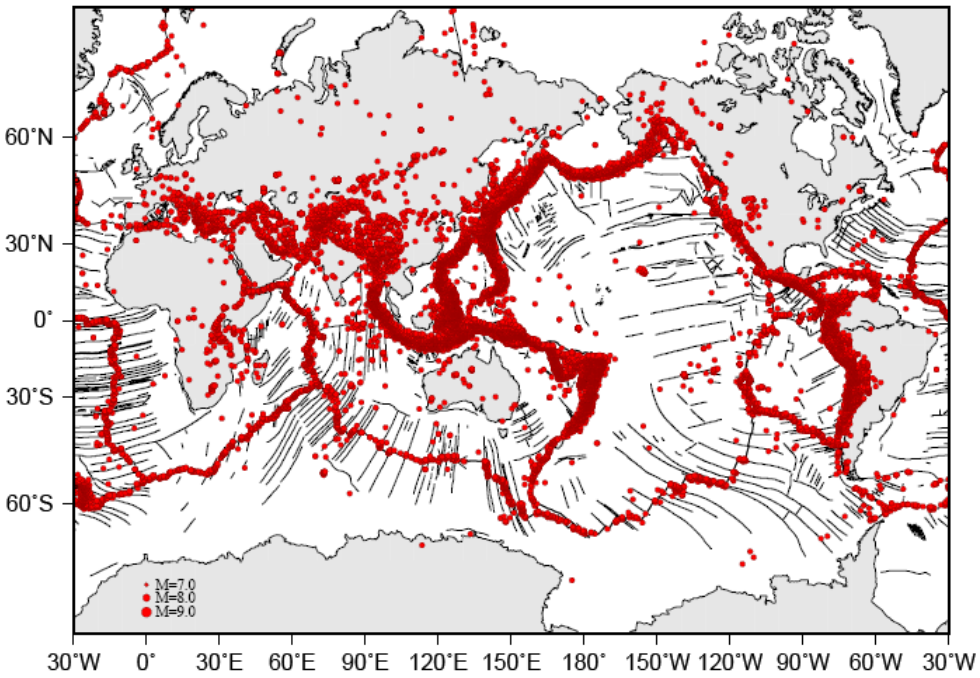

Figure 1.3: Seismic activity is mainly concentrated along plate boundaries, as shown in this map of earthquakes with magnitude M≥5.0; (NEIC seismic catalogue, 1973-2007.

There are three types of plate boundaries (Figure 1.4): convergent, where the plates are colliding and the lithosphere is consumed (trenches, subductions); divergent, where the plates are spreading apart and new lithosphere is accreted from mantle material (continental rifts, oceanic ridges); and conservative, where the lithosphere is not destroyed nor created, these are transform faults (like S. Andreas, Aqaba-Levant).

Some plates are shrinking, others are growing (Table 1.1, Anderson, 2007), so that the plate mosaic changes slowly and continuously configuration; plate tectonics is ultimately the representation of a global engine of recycling Earth's outer materials, up to down and down to up, over geological times.

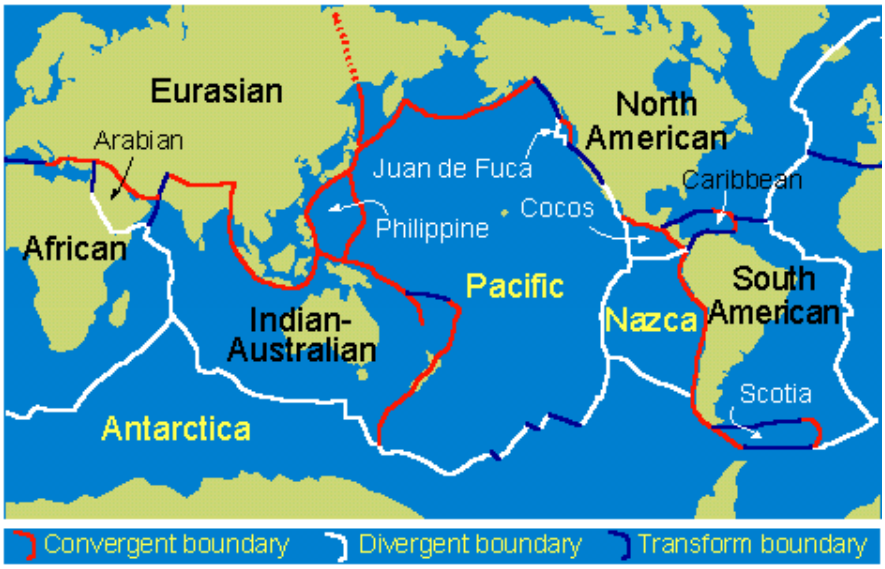

Figure 1.4: Schematic map of the different types of plate boundaries: convergent, red; conservative, blu; divergent, white (from http://www.mhhe.com/earthsci/geology/).

Table 1.1: Plate life

Plate	Area ($x10^6$ km^2)	Growth rate (km^2/100yr)
PA	108.0	-52
AF	79.0	30
EU	69.0	-6
IN-AU	60.0	-35
NA	60.0	9
AN	59.0	55
SA	41.0	13
NZ	15.0	-7
AR	4.9	-2
CA	3.8	0
CO	2.9	-4
PH	5.0	-1
Total	507.6	0

This process is well evidenced by the researches about the age of oceanic lithosphere and spreading rates (Figure 1.5). Recently, The Ionian Sea and the east Mediterranean basins have been identified as the oldest preserved in-situ ocean floor, ranging in age from about 270 Ma (Late Permian) to 230 Ma (Middle Triassic) (Müller et al., 2008).

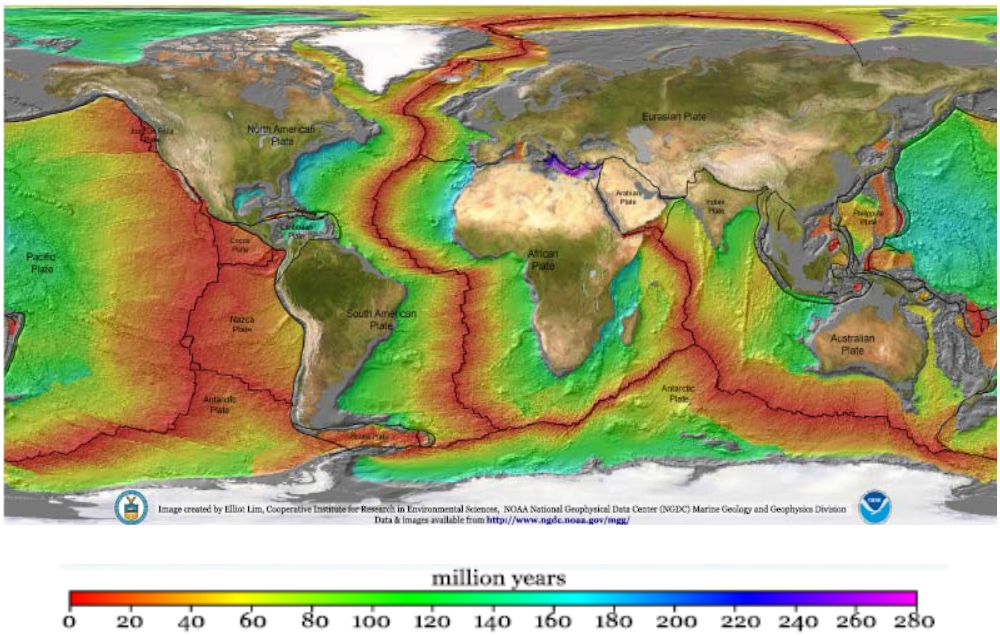

Figure 1.5: The recent map of the oceanic lithosphere age (from Müller et al., 2008).

1.4 Plate kinematics

The definition of plate kinematic models relies on the Euler theorem formulated by Leonhard Euler in the second half of XVIII century. According to it, every displacement of a rigid body in which even a single point is fixed, is rotational. As particular application, the motion of a plate on a sphere (Earth's approximated shape) may be represented by a rotation of the body around a fixed axis passing through the centre of the sphere.

Present–day plate motions are rotations about instantaneous rotation poles, with instantaneous angular velocities, that can be analytically represented both in spherical and geocentric Cartesian coordinate systems.

The rotation axis cuts the Earth's surface in two points called the rotation poles (or the Euler poles). Every plate displacement is characterized by a rotation about an Euler pole with an angular velocity $\vec{\omega}$. The vector $\vec{\omega}$ lies on the rotation axis and the sign convention used is that rotation is positive if it is right–handed: viewed from the axis itself the plate turns about counter clockwise. Thus a rotation pole is positive and the other is negative (anti–pole).

Every plate point moves with a linear velocity $\vec{V}$, tangent to the Earth's surface, given from

$\vec{V} = \vec{\omega}_p \times \vec{R}$, modulus $V = \omega_p R \sin\Delta$, where $\vec{V}$ is the linear velocity, $\vec{\omega}_p$ is the angular rate, $\vec{R}$ is the Earth's radius, and Δ is the angular distance between the Euler pole and a single plate point. The velocity reaches its maximum value $V = \omega_p R$ for $\Delta = \pi/2$; the line along which the tangential velocity is always maximum is called Eulerian equator.

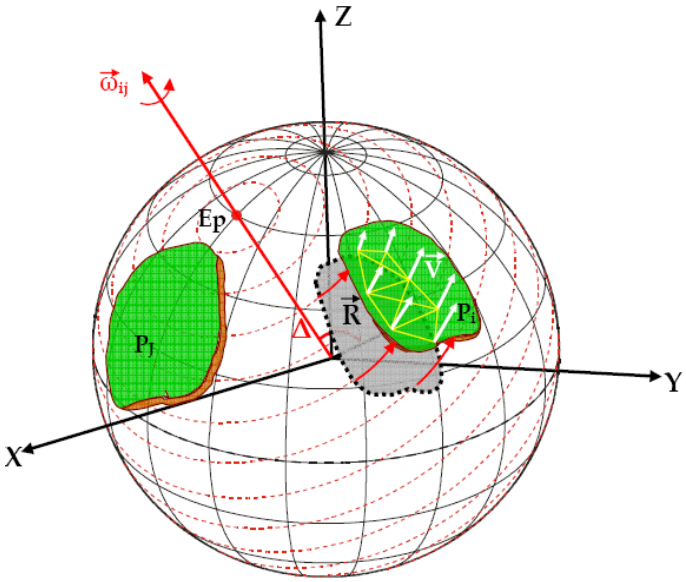

Figure 1.6: Relative plate motions. The plate P_i is stated fixed and the plate P_j rotates around the Euler pole (Ep) with a relative rotation vector $\vec{\omega}_{ij}$. Red circles represent the trajectories of motion.

Similarly, the motion of two plates i and j, rotating with respect to each other (Figure 1.6) may be represented as a rotation about one axis passing

through the center of the Earth, the linear relative velocity vector of any point reads

$$\vec{V} = \vec{\omega}_{ij} \times \vec{R}$$

Since vectors are additive, the (unknown) rotation vector for any plate may be found by combining the (known) rotation vectors from two other plates:

$$\vec{\omega}_{ij} = \vec{\omega}_{ik} + \vec{\omega}_{kj}$$

1.5 Relative plate motions

The relative plate motion models are estimated in reference frames attached to the lithosphere. This means that the rotation vectors may be expressed with respect to plate pairs, with respect to one plate, or ultimately, with respect to the mean lithosphere.

These conventional models originate directly from the relative nature of data, since they combine the relative rates across ridges with the directions of motion (azimuths of transform faults) and earthquake slip vectors at plate boundaries.

The least squares estimation of the relative rotation rates and poles is performed applying the closure condition of a global circle connecting all the plates; it has constituted the basis of the first global relative models, describing the instantaneous motion over the past few millions years, depending on the geomagnetic chronological scale.

The closure condition implies that, given a series of rotation vectors, if you start and end with the same plate, the net rotation should be zero:

$$\vec{\omega}_{ii} = \vec{\omega}_{ik} + \vec{\omega}_{kj} + \vec{\omega}_{ji} = 0$$

From this, it is obvious that $\vec{\omega}_{ji} = \vec{\omega}_{ij}$

The continuously increasing data set has allowed to refine the model accuracies, from the first by Morgan (1968), Le Pichon (1968), CH72 (Chase, 1972), RM1 (Minster et al., 1974), PO71 (Chase, 1978), RM2 (Minster and Jordan, 1978) to the recent NUVEL-1 (DeMets et al., 1990) and NUVEL-1A (Argus and Gordon, 1991; DeMets et al., 1994) (Figure 1.7); this fact is more evident after the advent of space geodesy and GPS. A large amount of GPS observations, velocities and azimuths is now freely available on many online databases; they are continuously updated by geodetic centres accredited by international scientific services, allowing detailed analyses from global to local scale.

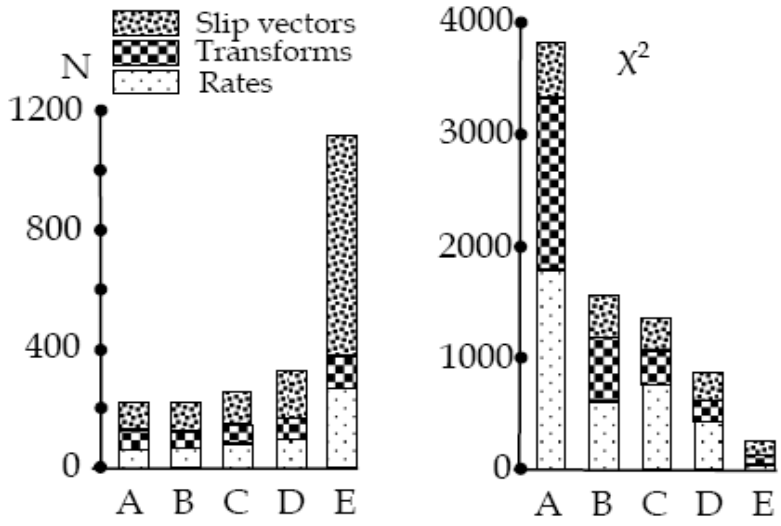

Figure 1.7: Increase of accuracy with the growing number of data (N), from earlier plate kinematic models to NUVEL-1: A=CH2 (Chase, 1972), B=RM1 (Minster et al., 1974), C=P071 (Chase, 1978), D=RM2 (Minster and Jordan, 1978), E=NUVEL-1 (modified from DeMets et al., 1990).

One of the most important geodynamic results of space geodesy has been the verification that, far from deformation areas, plate motions have remained generally steady over the past few million years. This is shown by the striking agreement between motions measured over a few years by space geodesy and the predictions of global plate motion models based on geological/geophysical observations that average the past three million years (Figure 1.8) The good match between past and present day plate motions shows that the relative velocities detected by space geodesy are a good indicator of the main Cenozoic and Neozoic plate relative motions (Stein, 1993).

Plate kinematic models referred to the mean lithosphere are called no-net-rotations (NNR), i.e. the lithosphere has not a residual rotation rate. This frame is defined as the reference frame that satisfies the condition in which the global angular momentum is zero, namely assuming a constant density.

$$\int_S \vec{V} \times \vec{R}\ dS = 0$$

where $\vec{V}$ is the plate velocity at position $\vec{R}$ and S is the lithosphere surface.

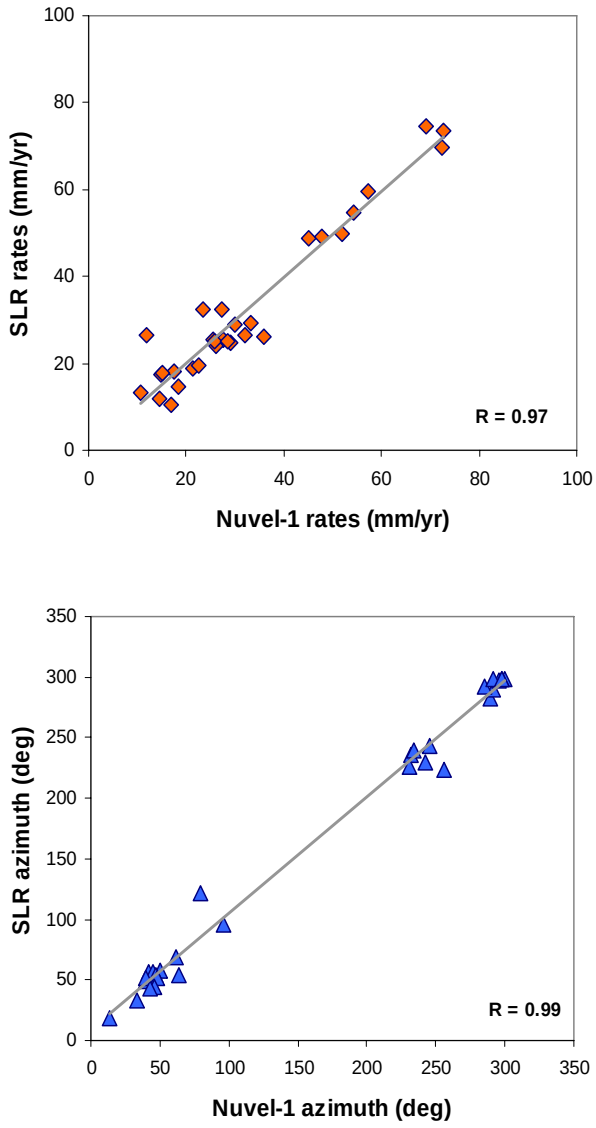

Figure 1.8: Space geodetic rates and azimuth of sites far from deformation zones are in very good agreement with those predicted by NNR-NUVEL-1 (data from Smith et al., 1994).

One example is the model NNR-NUVEL1 plate tectonic model by Argus and Gordon (1991) describing the angular velocities of the 14 major tectonic plates defined by a no net rotation constraint (Table 1.2, Argus and Gordon, 1991).

Table 1.2: NNR-NUVEL1 Euler poles and rotation rates

Plate	Lat. °N	Lon. °E	Ω °/Myr	rms velocity
AF	50.6	-74.0	0.30	30
AN	63.0	-115.9	0.25	16
AR	45.2	-4.4	0.57	46
AU	33.8	33.2	0.68	66
CA	25.0	-93.1	0.22	9
CO	24.5	-115.8	1.58	77
EU	50.6	-112.4	0.24	25
IN	45.5	0.4	0.57	59
JF	-27.4	58.1	0.64	20
NA	-2.5	-86.0	0.22	20
NZ	47.8	-100.2	0.78	79
PA	-63.0	107.4	0.67	67
PH	-39.0	-36.7	0.95	42
SA	-25.4	-124.6	0.12	12

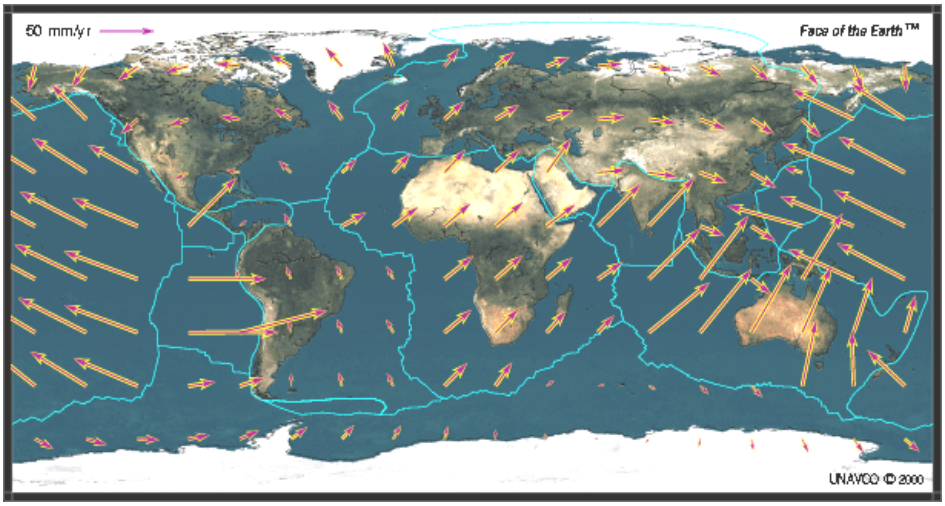

Figure 1.9: NNR-NUVEL-1A velocity field for major tectonic plates (DeMets et al., 1994) (from http://sps.unavco.org/crustal_motion/dxdt/model/).

Fixing any plate (the Pacific Plate is usually fixed) to zero velocity will yield velocities in the NUVEL-1 relative plate motion model which are derived from paleomagnetic data, transform fault azimuths and earthquake slip vectors (DeMets et al., 1990). Note that a recent revision of the paleomagnetic time scale has lead to a rescaling of the angular rates by a factor of 0.9562 (see DeMets et al., 1994), defining the newer models NUVEL-1A and NNR-NUVEL-1A (Figure 1.9). The model NNR-NUVEL-1 incorporates the NUVEL-1 model originally referred to the Pacific plate (Argus and Gordon, 1991). The angular velocity of the Pacific plate relative to the no-net-rotation reference frame is then calculated from

$$\omega_{PA} = (-3/8\pi) \cdot \sum_i Q_i \cdot \omega_i$$

where Q_i are the geometrical tensors of each plate accounting for the normalized plate surfaces (Solomon and Sleep, 1974).
A comparison between the NNR-NUVEL1 model and the model AM0-2 (Minster and Jordan, 1978) evidenced a residual net rotation of 1.5 cm/yr.
Differences between the NNR-NUVEL1 and HS2-NUVEL1 are described by a right-handed rotation of 0.33°/Myr about a pole located at 49°S and 65°E.
Recently, many other NNR plate kinematic models have been estimated from space geodetic observations: the recent ITRF2005, details in Chapter 2 (Altamimi et al., 2007); the APKIM2000, Figure 1.10 (Drewes and Meisel, 2003) and formerly the REVEL (Sella et al., 2002).

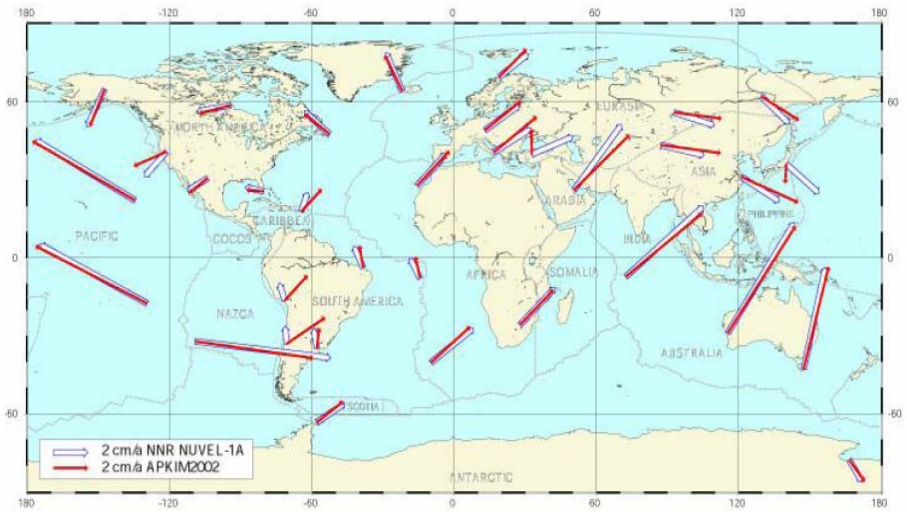

Figure 1.10: The APKIM2000 (Drewes and Meisel, 2003) and the NNR-NUVEL1A models (DeMets et al., 1994), (from Drewes and Meisel, 2003).

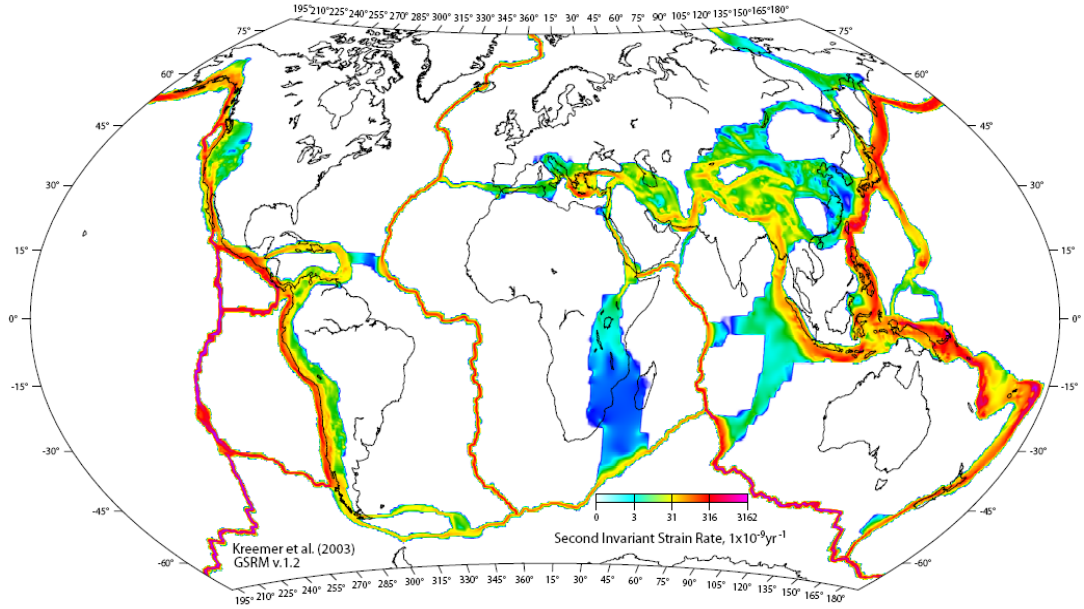

Figure 1.11: Contours of the second invariant of the model strain rate tensor field obtained by a least squares fit to the geodetic velocities and strain rates obtained from seismological and geological observations (from Kreemer et al., 2000).

The second invariant is defined as $\sqrt{\dot{\varepsilon}_{\phi\phi}^2 + \dot{\varepsilon}_{\theta\theta}^2 + 2 \cdot \dot{\varepsilon}_{\phi\theta}^2}$ where $\dot{\varepsilon}_{\phi\phi}, \dot{\varepsilon}_{\theta\theta}$ and $\dot{\varepsilon}_{\phi\theta}$ are the horizontal components of the strain rate tensor.

Different by nature is the first NNR model that implicitly add the kinematics of plate boundary deformation to a description of rigid plate motions (Kreemer et al., 2000; Kreemer and Holt, 2001; Kreemer et al., 2003). The model provides both the estimates of strain rate (Figure 1.11) and velocity field (Figure 1.12), by introducing geodetic observations and seismo-tectonic strain rates obtained through a summation of Quaternary fault and seismic moment tensors (Dziewonsky et al., 2000) slip rates, using a variant of Kostrov's formula (Kostrov, 1974).

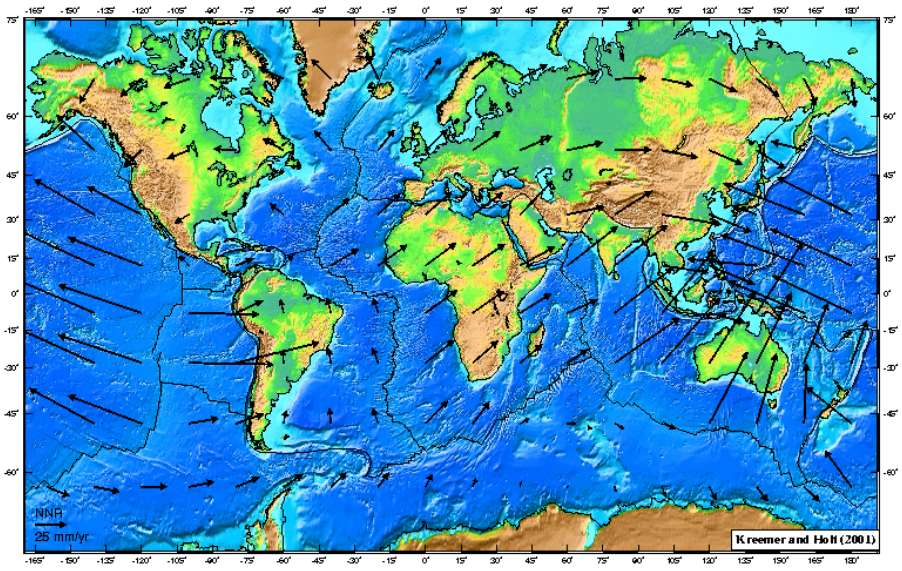

Figure 1.12: NNR plate kinematic model including rigid plate motions and velocity gradients within plate boundary zones (from Kreemer and Holt, 2001). The estimated velocity field is significantly different from earlier models in areas of diffuse deformation.

1.6 Absolute plate motions and the hotspots

One of the main consequences due to the application of the NNR condition is that it allows only accurate estimations of relative motions, whilst other motions, for instance with respect to the inner layers of the Earth body, are not determinable.

Since the observations useful to define plate kinematics are relative by nature, absolute plate motion models, describing the motion of plates relative to the mesosphere, rely on the assumption that it is possible to know at least the motion of one plate with respect to the mantle. This link is provided by the hotspots, a peculiar type of volcanoes observed for the first time by Wilson (1963) and interpreted by Morgan (1972) as directly connecting the mantle with the Earth's surface.

Absolute plate motion models are based on the assumption that the mantle is deforming slowly enough to constitute a reference independent from the plates themselves and the hotspot tracks are recording the relative

motion between lithosphere and mantle. The hotspot framework is based on the further assumption that the hotspots are stationary relative to each other (Morgan, 1971, 1972; Wilson, 1973), and that the age progressions and trends of the linear island chains reflect the motion between the plates and the mesosphere. When a plate passes on a hotspot, a seamount volcanic chain is formed. The classical example is the Hawaii-Emperor island seamount chain that displays a nearly linear age progression (Dalrymple et al., 1980). The rate and azimuth of the hotspot track contribute to define the rate and the azimuth of the plate motion, whereas the motion of the other plates can be estimated by applying the closure conditions.

The first attempts to model absolute motion were proposed by Lliboutry (1974) and Solomon and Sleep (1974); their models are based on a dynamic balance of forces acting on the lithosphere. After, were proposed other models, the first AM0-1 is no net rotation; then followed AM1-2, AM2-2 and AM3-3, based on the RM2 relative model (Minster and Jordan, 1978). AM2-2 is based on the Burke and Wilson hypothesis (1972) considering the African plate stationary with respect to the mantle, a criterion endorsed by Duncan and McDougall (1976) on the basis of Pacific hot spot data. AM3-2 reflects the Jordan's idea (1975) according to which the Caribbean plate is fixed. AM1-2 shows the best fit to the hotspot data set, on average the rate data all fit within 1 cm/yr, thus confirming the Wilson-Morgan hypothesis.

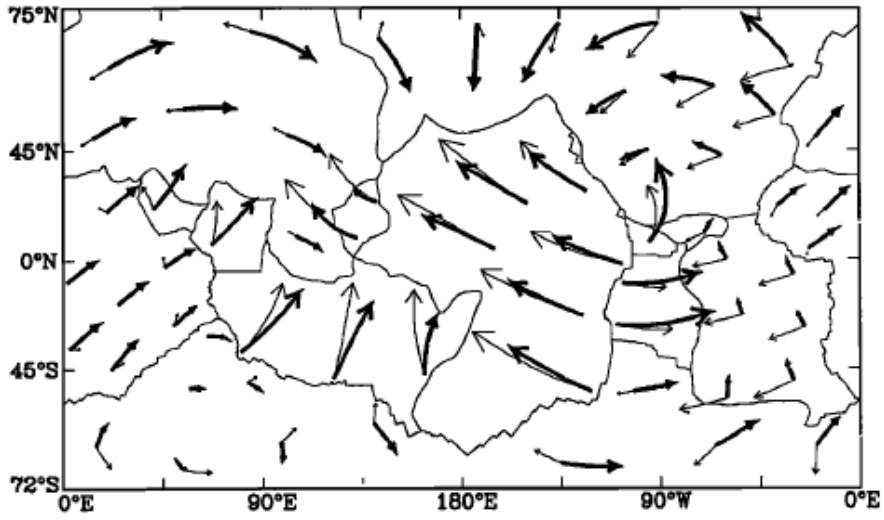

Figure 1.13: Comparison between the NNR-NUVEL1A model, thick arrows (Argus and Gordon, 1991) and the HS2-NUVEL1, thin arrows (Gripp and Gordon, 1990). Arrows show the trajectory of the lithosphere if the current angular velocities remained unchanged over 50 Myr (from Argus and Gordon, 1991).

Recent absolute plate kinematic models are the HS2–NUVEL1 (Gripp and Gordon, 1990) and the HS3–NUVEL1A (Gripp and Gordon, 2002), respectively based on the relative model NUVEL–1 (DeMets et al., 1990) and NUVEL-1A (Argus and Gordon, 1991; DeMets et al., 1994), having the advantage to incorporate space geodetic data. Figure 1.13 shows a comparison between the motion predicted by the HS2–NUVEL1 and the NNR-NUVEL1A models; the last model rotates with respect to the first by a right-handed rotation of 0.33°/Myr about a pole located at 49°S, 65°E. The differences between the two reference frames are completely specified by this rotation because NNR-NUVEL1A and HS2-NUVEL1 contain identical relative plate velocities.

1.7 One or more hotspots reference frames (HSRF)?

Most of the Earth's volcanism is associated with the plate boundaries, along the ridges and subduction zones; nevertheless, there is a limited number of volcanoes unusual under several aspects: they occur intraplate, have a different chemistry and often the active volcano may be at one end of an island chain, with the islands ageing with the distance of the active volcano. These features are consistent with a formation of the chain corresponding to a counter motion of the plate over the mantle.

Since the Wilson's idea (1963), the hotspot tracks have been used to compute the motion of plates relative to the mantle.

Morgan (1971, 1972) hypothesized that the hotspots are manifestations of convection in the lower mantle which provides the motive force for continental drift. In his model there are about twenty deep mantle plumes, probably originating from the core-mantle boundary, bringing heat and relatively primordial material up to the asthenosphere and horizontal currents in the asthenosphere flow radially away from each of these plumes. Morgan believed his model compatible with the observation that there is a difference between oceanic island and oceanic ridge basalts.

Therefore, a plume is a hypothetical mantle feature; a hotspot is a region of magmatism or elevation that has been deemed to be anomalous in some respect because of its volume or location. In the plume hypothesis, a hotspot is the surface manifestation of a plume, but the concepts are different; one is the presumed effect, and the other is the cause (Anderson, 2000).

The hotspots may have different origin and variable depth source (e.g., Courtillot et al., 2003). There are a number of growing evidences suggesting

that the so-called hotspots are rather superficial features, originating either from the asthenosphere, or the lithosphere base itself (Bonatti, 1990; Smith, 1993; Smith and Lewis, 1999; Anderson, 2000), possibly unrelated to deep mantle sources. For example some Atlantic hotspots have been interpreted as derived from an asthenosphere richer in fluids, being in fact cooler than other segments of the Mid Atlantic Ridge, but wetter (Bonatti, 1990). Some other Pacific intraplate hotspots have rather been interpreted as related to the shear heating generated at the decoupling interface between lithosphere and asthenosphere (Doglioni et al., 2005). Other shallow mechanisms that have been proposed are fissures or grabens in the lithosphere (Natland and Winterer, 2005; Anderson, 2005) but other segments of the scientific community still prefers to interpret hotspots as deep mantle features (e.g., Morgan, 1971; Davies, 1988) or intermediate sources (e.g., Ritsema and Allen, 2003). Therefore different magmatic trails or hotspots tracks at the surface could have different origins and depth sources, although they are still often erroneously mixed together or considered as a single system (Figure 1.14).

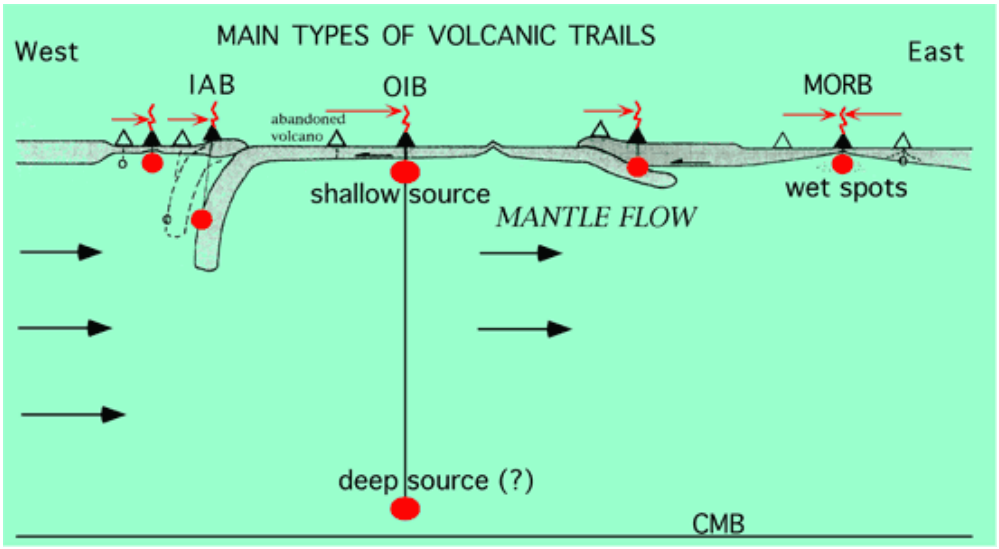

Figure 1.14: The main volcanic chains may have different origins and depths. The red arrows indicate the direction of volcanism migration with time. Filled triangles represent the youngest volcanic products. Volcanic trails originating on ridges may be wetspots (in sensu Bonatti, 1990) and derived from a fluid-rich asthenosphere. The hotspots located on plate boundaries are not fixed since both ridges and trenches move relative to one another and with respect to the mantle. Pacific hotspots, regardless their source depth, are located within the plate and are virtually the only ones that can be considered reliable for a hotspot reference frame. (from Cuffaro and Doglioni, 2007).

Since most of the hotspots are steadily located on ridges, rift zones or transform zones, (Figure 1.15) they cannot be considered as stable reference for plate motion modelling. In principle, the definition of any plate kinematic model with respect to the mantle should be based on an optimal choice of the hotspot candidates to realize a suitable reference frame. This is the motivation for which the selection of reliable hotspots is of fundamental importance; nevertheless, in spite of the geodynamic discussions still alive, the conservative choice of selecting exclusively the more reliable intraplate hotspots (Gripp and Gordon, 2002) seems the only reasonable.

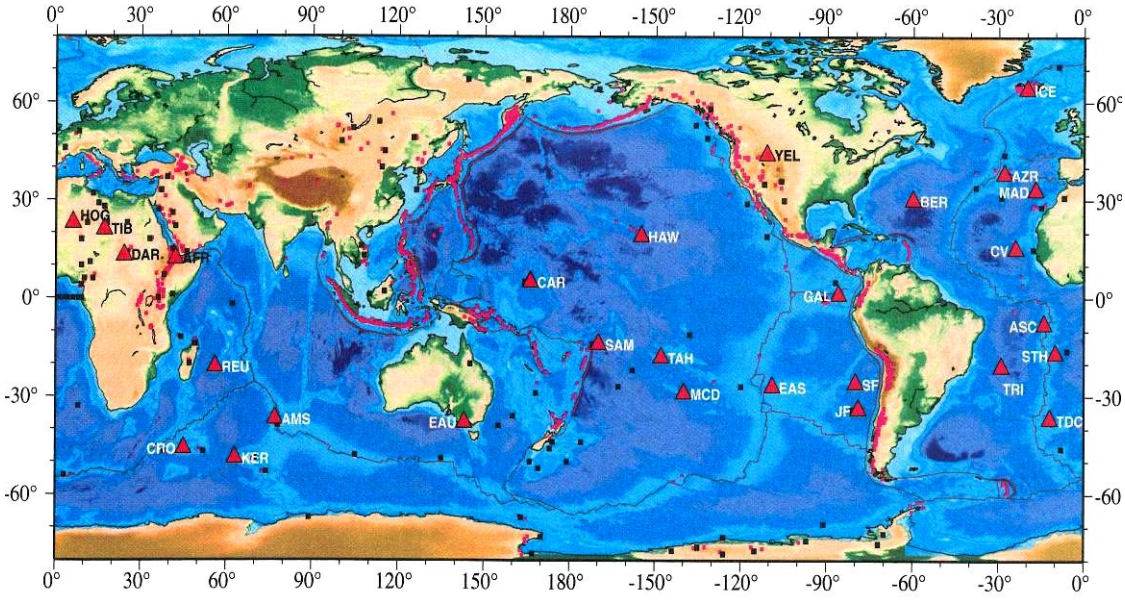

Figure 1.15: Map showing the classic hotspots (HS) (from Anderson and Schramm, 2005). The more significant HS are indicated by red triangles, active volcanoes by red squares and earlier rejected hotspots by black square.

The plate on which the selected hotspots are located become the reference plate defining the known tangential velocity with respect to the mantle; moreover, since any possible depth assigned to the hotspot source reflects directly on the velocity assumed by the reference plate, we will overcome this problem by calibrating our model for different velocities that can be assumed by the reference plate (Chapter 3.6).

1.8 Westward drift of lithosphere

Since the intuition of Wegener (1915), there have been a number of papers describing a westward drift of the lithosphere relative to the mantle.

The first attempts to evaluate a net rotation of the lithosphere were made by fixing one plate, assumed to be attached to the mantle: the classic evidence of the drift was estimating plate motions relative to Antarctica (Le Pichon, 1968; Knopoff and Leeds, 1972), Figure 1.16. Successive evaluations were computed by comparing the residual plate by plate rotation vector between the HS and NNR models (Gripp and Gordon, 1990; Argus and Gordon, 1991; Gordon, 1995; Gripp and Gordon, 2002).

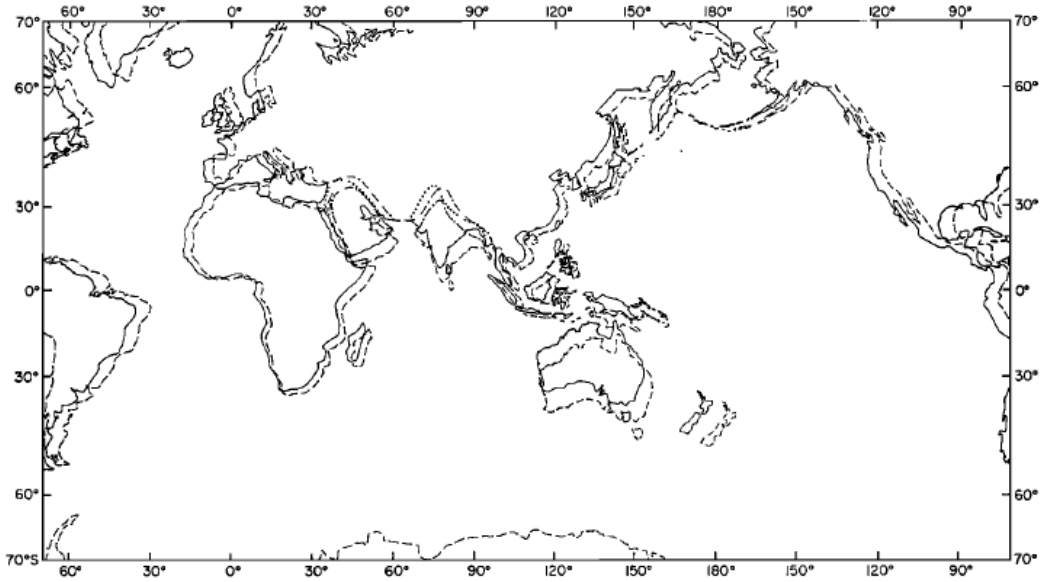

Figure 1.16: Plate motion relative to Antarctica; dashed line: position of continents about 10 Myr ago; full line: present day position (from Le Pichon, 1968).

Some models have explained the westward drift by the dynamics of an Earth's model where the asthenospheric viscosity below the oceans is at least one order of magnitude lower than underneath the continents (Ricard et al., 1991; O'Connell et al., 1991).

In other studies, tidal or Earth's rotation effects have been invoked to explain this polarization (Bostrom, 1971, 2000; Knopoff and Leeds, 1972;

Moore, 1973); however Jordan (1974) and Jeffreys (1975) contradicted the effects of the moon on the lithosphere and these models were abandoned.

Recent studies have shown that the existence of a global tectonic pattern (Doglioni, 1990, 1993) may be inferred by many global tectonic evidences: the directions of the subduction zones that follow an ordered undulated flow (Figure 1.17 A), and the angle asymmetry of their related slabs.

A

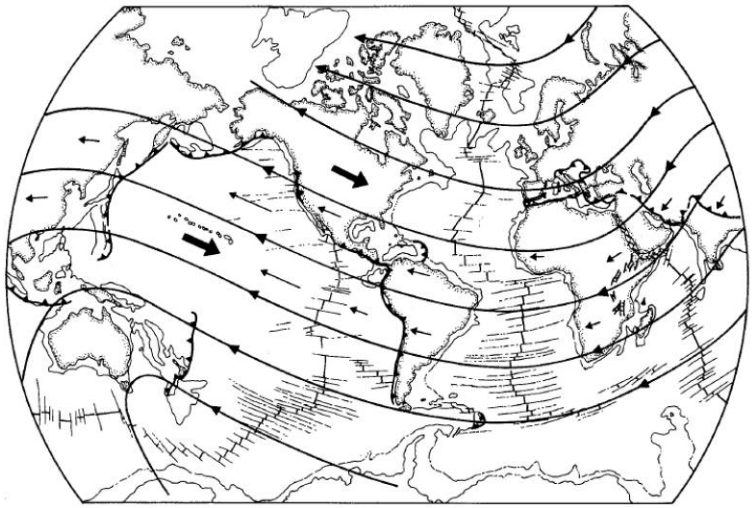

B

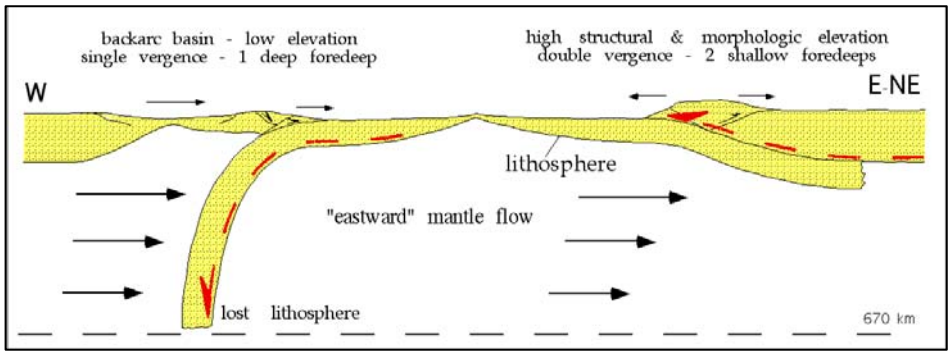

Figure 1.17: (A) Connecting the directions of relative motion it is inferred that lithosphere plates do not move randomly with respect to the mantle, but follow an ordered, undulated westward directed flow; (B) W-directed subductions are steeper than those E-NE-directed; the associated orogens are respectively characterized by lower structural and topographic elevation, backarc basin, and in the other side by higher structural and morphological elevation and no backarc basin. This asymmetry would be explained by the relative motion between the whole lithosphere (toward the west) and the underlying mantle (from Doglioni, 1990; Doglioni et al., 1999).

In fact, along this flow, west-directed subduction zones are steeper than those E– or NE–directed; the associated orogens are respectively characterized by lower structural, topographic elevation and backarc basin; whereas, in the other side by higher structural and morphological elevation and no backarc basin (Doglioni et al., 1999) (Figure 1.17 B).

The asymmetry is striking when comparing western and eastern Pacific subduction zones, and it is usually interpreted as related to the age of the downgoing oceanic lithosphere, being considered older, cooler and denser in the western side. However these differences persist elsewhere, regardless the age and composition of the downgoing lithosphere, e.g., in the Mediterranean Apennines and Carpathians Vs Alps and Dinarides, or in the Banda and Sandwich arcs, where even continental or zero-age oceanic lithosphere is almost vertical along west-directed subduction zones (Cruciani et al., 2005). Rift zones are also asymmetric, being the "eastern" side more elevated of about 100-300 m worldwide (Doglioni et al., 2003).

In spite of its proven and accepted existence, the westward drift of the lithosphere has been not fully understood so that its implications are far to be applied: as a relevant example, both plate kinematics and space geodesy reference frames are still attached to the no-net-rotation assumption (e. g. Argus and Gordon, 1991; Heflin et al., 2004).

In particular, there are still doubts about 1) which is the engine of the westward drift, (Ricard et al., 1991; Ranalli, 2000; Scoppola, 2006) and 2) whether it affects the entire lithosphere or it is rather only a mean value, with most of the lithosphere moving "west", but part of it still moving in the opposite direction relative to the mantle. According to this last idea, only some plates would move westward, and since one of them is the Pacific plate, which is the largest and the fastest moving WNW-ward (Figure 1.18), the sum of all vectors would maintain a residual westward component, without a complete polarization (Gripp and Gordon, 1990; Henderson, 2001; Gripp and Gordon, 2002).

Regardless its nature and speed, combined with the hotspots tracks, the westward drift indicates the existence of a decoupling surface between lithosphere and sub-asthenospheric mantle.

1.9 The Low Velocity Zone (LVZ)

One of the assumptions on which the westward drift of the lithosphere is based on is that there is no effective coupling between the lithosphere and the

mantle. This condition is possible hypothesizing the presence of a global-scale ultra-low viscosity layer, with variable thickness, from few tens of km, under most of the shields, to few hundreds, under the most tectonically active plates. Such a layer would permit the lithosphere/asthenosphere rotational decoupling to be effective and the mantle convection would add lateral variations of viscosity (Thybo, 2006) permitting relative motion between plates.

The question of the actual value of the asthenosphere viscosity is still matter of debate, in fact there are many papers indicating a value too high in order to allow a complete decoupling of the overlying lithosphere (Jordan, 1974; Jeffreys, 1975; Ranalli, 2000). However, there are several limitation in the proposed asthenosphere viscosity estimates: they are based on the post-glacial rebound modeling really related to the bulk viscosity (e.g., Lambeck, 1980), not to the shear viscosity associated to the decoupling zone, which may be lower up to three orders of magnitude (Scoppola et al., 2006; Aoudia et al., 2007; Melini et al., 2008).

There are a number of counter arguments casting doubts about the viscosity estimation from the post-glacial rebound models:

1) the viscosity is obtained as averaged value over the entire asthenosphere thickness (between 100 and 400 km depth, e.g., Lambeck, 1980; Paulson et al., 2007);
2) the asthenosphere might have different values of viscosity as a function of the time-scale of the process, as the mantle with a non-linear rheology (e.g., Giunchi and Spada, 2000);
3) the model of post-glacial rebound are pertaining to areas where the low velocity layer in the asthenosphere is less evident from seismic tomography (in particular in parts of the Baltic shield it seems absent, Calcagnile and Panza, 1978; Calcagnile, 1991).

On the contrary, there are several evidences supporting the existence of low viscosity zones: petrological models, hypothesizing a H_2O rich-upper mantle (e.g., Hirth and Kohlstedt, 1996); the presence of clinopiroxene in the asthenosphere that could significantly lower the viscosity in comparison to dry olivine; P and S waves tomography indicate the presence of a very-low seismic velocity few tens of km thick layer atop the asthenosphere (Rychert et al., 2005; Panza et al., 2007). Moreover, the presence of a thin ultra-low viscosity layer in the asthenosphere can be invisible to Glacial Isostatic Adjustment (GIA) due to the channel flow effect (Cathles, 1975; Scoppola et al., 2006).

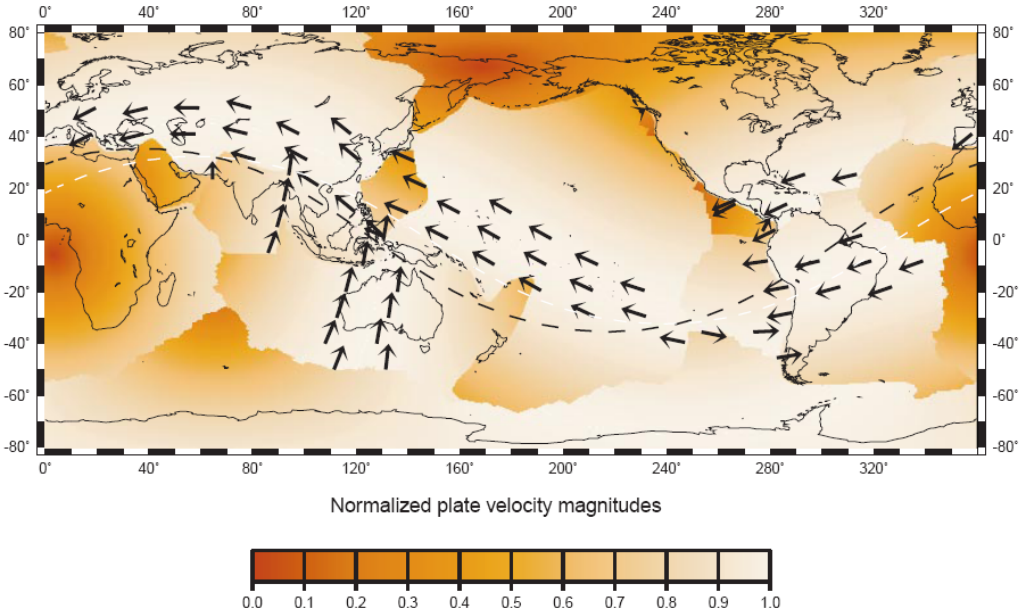

Figure 1.18: Delineation of a global fast `belt' of plate velocities from the HS2 plate motion model (Gripp and Gordon, 1990). The combination of bright relative plate velocity magnitudes and vector fields highlights the zone of fast plate motions that are closely aligned with great circles. The black dashed line is the great circle of best fit to all the fast locations. The white dashed line is another great circle of best fit determined excluding the outliers with respect to the black line (from Henderson, 2001).

2 Reference Systems and Reference Frames

2.1 Introduction

The establishment of global geodetic networks based on the analysis of various geodetic observations has the aim to supply a unified means for describing position by providing coordinates of points on the Earth's surface.

In the last years, space geodetic observations, such as Very Long baseline Interferometry (VLBI), Satellite Laser ranging (SLR), Doppler Orbitography and Radio-positioning Integrated by Satellites (DORIS), Global Positioning System (GPS) and similar radio navigation systems have become a key tool in geodynamic studies devoted to the observation of plate motions and detection of deformations (Lambeck, 1988; Hofmann-Wellenhof et al., 2001).

These observations require an appropriate definition of reference frame, which is in turn defined by the geocentric Cartesian coordinates and velocities of global tracking stations, determined by means of space geodetic techniques themselves.

Positioning is therefore intricately linked to a reference system: the reference system is realized by the reference frame which is in turn defined by station positions. Any factor that affects stations and satellite positions, affects the reference frame and vice versa.

Since the late 1980s, the GPS constellation of satellites has become to play a major role in regional and global studies of the Earth. In the face of extensive diffusion and diversification of GPS applications, the worldwide scientific community has made an effort to promote international standards for GPS data acquisition and analysis and to deploy and operate a common comprehensive global tracking system.

Nowadays, the wide global network of high-precision GPS receivers offers the possibility to produce a reference frame that is dense, of a reasonably homogeneous quality, of sub-centimetric accuracy on a global scale, readily accessible to GPS users, ideal for monitoring variations in Earth's shape and providing kinematic boundary conditions for regional or local geodetic studies.

2.2 Terrestrial and Celestial Reference Systems and Reference Frames

Space geodetic techniques are based on differential positioning between the stations and the satellites and then both types of coordinates must be expressed in the same reference frame. The station positions are conveniently represented in a Terrestrial (Earth-fixed) Reference Frame rotating in some well defined way with the Earth, whereas the determination of the satellite orbits requires a geocentric Celestial (quasi-inertial) Reference Frame. Then, there is the need to define precisely the transformation parameters between one system to the other (Mueller, 1985).

The definition of the Terrestrial Reference System is complicated by geophysical processes that make the Earth's crust deforming at global, regional and local scales, at a magnitude greater than the precision of present-day space geodetic measurements. The definition of the Celestial Reference System is complicated by the fact that stellar objects have proper motions or structure and are not truly point sources (Arias et al., 1995).

The Celestial Reference System is realized by a catalogue of the equatorial coordinates of more than 118000 stars at epoch 1991.25 along with their proper motions, their parallaxes and their magnitudes (Kovalevsky et al., 1997). This is the Hipparcos Catalogue, the primary product of the European Space Agency's astrometric mission, Hipparcos. Launched in August 1989, Hipparcos successfully observed the celestial sphere for 3.5 years before operations ceased in March 1993. Calculations from observations generated the Hipparcos Catalogue of 118,218 stars charted with the highest precision (ESA, 1997). These coordinates define, at an arbitrary fundamental epoch, a Celestial Reference Frame (CRF).

The Terrestrial Reference System is realized through a set of Cartesian station coordinates at an arbitrary fundamental epoch, determined from a variety of space geodetic observations including SLR, VLBI and GPS (Kovalevsky et al., 1989; Boucher, 2001). These station positions define on the Earth's surface a fundamental polyhedron. The positions are expressed in a particular geocentric Cartesian coordinate system defined according to international standards. Maintaining the Reference Frame means to relate the rotated, translated and deformed polyhedron to the fundamental polyhedron at a later epoch. The deformations of the polyhedron are, by definition, those motions that do not contain any rotations or translations. The deformations are accommodated, at least at the first order, by supplementing the station catalogue with station velocities derived from long term geodetic

measurements. The Reference Frame does not change, unless a new one is defined, it is fixed to the station position at a reference epoch t_0 (station position in the fundamental polyhedron) and consists of a set of Cartesian coordinates and velocities at a given epoch. The connection between the TRF (fundamental polyhedron) and the CRF is given by nutation, precession and Earth orientation parameters (EOP).

2.3 Variability of the Earth's rotation vector

The Earth's orientation is defined as the rotation between a rotating geocentric set of axes attached to the Earth (the Terrestrial Reference System) and a non-rotating geocentric set of axes linked to inertial space (the Celestial Reference System).

The common way for describing the Earth's rotation is to specify the rotation matrix between these two systems. If the Earth was rotating uniformly around a fixed rotation axis (with respect to the Earth's crust and the celestial system), the Earth rotation changes would be described through one parameter only: the rotation angle varying linearly with time, or the time scale which can be derived from this rotation angle (the Universal Time). Actually the rotation axis is neither fixed with respect to the crust nor with respect to a celestial system, and the Earth's rotation rate undergoes slight variations (Mueller, 1971; Hide and Dickey, 1991).

The changes of the Earth's rotation vector are caused by the gravitational torque exerted by the Moon, Sun and planets, displacements of masses in different parts of the planet and other excitation mechanisms (Melchior, 1983; Yoder et al., 1981; Paquet et al., 1997). The observed oscillations can be interpreted in terms of mantle elasticity, Earth's flattening, structure and properties of the core-mantle boundary, rheology of the core, underground water, oceanic and atmospheric variability on time scales of weather or climate (Lambeck, 1980; Blewitt et al., 2001). The understanding of the coupling between the various layers of our planet is also a key aspect of the research on the Earth's rotation.

In principle the Earth's orientation can be described through three independent angles (for instance the Euler angles). However the classical monitoring of the Earth's rotation considers separately the motion of the rotation axis in the Earth and in the space inertial system. The main motion of the rotation axis in an inertial space is the precession. In addition, there are

small motions of the rotation axis called nutation (Figure 2.1) (Mathews et al., 2002).

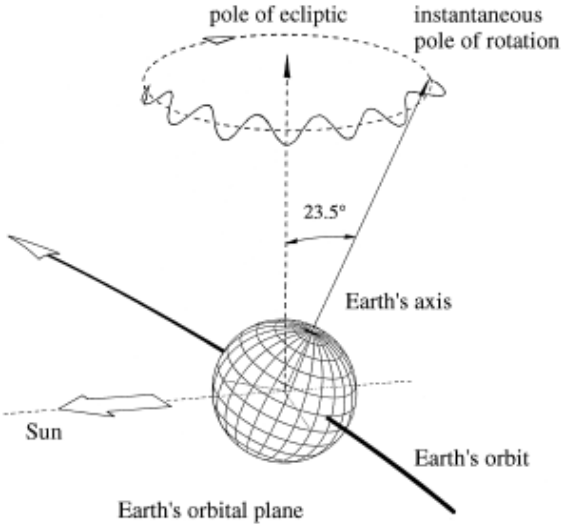

Figure 2.1: The Earth's rotation axis in inertial space

The motion of the Earth's rotation axis with respect to its crust (in the terrestrial frame) is called polar motion. Nutation and polar motion are due to both external torques (forced motion) and free motion. Nutation represents primarily the forced response of the Earth; polar motion represents the forced and free response in almost equal parts. Currently, only the forced response on the nutation can be well predicted from available geophysical and orbital models, supplemented by space geodetic measurements (VLBI). The free response of nutation and polar motion can only be determined by space geodesy (by VLBI and increasingly by GPS). Polar motion is the rotation of the true celestial pole as defined by the precession and nutation models with respect to the pole (Z-axis) of a conventionally selected Terrestrial Reference Frame (McCarthy and Petit, 2004). The polar motion observed accuracy is today 0.2-0.5 milliseconds of arc (mas), which is equivalent to 6-15 mm on the Earth's surface (Figure 2.2).

If all torques on the Earth were eliminated, its rotation axis would still vary with respect to its figure primarily due to its elastic properties and to

exchange of angular momentum between the solid Earth, the oceans and the atmosphere (Chao, 1989; Herring, 1992; Ray et al., 1994; Gross, 2000).

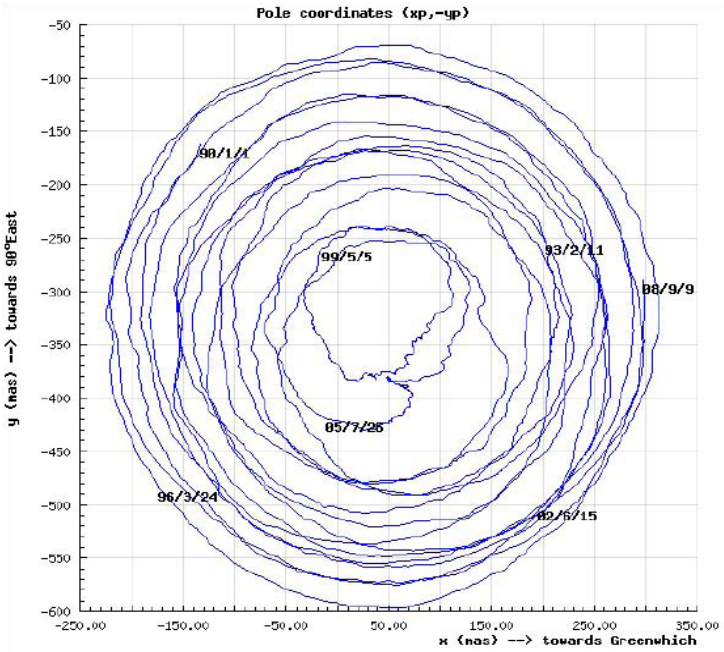

Figure 2.2: Polhody from 1/1/1990 to 11/9/2008, the trace of the polar motion on the polar tangent plane with respect to the conventional pole (created by the web site of IERS, Observatoire de Paris).

These geophysical excitations remain unpredictable, so that the polar motion is not completely modelled and determined empirically by space geodetic measurements of various sets of geophysical data. Consequently are routinely studied the time series of :

- Atmospheric Angular Momentum (AAM) excitation functions (routinely derived) and atmospheric torque on the solid Earth
- Oceanic Angular Momentum (OAM)
- Hydrological Angular Momentum (HAM) excitation functions
- Core angular momentum (CAM) associated with core-mantle electromagnetic coupling.

The polar motion free component (all external torques eliminated) has a somewhat counter clockwise circular motion with a main period of about 430 days (the Chandler period) and amplitude of 3-6 m. Its forced component

(due to tidal forces) is about an order of magnitude smaller, with nearly diurnal periods (Zschau, 1983), whereas its forced annual component due to atmosphere excitation is nearly as large as the Chandler motion.

The measurements of the Earth's rotation are under the form of time series of the so-called Earth Orientation Parameters (EOP) (Gambis and Bizouard, 2008). Universal time (UT1), polar motion and the celestial motion of the pole (precession/nutation) are determined by VLBI (Ma and Shaffer, 1991). The satellite-geodesy techniques, GPS, SLR and DORIS, determine polar motion and the rapid variations of universal time (Herring et al., 1991).

2.4 The International Earth Rotation and Reference Systems Service (IERS)

The IERS was established as the International Earth Rotation Service in 1987 by the International Astronomical Union and the International Union of Geodesy and Geophysics and it began operation on 1 January 1988. In 2003 it was renamed to International Earth Rotation and Reference Systems Service.

Its Central Bureau combines the result of different analysis centres adopting the same standards, disseminates information on the Earth's orientation, and maintains the Reference Frames.

The primary objectives of the IERS are to serve the astronomical, geodetic and geophysical communities by providing:

- The International Celestial Reference System (ICRS) and its realization, the International Celestial Reference Frame (ICRF).
- The International Terrestrial Reference System (ITRS) and its realization, the International Terrestrial Reference Frame (ITRF).
- The Earth orientation parameters, required to study the orientation variations and to perform transformation between the ICRF and the ITRF (Gambis and Bizouard, 2008).
- The geophysical data to interpret time/space variations in the ICRF, ITRF or EOP, and model such variations.
- The standards, constants and models (i.e., conventions) encouraging international adherence (McCarthy and Petit, 2004).

The IERS provides data on Earth orientation, on the International Celestial Reference System/Frame, on the International Terrestrial Reference System/Frame, and on geophysical fluids. It maintains also Conventions containing models, constants and standards.

The IERS bases its operability on the work of the following Services:

⇒ IVS, International VLBI Service for Geodesy & Astrometry (Schlüter and Behrend, 2007);
⇒ ILRS, International Laser Ranging Service (Pearlman et al., 2002);
⇒ IDS, International DORIS Service (Tavernier et al., 2006);
⇒ IGS, International GNSS (Global Navigation Satellite Systems) Service (Dow et al., 20005)

2.5 ICRS and ICRF: definition and realization

By Reference System it is meant the set of prescriptions and conventions together with the modelling required to define at any time a triad of axes. The International Celestial Reference System (ICRS) has the origin located at the barycentre of the solar system through appropriate modelling of VLBI observations. The Z axis is defined orthogonal to the reference celestial equator, the X axis is passing through the reference equinox γ and the Y axis is orthogonal to the XZ plane, to complete the right-handed tern (Figure 2.3, more details in the IERS web site).

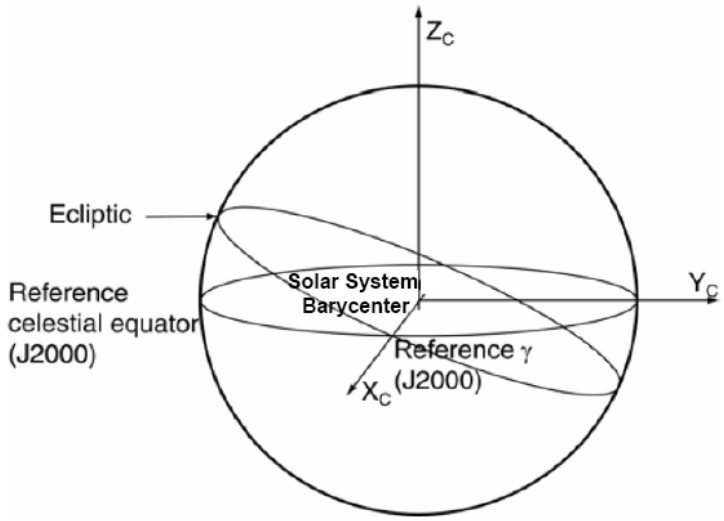

Figure 2.3: The Celestial Reference System.

The International Celestial Reference Frame (ICRF), the practical realization of the ICRS, is a quasi-inertial system defined to represent the Earth's motion with respect to some selected extragalactic radio sources observed by VLBI.

The ICRS can be connected to the ITRS by the EOP describing the irregularities of the Earth's rotation. Technically, they are the parameters which provide the rotation of the ITRS to the ICRS as a function of time (polar motion, LOD and celestial pole offsets). The ICRS is used to compute and describe the orbits of the Earth satellites. ICRS is not co-rotating with the Earth and is not useful to describe the positions of points located on the Earth's surface.

2.6 ITRS and ITRF: definition and realization

The International Terrestrial Reference System (ITRS) constitutes a set of prescriptions and conventions together with the modeling required to define origin, scale, orientation and time evolution of the system (Figure 2.4).

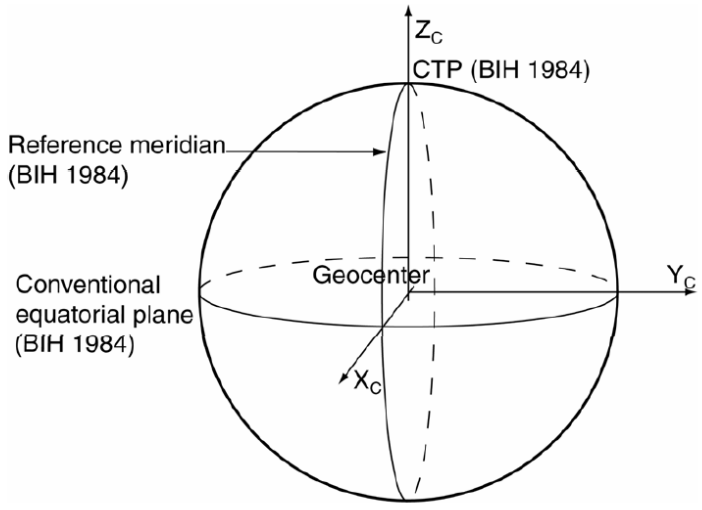

Figure 2.4: The Terrestrial Reference System.

Its definition fulfills the following conditions:

1. It is geocentric, the center of mass being defined for the whole Earth, including oceans and atmosphere.
2. The unit of length is the meter (SI). The scale is obtained by appropriate relativistic modeling defining the speed of light.
3. Its orientation was initially given by the BIH orientation at 1984.0.
4. The time evolution of the orientation is ensured by using a no-net-rotation condition with regards to horizontal tectonic motions over the whole Earth.

The ITRS is realized by the ITRF (Boucher and Altamimi, 1996), which is defined by the adopted geocentric Cartesian *c*oordinates and velocities of a set of reference stations observed by VLBI, LLR (Lunar Laser Ranging), GPS, SLR, and DORIS. The ITRF coordinates implicitly define the axes of the frame (orientation and origin). The model assumes that the instantaneous position of any point on the Earth's surface at epoch *t* may be linearly modeled by

$$X(t) = X_0 + \dot{X}(t - t_0) + \sum_i \Delta X_i(t)$$

The last term means that the coordinates of the reference stations are biased by tides (Cartwright and Tayler, 1971) and ocean loading (Schernek, 1993), these effects are modeled and removed whereas other source of deformations are not modeled.

The construction of ITRF is based on a combination of solutions provided by different centers of analysis. The model used for the combination is based on a similarity transformation of seven parameters:

$$\begin{bmatrix} X^S \\ Y^S \\ Z^S \end{bmatrix} = \begin{bmatrix} X \\ Y \\ Z \end{bmatrix}_{t_0} + \begin{bmatrix} T_X^S \\ T_Y^S \\ T_Z^S \end{bmatrix} + \begin{bmatrix} D^S & -R_Z^S & R_Y^S \\ R_Z^S & D^S & -R_X^S \\ -R_Y^S & R_X^S & D^S \end{bmatrix} \cdot \begin{bmatrix} X \\ Y \\ Z \end{bmatrix}_{t_0}$$

where T_X^S, T_Y^S, T_Z^S, D^S, R_X^S, R_Y^S, R_Z^S are respectively the three translations, the scale factor and the three rotations between the ITRF and individual *S* solutions.

Thanks to the good coherence found between velocities from space geodesy and the model NUVEL-1 (Figure 1.8, Chapter 1), the ITRF orientation rate has been defined by convention so that there is no-net-rotation (NNR) of the frame with respect to the Earth's lithosphere; this is

realized by aligning the ITRF to the geological tectonic model NNR-NUVEL-1A (Chapter1; Argus and Gordon, 1991).

It has to be underlined that the alignment of the ITRF to the NNR-NUVEL-1A model is not a rigorous way to define an Earth reference frame. In fact, a reference frame should refer to the behavior of the deforming Earth as a whole, involving all its mass points and not just a set of discrete points confined on its surface (Figure 2.5). The theoretical condition for a rigorous frame definition, the *Tisserand* frame, requires that

$$h = \int_E \vec{X} \times \frac{d\vec{X}}{dt} \cdot dm = 0$$

or, in discrete form

$$h = \sum_{i=1}^{P} m_i \cdot \begin{bmatrix} 0 & -Z & Y \\ Z & 0 & -X \\ -Y & X & 0 \end{bmatrix} \cdot \begin{bmatrix} V_X \\ V_Y \\ V_Z \end{bmatrix} = 0$$

the relative angular momentum of the whole Earth must be zero; however its practical realization is not easy, involving a detailed knowledge of each plate mass (Dermanis, 2001).

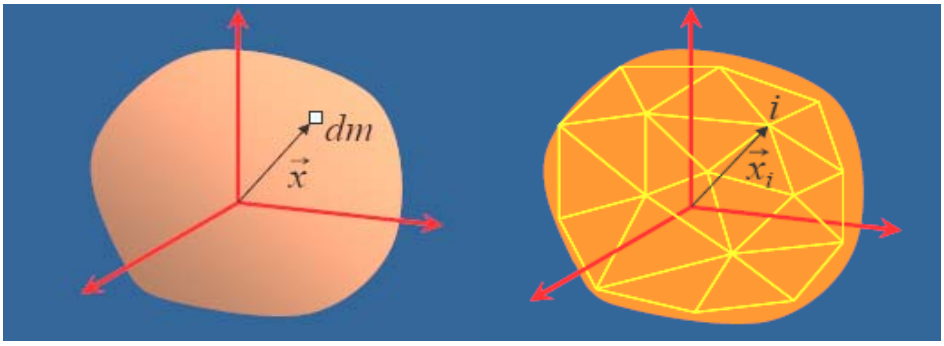

Figure 2.5: The Earth as a continuum (A) and as a network of discrete points (B) to which the *Tisserand* principle should be applied (from Dermanis, 2006).

The ITRF is an alternative realization of WGS84 created by the civil GPS community, quite independently of the US military organizations. The terrestrial reference system used by the U.S. Department of Defense (DoD)

for GPS positioning is the World Geodetic System 1984 (WGS84). It consists of three-dimensional Cartesian coordinate system and an associated ellipsoid, so that WGS84 positions can be described both as geocentric Cartesian or ellipsoidal coordinates. It was realized by the adopted coordinates of a globally distributed set of tracking stations with an estimated accuracy of 1-2 meters (compare to the 10-20 mm accuracy of ITRF). Because the ITRF is of higher quality than the military WGS84 TRF, the WGS84 datum now effectively takes its definition from ITRS. Therefore, although in principle the broadcast TRF is the principal realization of WGS84, in practice ITRF has become the more important Terrestrial Reference Frame because it has proven to be the most accurate global TRF ever constructed.

2.7 The ITRF2005

Each version of the ITRF is identified by a year code, indicating the year of realization. The last realization of ITRF is the ITRF2005 referred to the epoch 2000.0 (1 Jan 2000) (Altamimi et al., 2007). The solution is obtained by combining station positions and velocities estimated by many different analysis centers using observations of the main space geodesy techniques: VLBI, SLR, GPS and DORIS. The key-element of the ITRF combinations is the availability of co-location sites where two or more space geodesy instruments are operating and where differential coordinates, the so-called local ties, between the measuring reference points of these instruments are determined.

The ITRF2005 combination has been performed on one time series (rates and EOPs parameters) of solutions per each space geodesy technique. The time span covered by each series is different: 26 years for VLBI, 13 for SLR, 12 for DORIS and about 10 years for GPS.

The ITRF2005 is composed of 608 stations located at 338 sites (Figure 2.6), with an unbalanced distribution between the northern hemisphere (268 sites) and the southern hemisphere (70 sites). It is simply a list of coordinates (X Y and Z in metres) and velocities (dX, dY and dZ in metres per year) of each station in the TRF, together with the estimated level of error in those values. The coordinates relate to the time 2000.0; to obtain the coordinates of a station at any other time, the station velocity is applied to propagate coordinates along time, under the hypothesis of linear motion. Each ITRF realization is available as a SINEX (Software Independent Exchange) format text file from the IERS Internet web site.

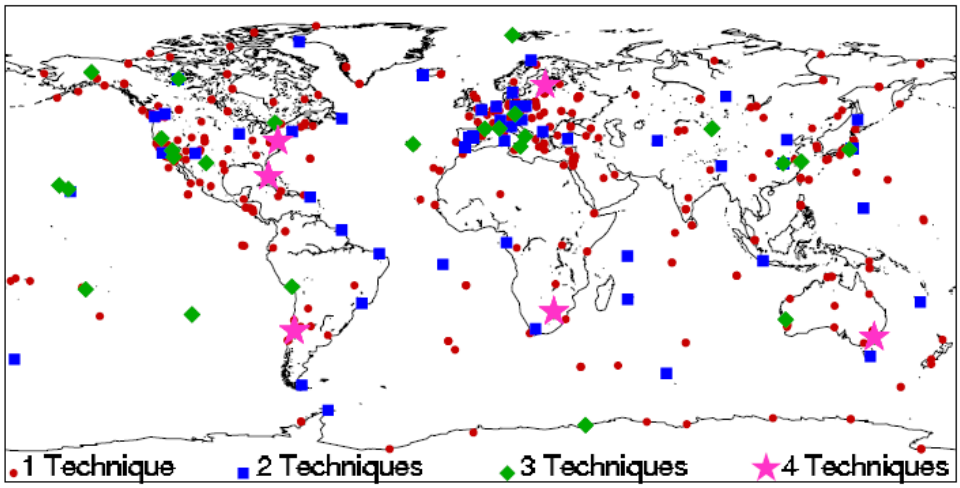

Figure 2.6: The ITRF2005 sites with the number of co-located techniques (from Altamimi et al., 2007).

A selected set of 152 velocities (Figure 2.7) has been used to estimate the ITRF2005 plate motion model defined by the rotation pole and rates of 15 plates (Table 2.1), each one with at least three velocity vectors.

Table 2.1: ITRF2005 Euler poles and rotation rates

Plate	Lat. °N	Lon. °E	ω °/Myr	rms °/Myr
AF	49.995	-82.501	0.269	0.003
AN	58.813	-125.315	0.223	0.007
AR	49.642	5.061	0.579	0.019
AU	32.407	37.367	0.628	0.003
CA	39.318	-104.279	0.241	0.145
EU	56.330	-95.979	0.261	0.003
IN	49.823	21.841	0.614	0.108
NA	-4.291	-87.385	0.192	0.002
NZ	45.101	-101.441	0.642	0.015
PA	-62.569	112.873	0.682	0.004
SA	-16.800	-129.631	0.121	0.003
SO	53.661	-89.542	0.309	0.019
YA	59.425	-109.737	0.310	0.021

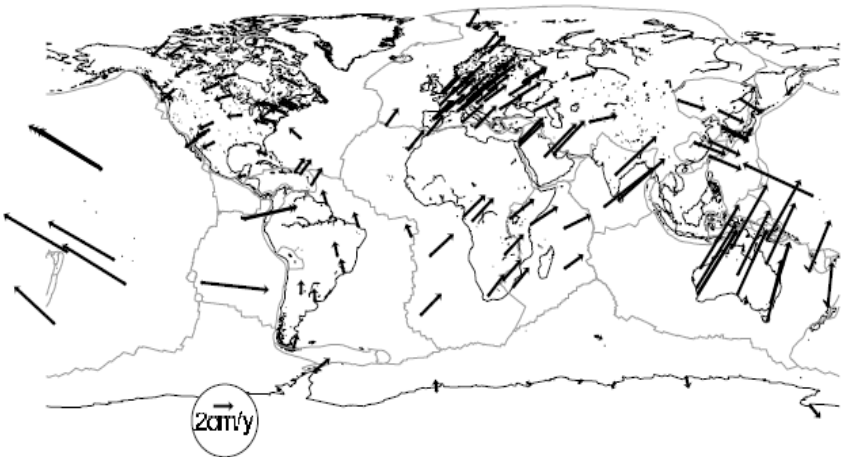

Figure 2.7: The ITRF2005 velocities used to estimate the plate rotation poles and rates (from Altamimi et al., 2007).

The selection of the sites satisfies the following criteria: (1) continuously observed during at least 3 years; (2) located on rigid parts of tectonic plates and far away from deforming zones; (3) velocity formal error, as result of the ITRF2005 combination, less than 1.5 mm/y; and (4) post-fit velocity residual (over East or/and North component) less than 1.5 mm/yr, after the rotation poles estimation. The errors in the rotation pole coordinates range between 0.3° to 35°, longitudes are the worst determined.

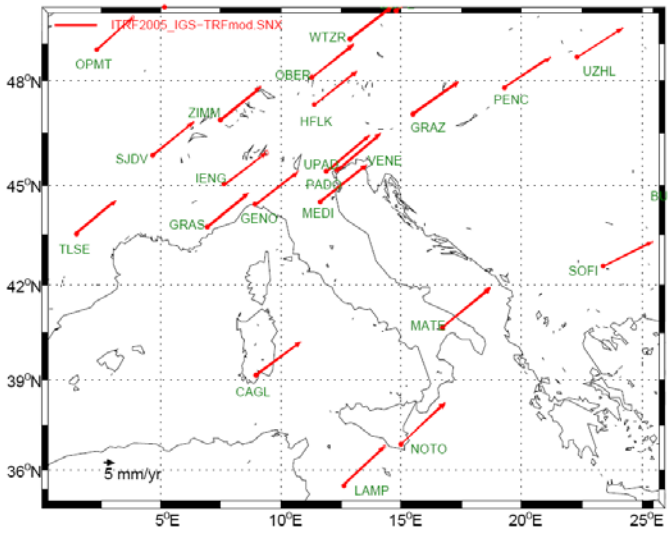

Figure 2.8: The ITRF2005 velocities in the Italian area, only 9 sites from Italy are selected to contribute to ITRF definition

In Italy only 9 sites are selected to contribute to the ITRF2005 definition (Figure 2.7). Some of these sites have co-located techniques or redundant GPS stations, for a total 13 observing sites (Table 2.2).

Table 2.2: ITRF2005 velocity components of the Italian sites

SITE	Lon	Lat	E	±E	N	±N	Up	±Up	azi
	°N	°E	mm/yr	mm/yr	mm/yr	mm/yr	mm/yr	mm/yr	°
CAGL	8.97	39.14	21.54	0.24	16.16	0.23	0.25	0.60	120.5
CAGZ	8.97	39.14	21.54	0.24	16.16	0.24	0.25	2.59	120.7
GENO	8.92	44.42	20.84	0.51	15.87	0.60	0.39	2.08	172.2
IENG	7.64	45.02	20.36	1.16	15.31	1.16	1.14	0.27	53.3
LAMP	12.61	35.50	19.56	1.11	18.68	0.77	0.21	1.57	95.7
MAT1	16.71	40.65	23.13	0.15	19.44	0.15	0.25	0.60	125.0
MATE	16.71	40.65	23.13	0.15	19.45	0.15	1.15	0.27	125.0
MEDI	11.65	44.52	22.29	0.18	17.61	0.18	-2.25	0.34	136.7
NOT1	14.99	36.88	21.17	0.19	19.83	0.19	-0.64	0.42	129.8
NOTO	14.99	36.88	21.17	0.19	19.83	0.19	-0.64	0.42	129.8
PADO	11.90	45.41	20.85	0.26	17.28	0.32	-1.18	0.92	174.6
UPAD	11.88	45.41	20.85	0.26	17.29	0.32	-1.18	0.92	174.6
VENE	12.33	45.44	20.97	0.45	17.47	0.53	2.04	3.89	176.4

2.8 The International GNSS Service (IGS)

The International Global Navigation Satellite Systems (GNSS) Service (IGS), formerly the International GPS Service (Mueller and Beutler, 1992), is a voluntary federation of more than 200 worldwide agencies that pool resources and permanent GPS and GLONASS station data to generate precise GPS and GLONASS products. The IGS is committed to providing the highest quality data and products as the standard for GNSS in support of Earth science research, multidisciplinary applications, and education. The IGS is essential for anybody requiring high accuracy WGS84 positions. The IGS operates a global TRF about 400 GPS stations (June 2008, Figure 2.8) and from these produces the following products freely distributed via the Internet:

- IGS tracking station dual-frequency GPS data.
- Precise GPS satellite orbits (ephemeredes).
- GPS satellite clock parameters.
- Earth orientation parameters.

- IGS tracking station coordinates and velocities; many of these stations are also listed in the ITRF.
- Zenith path delay estimates.

A set of GPS stations is selected for the IGS realization of ITRF (currently the IGS05). The main selection criteria are station performance, track record, monumentation, collocation and geographical distribution.
The difference between IGS05 and ITRF2005 is that the first is a GPS-based terrestrial frame, while the second is obtained after a combination of multi-technique solutions.

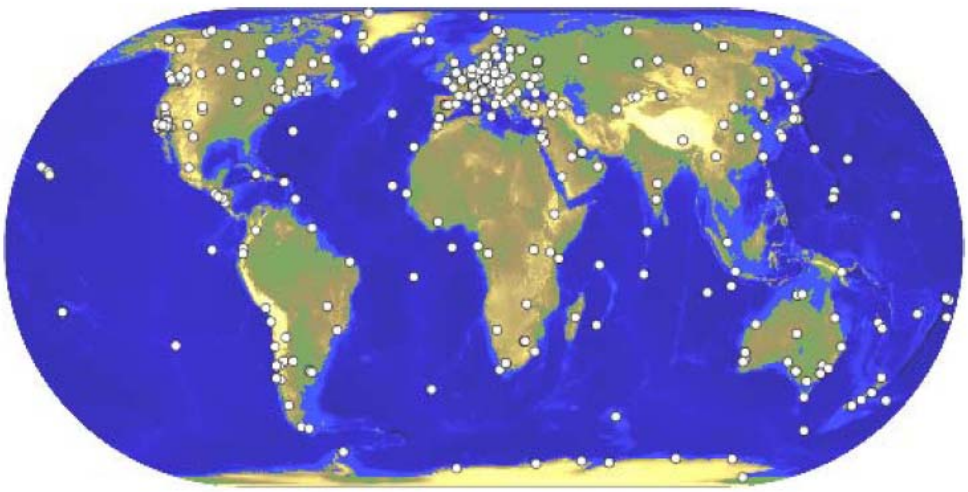

Figure 2.9: The IGS tracking network

3 A new plate kinematic model

3.1 Introduction

A difficult task in geodynamics is the definition of a reference frame useful for the representation of plate motions, due to a number of kinematic uncertainties.

Updated information on present plate motions is based on space geodesy data (Heflin et al., 2007.9; http://sideshow.jpl.nasa.gov/mbh/series.html), where the rate of motions are essentially estimated from GPS continuous observations (Figure 3.1) in a no-net-rotation frame (NNR), as assumed by the ITRF (Altamimi et al., 2002 a; 2002b).

Since the NNR hypothesis is an arbitrary choice introduced in order to fix the rank deficiency proper of the positions estimation problem based on space geodesy observations, this information is able to describe only for relative plate motions (Dermanis, 2001; 2002), whereas any absolute motion relative to the mantle is not accounted for.

We have seen that space geodesy data largely confirm the NNR-Nuvel1 model (Figure 1.8, Chapter 1), the Nuvel1 in a no-net-rotation frame, based on past ocean floor magnetic anomalies and focal mechanisms (DeMets et al., 1990; Argus and Gordon, 1991), with a good match between past and present day plate motions (Stein, 1993); therefore, it is assumed that present analysis is a good indicator of the main Cenozoic and Neozoic plate movements.

On the other hand, it is worth noting that the global analysis of tectonic features such as transform faults, subduction zones and rifts can also contribute to the present and past plate motions description. Using the major tectonic features on Earth, the plates appear not moving randomly, but they rather follow an undulated sinusoidal flow (Doglioni, 1990; 1993), with possible (second-order) sub-rotations (Cuffaro et al., 2004; 2008). Moreover, plate motions are westerly polarized, the so-called net rotation or "westward drift" (Le Pichon, 1968; Bostrom, 1971; Ricard et al., 1991; O'Connell et al., 1991) which can be evidenced both with respect to the Antarctica plate (Le Pichon, 1968; Knopoff and Leeds, 1972) as well as to the hotspot reference

frame (HSRF) (Gordon, 1995; Henderson, 2001; Gripp and Gordon, 2002). As underlined in Chapter 1, the existence of a westward drift polarizing the sinusoidal flow is also supported by independent geological and geophysical evidences, such as the asymmetry of subduction and rift zones following or opposing the relative counter motion of the mantle (Doglioni et al., 1999; Doglioni et al., 2003).

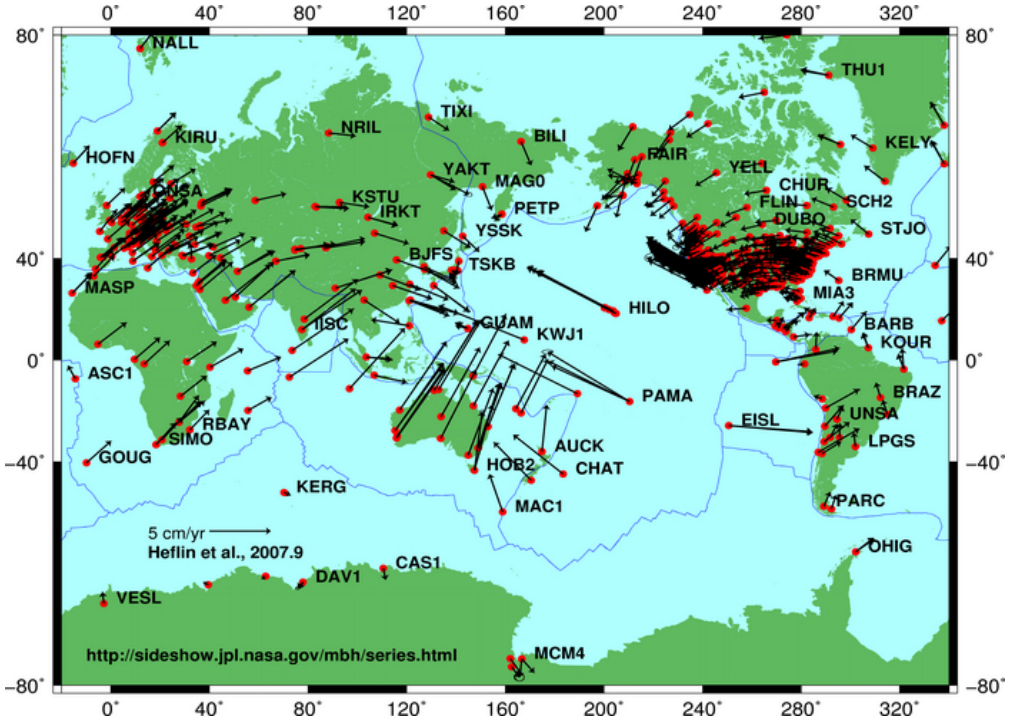

Figure 3.1: The recent solution of horizontal plate motion from the California Institute of Technology, JPL (Heflin et al., 2007.9) in the ITRF2005 (from http://sideshow.jpl.nasa.gov/).

The main purpose of this chapter is to propose a unified way to describe plate motions, overcoming the problems introduced by the NNR condition, taking into account that past and present plate kinematic analysis supports the existence of an ordered flow of plate motions which is polarized to the "west" in the HSRF. We propose an analytical description of the plate motions w.r.t. the underlying mantle, both accounting for relative plate kinematics inferred from space geodesy and first order tectonic constraints.

3.2 The *Tectonic mainstream*

In order to establish the geological constraints for the definition of the analytical model, let us consider the six major plate boundaries of Earth (Figure 3.2), Pacific-Nazca, Nazca-South America, South-America-Africa, Africa-Arabia/India, Arabia/India-Eurasia, and Eurasia-Pacific. In Figure 3.2, they are the East Pacific Rise (1), the Mid Atlantic ridge (2), and the Red Sea - Indian ridge (3), for extensional margins, and the western Pacific subduction zones (4), the western northern and southern Americas Cordilleras (5), and the Alpine-Himalayas system (6) for convergent margins.

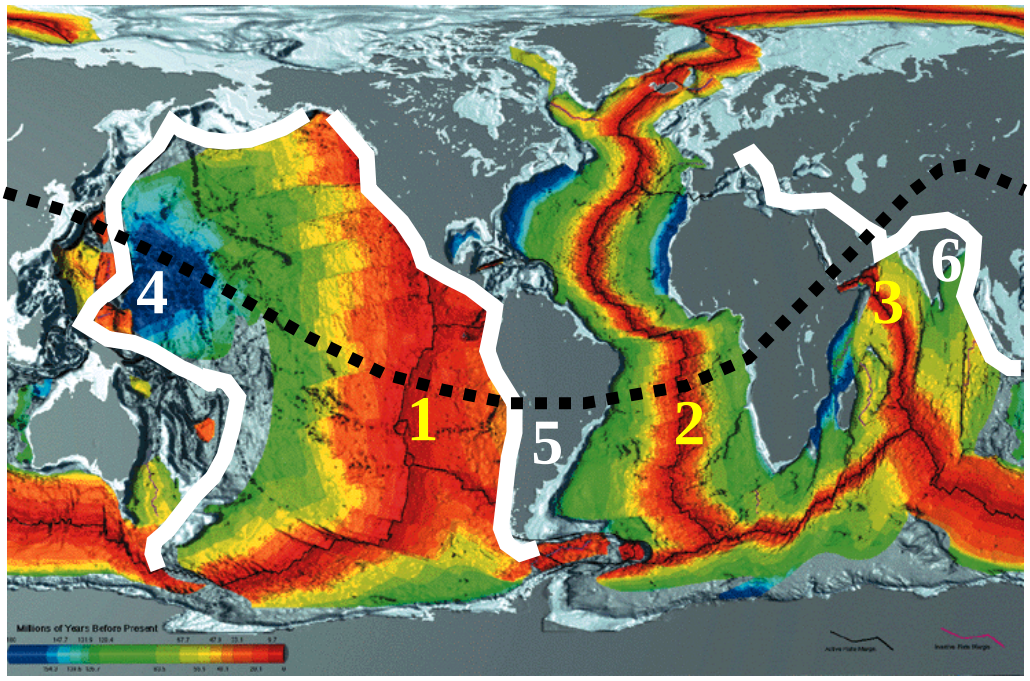

Figure 3.2: Construction of a *tectonic mainstream*, starting from the Pacific motion direction and linking all the other relative motions in a global circuit using first order tectonic features such as the East Pacific Rise (1), the Atlantic rift (2), the Red Sea, the Indian Ocean rift (3) for the rift zones, and the west Pacific subduction (4), the Andean subduction (5), and the Zagros-Himalayas subduction (6) for convergent margins. See text for description.

In the extensional tectonic settings, we assume that transform faults are parallel to the relative plate motions, whereas in convergent settings, the relative plate motions are constrained by the dominant trend of folds and

thrusts, where no significant transpressive tectonics occurs. Another prominent large scale plate boundary is the SW-Indian ridge which is not included in this present first order analysis because it has very slow spreading rates and it is possibly related to the subrotations of Africa and Antarctica.

Starting from the Pacific WNW-ESE plate motion relative to the mantle and constrained by the Hawaiian and Society tracks, and moving ESE, the relative E-ward motion of the Nazca plate (in the NNR reference frame) can be transferred to an "absolute" kinematic analysis. Continuing to the E, the motion of the Nazca plate relative to South America (Kendrick et al., 2003), allows to refer the motion of the South America again to the Pacific and so on. The major plate boundaries can then be connected in a global circuit. In this way it appears that plate motions describe a flow, exemplified by an imaginary line (Figure 3.2), passing throughout all the major tectonic features of Earth.

This flow line crosses the East Pacific Rise (EPR), where the rifting is about E-W, the Andean subduction (AS), the Middle Atlantic Ridge (MAR), again both almost E-W. Then the Red Sea and East Africa rift (RSEAR) open along the NE-SW trend, similarly to the Indian Ocean. The direction gradually moves to a NNE-SSW trend in the Zagros-Himalayas (HimS) subduction zones. In Asia it rapidly turns to E-W and to NW-SE (Baikal rift, BR, and the Japan Subduction, JS), eventually closing the circuit in the Pacific between the Hawaiian and Society Hotspots (HH) (Figure 3.2). The flow line can be envisaged only filtering the transtensive or transpressive tectonic settings. For example, the East Africa Rift is characterized by left-lateral transtension where crossed by the flow line. Left-lateral transpression, as another example, characterizes the tectonic setting along the Chaman transform zone of Afghanistan-Pakistan where the NE-SW trending line enters into the Zagros-Himalayas orogens.

The flow line is stable back to at least 47 Myr (before the Hawaii-Emperor bending). However the Hawaii-Emperor bending has been shown not to be associated to a coeval rotation of the Pacific plate (Norton, 1995). Moreover, apart minor oscillations, the flow seems to be stable since at least the Late Permian in the Atlantic rifting realm both in the earlier continental and later oceanic stages and along the Asian Cimmerides subduction zones. The trend inferred from these tectonic indicators is rather coherent with the directions obtained from space geodesy data in the NNR reference frame.

Regardless its nature and speed, combined with the hotspots tracks, the westward drift indicates the existence of a decoupling surface between lithosphere and sub-asthenospheric mantle.

3.3 The hotspot reference frame (HSRF)

In principle, the definition any plate kinematic model with respect to the mantle, should be based on an optimal choice of the hotspot candidates to realize a suitable reference frame. The plate on which the selected hotspots are located becomes the reference plate defining the known tangential velocity with respect to the mantle and any potential depth assigned to the hotspot source reflects directly on the velocity assumed by the reference plate with respect of the mantle. For this purpose it is fundamental to know whether hotspots i) are anchored to the mantle, ii) are stationary with respect to each other, and iii) have shallow or deep roots. Looking at maps of hotspots (e.g., Anderson and Schramm, 2005), plumes occur either in intraplate settings, or close or along plate boundaries. A number of models have been produced to quantify the relative motion among hotspots and their reliability to generate a reference frame (Norton, 2000; Wang and Wang, 2001; Gripp and Gordon, 2002; Courtillot et al., 2003). As a consequence, not all the volcanic chains identified as hotspots may be selected as a reliable reference frame. Gripp and Gordon (2002; Table 11) defined the last hotspot reference frame HS3 using eleven segment trends and two volcanic propagation rates.

Concerning the source depth of hotspots (Foulger et al., 2005), whether hotspots are sourced either from the deep mantle or the asthenosphere, it has to be underlined that plate motion modeling does not necessarily require to know the depth of the hotspot source; this parameter acts indirectly on the velocity of the reference plate. Therefore, any absolute plate motion model calibrated for a variable velocity takes into account indirectly of this discussed question (see Chaper 1).

3.4 Plate motion kinematic model

The wide use of space geodesy techniques devoted to geophysical and geodynamical purposes has recently evidenced some limitations due to the

intrinsic TRF definition. It is noteworthy that current reference frames based on space geodesy techniques, as the ITRFyy, are defined under hypotheses suited to overcome the rank deficiency of the observations with respect to the parameters that have to be estimated, i.e. coordinates and velocities (Dermanis, 2001; Dermanis, 2002). From a geodetic point of view, one possibility implies the application of the no-net-rotation condition (NNRC) (Altamimi et al., 2002). This condition is realized by aligning the global inter-technique ITRF2000 solutions to the NNR-Nuvel-1A model (i.e., by imposing null rotation rate components between ITRF2000 and NNR-Nuvel-1A). The application of this condition, besides the known limitations (Dermanis, 2002; Altamimi et al., 2002), has some geophysical consequences; in fact the ITRFyy allows for accurate estimations of relative plate motions only (Altamimi et al., 2002), whilst any absolute motion (for instance with respect to the inner layers of the Earth body, in particular the mantle) is not determinable.

In this study we try to overcome such limitations introduced by the application of the NNRC, starting from a simple global kinematic model in which we introduce the net rotation of the lithosphere with respect to the mantle. Particularly, we hypothesize that each plate motion may be mainly described by a first order term, accounting for the ordered net rotation at global scale (represented by an angular velocity vector different from plate to plate), and a second order term, accounting for possible plate sub-rotations (Cuffaro et al., 2004), around a rotational axis centered on the plate (Cuffaro et al., 2008), which is here neglected.

First order plate motion follows an imaginary line representing their main trajectory (*tectonic mainstream*), according to what discussed in section 3.2; this line may allow a simple analytical representation as a low (e.g., 3rd) order Fourier series in geographic coordinates (φ, λ)

$$\varphi(\lambda) = \frac{a_0}{2} + \sum_{i=1}^{3}(a_i \cos(i\lambda) + b_i \sin(i\lambda)) \quad (1)$$

The 7 parameters in (1) may be computed starting from the concept of Eulerian equator plane of each plate, which is just the plane orthogonal to plate absolute (w.r.t. the mantle) angular velocity; in a spherical Earth approximation, all absolute angular plate velocities pass through the Earth center as their correspondent Eulerian equatorial planes (Figure 3.3). If we consider all the plates crossed by the *mainstream* and the traces of their Eulerian equatorial planes on the sphere (Eulerian equators), the *tectonic mainstream* line may be regarded as the line globally approximating the

Eulerian equators themselves. Therefore, the 7 parameters in (1) may be derived after the absolute angular velocities estimation, as described in section 3.6.

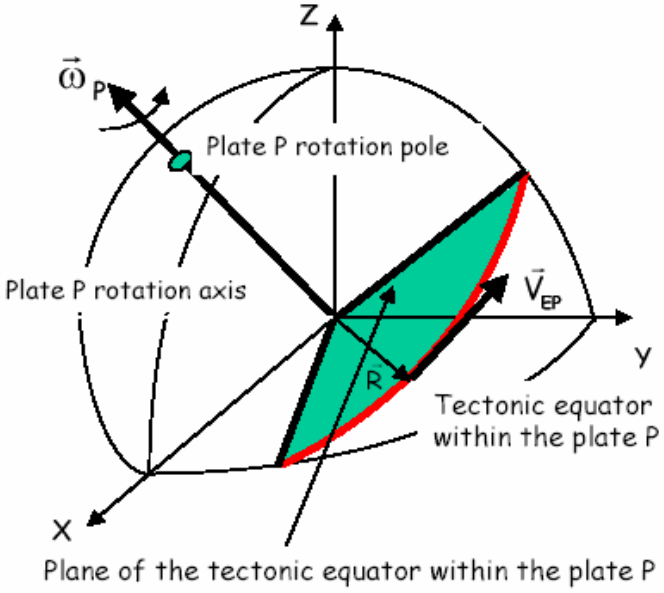

Figure 3.3: Kinematic condition between *tectonic mainstream* (red line) and angular velocity of a given plate, under spherical approximation.

In order to set up the model to perform this estimation, we start from the transformation between two velocity sets (NNR and HSRF), which reads

$$\vec{V} = \vec{V}_{NNR} + \vec{V}_d \quad (2)$$

where $\vec{V}$ is the absolute (i.e. HSRF), $\vec{V}_{NNR}$ is the NNR velocity whose components are $(V_{X_{NNR}}, V_{Y_{NNR}}, V_{Z_{NNR}})$ and $\vec{V}_d$ is the drag term, due to the net-rotation of lithosphere w.r.t. the mantle.

Let us consider for simplicity P plates with i sites, thus we can express (2) in terms of the absolute angular velocity $\vec{\omega}^p$ and geocentric position $\vec{r}_i$ as

$$\vec{\omega}^p \times \vec{r}_i - \vec{\omega}^d \times \vec{r}_i = \vec{V}_{i_{NNR}} \quad (3)$$

where $\vec{\omega}^d$ is the drag angular velocity.

We recall that the components of $\vec{V} = \vec{\omega} \times \vec{r}$ are

$$\begin{vmatrix} V_X \\ V_Y \\ V_Z \end{vmatrix} = \begin{vmatrix} i & j & k \\ \omega_X & \omega_Y & \omega_Z \\ X & Y & Z \end{vmatrix}$$

with i, j, k versors of X, Y, Z axes, so that

$$\begin{aligned} V_X &= Z \cdot \omega_Y - Y \cdot \omega_Z \\ V_Y &= X \cdot \omega_Z - Z \cdot \omega_X \\ V_Z &= Y \cdot \omega_X - X \cdot \omega_Y \end{aligned}$$

or, equivalently, separating the $\vec{\omega}$ components,

$$\begin{vmatrix} V_X \\ V_Y \\ V_Z \end{vmatrix} = \begin{vmatrix} 0 & Z & -Y \\ -Z & 0 & X \\ Y & -X & 0 \end{vmatrix} \cdot \begin{vmatrix} \omega_X \\ \omega_Y \\ \omega_Z \end{vmatrix}$$

Thus, the relationship (3) in matricial form becomes

$$\begin{vmatrix} 0 & Z_i^p & -Y_i^p \\ -Z_i^p & 0 & X_i^p \\ Y_i^p & -X_i^p & 0 \end{vmatrix} \cdot \left(\begin{vmatrix} \omega_X^p \\ \omega_Y^p \\ \omega_Z^p \end{vmatrix} - \begin{vmatrix} \omega_X^d \\ \omega_Y^d \\ \omega_Z^d \end{vmatrix} \right) = \begin{vmatrix} V_{X_i} \\ V_{Y_i} \\ V_{Z_i} \end{vmatrix}_{NNR} \qquad (4)$$

This model explicitly relates the plate absolute angular velocities $\vec{\omega}^p$, the drag angular velocity $\vec{\omega}^d$ (net-rotation angular velocity) and the velocity "observed" by GPS under NNR condition at some selected sites.
It clearly shows a rank deficiency w.r.t. the angular velocities in sense that one of them has to be fixed in order to estimate the others, being equal the velocity differences; in particular, it is easy to verify that, if the arbitrary vector

$$n = \begin{vmatrix} \Delta\omega_X \\ \Delta\omega_Y \\ \Delta\omega_Z \end{vmatrix}$$

is added to all (plate and drag) absolute angular velocities, the left side of equation (4) does not change.
On the other hand, we can fix the rank deficiency by introducing suitable additional constraints on the absolute plate angular velocities ($\vec{\omega}^a, \vec{\omega}^b$), what

may be done under the hypothesis of the existence of a *tectonic mainstream* representing the first order absolute plate motions.
These constraints regard:

1. continuity of the Eulerian equators, i.e. they must connect each other at plate boundaries
2. azimuths of the Eulerian equators at some longitudes, mainly forced by the principal tectonic features
3. attitude (and its precision) of the Pacific plate Eulerian equatorial plane, based on the motion directions (azimuths) of two well recognized hotspots within the Pacific plate (Hawaii and Society Islands)
4. velocities of Hawaii and Society Islands hotspots, based on different hypotheses of their source depths (deep mantle or mid-asthenosphere).

3.4.1 Continuity of the Eulerian equators

Since the Eulerian equator plane of each plate is orthogonal to the plate absolute angular velocity and crosses the Earth center, the Eulerian equator plane equation in the geocentric Cartesian coordinates system reads

$$\omega_X X + \omega_Y Y + \omega_Z Z = 0 \qquad (5)$$

where, in spherical approximation (mean Earth radius R = 6371 km)

$$\begin{vmatrix} X \\ Y \\ Z \end{vmatrix} = R \begin{vmatrix} \cos\varphi\cos\lambda \\ \cos\varphi\sin\lambda \\ \sin\varphi \end{vmatrix}$$

therefore, equation (5) in geographic coordinates (φ, λ) becomes

$$\omega_X \cos\varphi\cos\lambda + \omega_Y \cos\varphi\sin\lambda + \omega_Z \sin\varphi = 0 \qquad (6)$$

This equation is just useful to write down the continuity constraints; in fact, at the boundary between plates a and b $(\varphi^{ab}, \lambda^{ab})$ (note that in our model intersection between each plate boundary and plate Eulerian equator is represented by one point) the continuity condition states that

$$\begin{aligned} &\omega_X^a \cos\varphi^{ab}\cos\lambda^{ab} + \omega_Y^a \cos\varphi^{ab}\sin\lambda^{ab} + \omega_Z^a \sin\varphi^{ab} = \\ &= \omega_X^b \cos\varphi^{ab}\cos\lambda^{ab} + \omega_Y^b \cos\varphi^{ab}\sin\lambda^{ab} + \omega_Z^b \sin\varphi^{ab} \end{aligned} \qquad (7a)$$

or, under the hypothesis in our case always satisfied, that $\cos\varphi^{ab} \neq 0$ ($\varphi^{ab} \neq \pm\frac{\pi}{2}$) and $\omega_Z^a, \omega_Z^b \neq 0$

$$\begin{aligned} \cos\lambda^{ab}\frac{\omega_X^a}{\omega_Z^a} + \sin\lambda^{ab}\frac{\omega_X^a}{\omega_Z^a} &= -\mathrm{tg}\varphi^{ab} \\ \cos\lambda^{ab}\frac{\omega_X^b}{\omega_Z^b} + \sin\lambda^{ab}\frac{\omega_X^b}{\omega_Z^b} &= -\mathrm{tg}\varphi^{ab} \end{aligned} \qquad (7b)$$

more useful form the computational point of view; in this respect it has to be underlined that the system (7a) and the equivalent (7b) are not linear w.r.t. the unknown parameters ($\omega_X^a, \omega_Y^a, \omega_Z^a, \omega_X^b, \omega_Y^b, \omega_Z^b, \varphi^{ab}, \lambda^{ab}$); the necessary approximated values are supplied joining information stemming from geology and space geodesy.

3.4.2 Azimuth constraints on the Eulerian equators

The second kind of constraints interprets an additional geological condition that, in our opinion, must be satisfied: the *tectonic mainstream* direction must be equal to the mean azimuth α of motion across the largest Earth crust tectonic discontinuities (Gordon, 1995; Searle, 1986), as reported in detail in section 3.2.

Therefore, again representing with one point the intersection between the Eulerian equator and a tectonic discontinuity, the second kind of constraints states that the Eulerian equator azimuth has known value α^t in some selected points (φ^t, λ^t) (Table 3.1 and Figure 3.4 a). By applying simple geometric considerations, the azimuth constraint equation reads

$$\sin\lambda^t\cos\varphi^t\frac{\omega_X}{\omega_Z} - \cos\lambda^t\cos\varphi^t\frac{\omega_Y}{\omega_Z} = \mathrm{cotg}\alpha^t \qquad (8)$$

Note that if the discontinuity coincides with a plate boundary, equation (8) must be satisfied on both sides, that is for both plates a and b

$$\begin{aligned} \sin\lambda^t\cos\varphi^t\frac{\omega_X^a}{\omega_Z^a} - \cos\lambda^t\cos\varphi^t\frac{\omega_Y^a}{\omega_Z^a} &= \mathrm{cotg}\alpha^t \\ \sin\lambda^t\cos\varphi^t\frac{\omega_X^b}{\omega_Z^b} - \cos\lambda^t\cos\varphi^t\frac{\omega_Y^b}{\omega_Z^b} &= \mathrm{cotg}\alpha^t \end{aligned}$$

in this case, the two equations constraint both azimuth and continuity at the plate boundary.

Table 3.1: Azimuth of the selected tectonic features

	λ (°)	φ (°)	α (°)
1	348	-29	74 ± 3
2	56	12	40 ± 3
3	80	33	61 ± 3
4	142	35	103 ± 5
5	195	16	109 ± 5
6	245	-17	113 ± 3
7	288	-25	99 ± 5

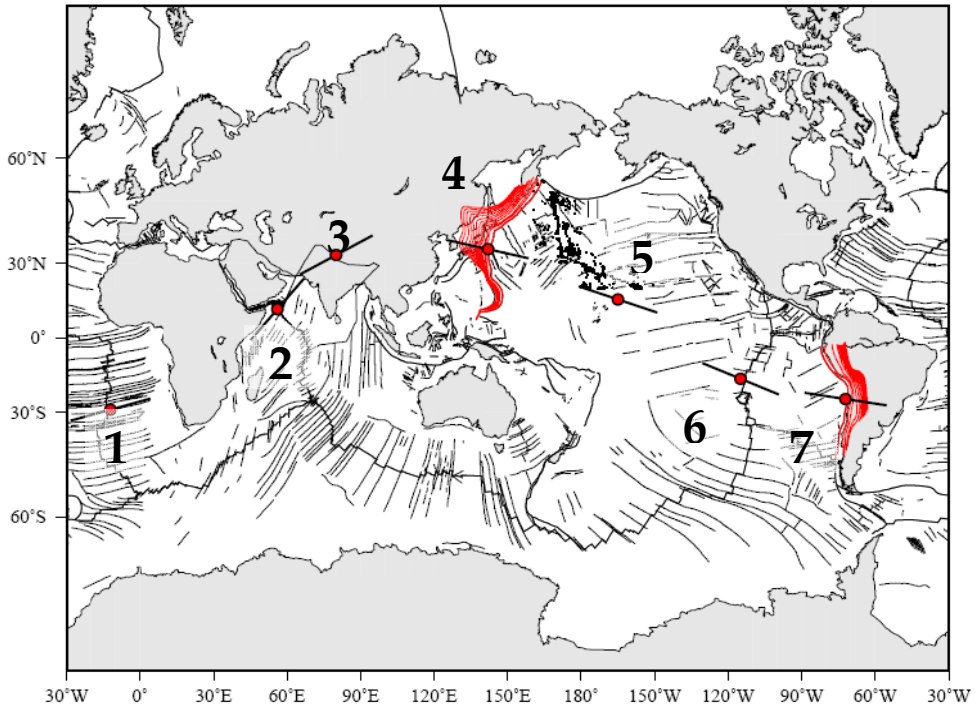

Figure 3.4 a: Map of the main tectonic features (listed in Table 3.1) selected to introduce azimuth constraints into the *tectonic mainstream* estimation.

3.4.3 Attitude of the Pacific plate Eulerian equatorial plane

The attitude of the Pacific plate Eulerian equatorial plane in terms of absolute angular velocity components ratios $(\frac{\omega_X}{\omega_Z}, \frac{\omega_Y}{\omega_Z})$ may be derived with its approximated uncertainty (angular velocity components ratio standard deviations) by equation (8), on the basis of the data concerning the motion azimuths of two well recognized hotspots within the Pacific plate (Hawaii and Society Islands) published in Gripp and Gordon (2002). As regards the attitude precision, note that the azimuths of the observed trends of these hotspots show the best precision in the whole hotspots set, consequently we prefer to base our present modelling on this conservative choice (Table 3.2 and Figure 3.4 b).

Table 3.2: Selected HS3-NUVEL1 active to 5 Myr

HS	Lat (°)	Lon (°)	Azimuth (deg)	Rate (km/Myr)
Hawaii	20.65	156.91	300.3±4.4	103.3±4.4
Society	-17.33	-149.55	292.6±7.8	117.9±5.6

Then, recalling equation (8) and applying the covariance propagation law under the hypothesis that angular velocity components ratio are independent, we may write down two equations for Hawaii (superscript H) and Society Islands (superscript S) respectively

$$\begin{aligned}
(\sin\lambda^H \cos\varphi^H)^2 \sigma^2\left(\frac{\omega_X}{\omega_Z}\right)_{PA} - (\cos\lambda^H \cos\varphi^H)^2 \sigma^2\left(\frac{\omega_Y}{\omega_Z}\right)_{PA} &= \frac{1}{\text{sen}^4\alpha^H}\sigma^2\left(\alpha^H\right) \\
(\sin\lambda^S \cos\varphi^S)^2 \sigma^2\left(\frac{\omega_X}{\omega_Z}\right)_{PA} - (\cos\lambda^S \cos\varphi^S)^2 \sigma^2\left(\frac{\omega_Y}{\omega_Z}\right)_{PA} &= \frac{1}{\text{sen}^4\alpha^S}\sigma^2\left(\alpha^S\right)
\end{aligned} \tag{9}$$

in the two unknowns $\sigma\left(\frac{\omega_X}{\omega_Z}\right)_{PA}$ and $\sigma\left(\frac{\omega_Y}{\omega_Z}\right)_{PA}$.

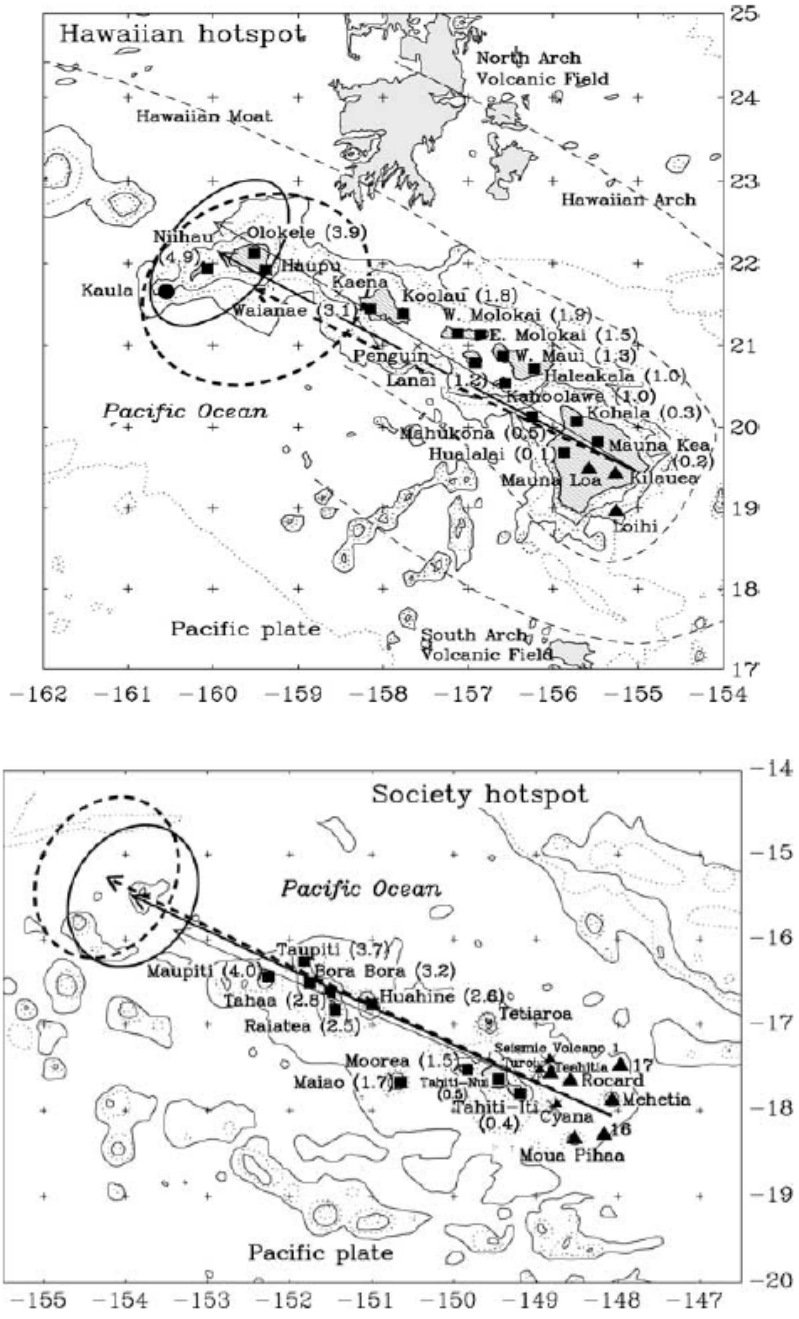

Figure 3.4 b: Thin arrows show the observed trends and volcanic propagation rates (see Table 3.2). Thick arrows show the motion calculated from HS3-NUVEL1A. Dashed arrows show the motion predicted by removing respectively the Hawaii (up) and the Society (down) rates and trends (from Gripp and Gordon, 2002).

3.4.4 Velocities of Hawaii and Society Islands hotspots

The classical velocities for the Hawaii and Society Islands hotspots are those referred to a deep source (Gripp and Gordon, 2002) and reported in Table 3.2.

Different velocities for Hawaii and Society Islands hotspots w.r.t the mantle may be hypothesized on the basis of different source depths.

As example, we show in Figure 3.5a simple sketch of the East Pacific Rise (EPR) plate kinematics, where it is easy to observe that the same relative motion may lead to different absolute velocities according to the different hypotheses, NNR, deep and shallow hotspot source depths (Doglioni et al., 2005). This constraint may be simply given by the ω_Z component of Pacific plate absolute angular velocity since the component ratios $(\frac{\omega_X}{\omega_Z}, \frac{\omega_Y}{\omega_Z})$ with their precisions are already constrained by equation (8), as above discussed.

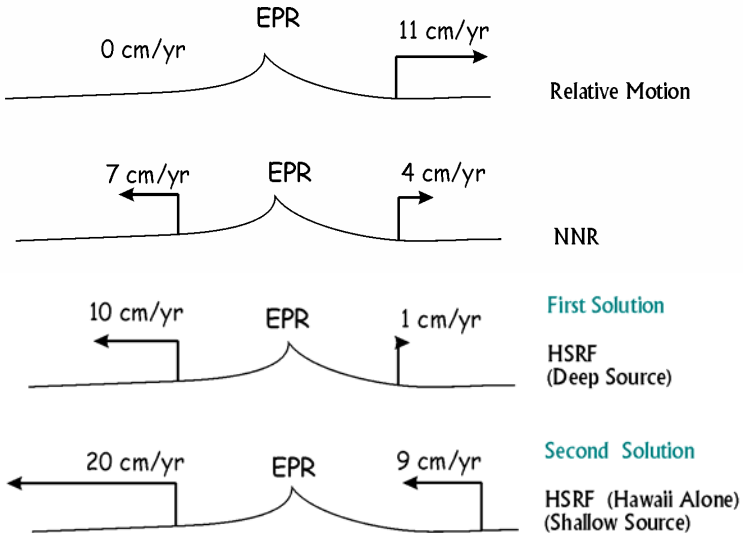

Figure 3.5: Sketch of East Pacific Rise plate kinematics; from top to bottom: relative motion, NNR motion, HSRF first solution, HSFR (Hawaii) second solution (after Doglioni et al., 2005).

3.5 Kinematic parameters estimation

Having exploited both the pure rank deficient kinematic model (4) and the constraints (7) and (8) which play a relevant role in the plate and drag absolute angular velocities determination, all the parameters involved in the model (plate and drag absolute angular velocities themselves and the geographic coordinates of points at plate boundaries where the Eulerian equator continuity condition is imposed) may be estimated according to the least squares principle, starting from approximated values, being the model non linear.In this respect, the solution has been carried out iteratively in a two-steps procedure.

First of all, the equations (8) were written for the 6 boundaries between plates crossed by *tectonic mainstream*, plus the mean azimuth of the Hawaii and Society Islands motions; these equations were solved separately from equations (4), in order to estimate the unknown plate absolute angular velocity component ratios which fulfil both the azimuths and the continuity constraints ($\tilde{\omega}_{XZ} = \left(\frac{\omega_X}{\omega_Z}\right)_{ac}$, $\tilde{\omega}_{YZ} = \left(\frac{\omega_Y}{\omega_Z}\right)_{ac}$), starting from the approximated values of geographic coordinates of the points at plate boundaries where the Eulerian equator continuity condition is imposed.

Then, the pseudo-observation equations on absolute angular velocity components of the form:

$$\begin{aligned} \omega_X &= \tilde{\omega}_{XZ}\omega_Z \\ \omega_Y &= \tilde{\omega}_{YZ}\omega_Z \end{aligned} \quad (10)$$

are added to equations (4) to solve the global model, estimating plate and drag absolute angular velocities.

The general (linear) form of the model for the second step reads

$$\begin{aligned} Y_0 + v &= Ax \quad \text{(functional model)} \\ C_{y_0y_0} &= \sigma_0^2 Q \quad \text{(stochastic model)} \end{aligned}$$

where Y_o is the (pseudo-)observations vector, v is the vector of residuals, A is the design matrix, x is the parameter vector, $C_{y_0y_0}$ is the observations covariance matrix, σ_0^2 is the prior variance of unit weight and Q is the observation cofactor matrix.

As regards the functional model, the equations (4) were written for 28 GPS sites located on major plates (3 for Pacific, Eurasia, India, Africa, South America, North America, Australia and Antarctica, 2 for Nazca and Arabia, the only available on these plates) far from high deformation areas, so that all plates involved has a similar number of sites. The selected sites have long enough coordinate time series with reliable ITRF2000 velocity components.

Table 3.3: GPS sites, coordinates, velocities ITRF00 and rms

PLATE	SITE	Lat. (°)	Lon. (°)	Vx m/kyr	rms m/kyr	Vy m/kyr	rms m/kyr	Vz m/kyr	rms m/kyr
PA	MKEA	19.801	-155.456	-14.85	0.10	63.04	0.06	31.07	0.04
PA	KWJ1	8.722	167.730	21.76	0.32	66.81	0.16	27.41	0.08
PA	THTI	-17.577	-149.606	-42.10	0.18	52.72	0.13	31.98	0.08
NZ	EISL	-27.148	-109.383	64.21	0.05	-19.51	0.09	-6.22	0.05
NZ	GALA	-0.743	-90.304	50.73	0.10	1.36	0.20	11.15	0.03
SA	BOGT	4.640	-74.081	-9.20	0.09	3.32	0.16	10.08	0.03
SA	FORT	-3.877	-38.426	-2.92	0.08	-4.53	0.07	11.94	0.02
SA	RIOG	-53.785	-67.751	6.80	0.08	-10.62	0.11	2.71	0.15
AF	MAS1	27.764	-15.633	-2.48	0.07	16.94	0.04	15.72	0.04
AF	NKLG	0.354	9.672	-1.56	0.29	20.63	0.19	17.68	0.06
AF	SUTM	-32.381	20.811	5.62	0.54	17.38	0.33	13.28	0.35
AR	AMMN	32.029	35.880	-23.59	0.69	11.30	0.57	11.71	0.50
AR	BAHR	26.209	50.608	-30.84	0.07	10.06	0.08	25.95	0.05
EU	KUNM	25.030	102.797	-31.84	0.14	5.00	0.26	-15.97	0.13
EU	IRKT	52.219	104.316	-25.72	0.04	1.05	0.06	-3.96	0.08
EU	WTZR	49.144	12.879	-15.32	0.06	17.32	0.04	9.78	0.07
IN	BAN2	13.034	77.512	-34.96	0.61	1.27	1.10	35.47	0.34
IN	HYDE	17.417	78.551	-35.24	0.93	1.12	1.88	32.62	0.72
IN	IISC	13.021	77.570	-40.82	0.07	2.48	0.13	33.12	0.04
AU	DARW	-12.844	131.133	-35.38	0.17	-13.01	0.18	53.82	0.07
AU	PERT	-31.802	115.885	-47.03	0.04	7.16	0.06	50.37	0.04
AU	TOW2	-19.269	147.056	-31.68	0.16	-13.25	0.12	50.33	0.07
NA	ALGO	45.956	-78.071	-16.34	0.03	-4.61	0.04	3.39	0.04
NA	MDO1	30.681	-104.015	-12.88	0.03	-1.65	0.05	-5.39	0.03
NA	PRDS	50.871	-114.293	-16.97	0.09	-1.17	0.13	-7.61	0.15
AN	DAV1	-68.577	77.973	0.82	0.04	-5.28	0.05	-3.48	0.10
AN	VESL	-71.674	-2.842	8.15	0.07	-3.04	0.06	3.17	0.19
AN	KERG	-49.351	70.256	-5.46	0.07	-0.38	0.10	-4.06	0.11

Table 3.3 shows the list of sites and the corresponding ITRF2000 velocities available at the moment of our estimation, according to the solution provided

by JPL (Heflin et al., 2004). Moreover, the pseudo-observation equations (10) were written for the 6 plates crossed by *tectonic mainstream*. Finally, we added one more pseudo-observation equation on the ω_Z component of the Pacific plate absolute angular velocity, constraining this parameter to a value driven by the hypothesis about hotspot source depths (Doglioni et al., 2005).

Concerning the stochastic model, in order to assess both the mean inner precision of the pure kinematic model and the reliability of the selected GPS sites, a preliminary adjustment with $\vec{\omega}^d = 0$ and Q=I was performed; in this respect we recall that the velocity precisions of ITRF00 (usually of the order of tenths of mm/yr) are overestimated by far, as discussed in Barzaghi et al. (2004). Consequently, coherently with the results in Barzaghi et al. (2004), we have re-estimated the variance of unit weight obtaining $\hat{\sigma}_0 = 2.8$ mm/yr that we have introduced as prior value into the global estimation procedure.

Moreover, equations (9) supplied the two unknowns:

$$\begin{aligned} \sigma\left(\frac{\omega_X}{\omega_Z}\right)_{PA} &\cong 0.15 \\ \sigma\left(\frac{\omega_Y}{\omega_Z}\right)_{PA} &\cong 0.17 \end{aligned} \qquad (11)$$

Then, we defined the full stochastic model, considering all the equations independent. We set up the variance of the kinematic equations (4) equal to $\hat{\sigma}_0^2$, whereas for the pseudo-observation equations (10), the variance was derived by the variance propagation law, from (11) and accounting both $\sigma(\omega_Z)_p$ uncertainties (iteratively estimated for each plate p) and the areas ratio $\frac{A_p}{A_{PA}}$ between each plate p and the Pacific one (Schettino, 1999):

$$\begin{aligned} \sigma\left(\frac{\omega_X}{\omega_Z}\right)_p &= \frac{A_p}{A_{PA}}\sigma\left(\frac{\omega_X}{\omega_Z}\right)_{PA} \\ \sigma\left(\frac{\omega_Y}{\omega_Z}\right)_p &= \frac{A_p}{A_{PA}}\sigma\left(\frac{\omega_Y}{\omega_Z}\right)_{PA} \end{aligned} \qquad (12)$$

In this way we want to take into account that larger plate motions (Forsyth and Uyeda, 1975) are likely to follow the first order net rotation at global scale than narrower (which may experience significant sub-rotations here not considered), so that absolute angular velocity components ratios $(\frac{\omega_X}{\omega_Z}, \frac{\omega_Y}{\omega_Z})$

derived at first step are as much reliable as wide plate is. Finally, ω_Z for the Pacific plate was just fixed by a suitable high weight.

3.6 Plate kinematic solutions and analytical representation of the *tectonic mainstream*

We have considered different hypotheses about the Pacific plate ω_Z component, leading to the following 3 absolute plate kinematic solutions (Figures 3.6 a, b, c; 3.7, 3.8 a, b, c; Tables 3.4 a, b, c and 3.5).

1. Gripp and Gordon "style" solution (GGS) – The absolute angular velocity component ω_Z of the Pacific plate is chosen so that the prior maximum velocity within the Pacific plate (velocity along the Eulerian equator) is the same as in Gripp and Gordon (2002), about 11.2 cm/yr. Note that the posterior maximum velocity (4) is slightly different since the uncertainties of the absolute angular velocity component ratios of the Pacific plate $((\frac{\omega_X}{\omega_Z})_{PA}, (\frac{\omega_Y}{\omega_Z})_{PA})$ are accounted for, therefore their values are re-estimated together with all other absolute angular velocity component ratios. This solution fulfils the global test on the model, under the hypothesis of Gaussian error distribution, w.r.t. the prior value $\hat{\sigma}_0 = 2.3$ mm/yr at the 95% significance level

$$r\frac{(\hat{\sigma}^2_{0GM})_{GG}}{\hat{\sigma}^2_0} = \chi^2_{exp} \le \chi^2_{r,95\%}$$

where r is the redundancy of the least square problem $(r = 70)$ at 95% significance level and $(\hat{\sigma}_{0GM})_{GGS} = 2.47$ mm/yr. In terms of agreement between the overall solution and the azimuth constraints, the weighted RMSE of the estimated azimuth w.r.t. the a priori chosen results is $\mathrm{WRMSE}(\alpha)_{GGS} = 4.68$ (Table 3.4 a); note that WRMSE is normalized, in fact each residual between prior and estimated azimuth is weighted by the inverse of its variance.
2. 15 cm/yr solution (S15) - In this case ω_Z is chosen so that the maximum velocity within the Pacific plate is 15 cm/yr; the estimated standard

deviation of unit weight of the global model $\hat{\sigma}_{0GM}$ is $(\hat{\sigma}_{0GM})_{15S} = 2.33\,\text{mm/yr}$ and obviously fulfils the global test on the model too. In terms of agreement between the overall solution and the azimuth constraints, we obtain $\text{WRMSE}(\alpha)_{15S} = 2.25$ (Table 3.4 b).

3. 20 cm/yr solution (S20) - In this case ω_Z is chosen so that the maximum velocity within the Pacific plate is 20 cm/yr; the estimated standard deviation of unit weight of the global model $\hat{\sigma}_{0GM}$ is $(\hat{\sigma}_{0GM})_{20S} = 2.18\,\text{mm/yr}$ and $\text{WRMSE}(\alpha)_{20S} = 1.95$ (Table 3.4 c).

Comparing these solutions, we can make some remarks.

Even if all solutions fulfil the global test on the model, it is clearly evident that S15 and S20 exhibit a finer agreement with the geological constraints (azimuths, Eulerian equators continuity and attitude of the Pacific plate Eulerian equator). In this respect, it is also evident that S15 and S20 are quite similar, even if the Pacific plate maximum velocity difference between them (5 cm/yr) is about 1.5 larger than between GGS and S15 (3.8 cm/yr). Therefore, the agreement between space geodesy solution and geological constraints seems require that Pacific plate be faster than derived in Gripp and Gordon (2002). In the same time, since solutions with faster and faster Pacific plate does not differ significantly as regards the agreement between space geodesy solution and geological constraints, it is not possible to clearly assess an upper limit for the Pacific plate velocity and for the derived plate kinematics uniquely on their basis; in fact it is possible to retrieve other quite similar solutions with higher maximum Pacific plate velocity, but here only the S20, as hypothesized in Doglioni et al. (2005) and the intermediate S15 are discussed. The main differences between GGS and S15/S20 regard the Indian and Nazca plates. In GGS at their plate boundaries significant discontinuities of the Eulerian equators are still present in latitude. In fact, if we take into account that 26° is the mean latitude discontinuity at the plate boundaries, for Nazca plate we have 25° and 41° w.r.t. South American and Pacific plates respectively and for Indian plate we have 79° and 73° w.r.t. Eurasian and African plates respectively. Moreover, in GGS the Nazca plate moves essentially eastward, different form all other plates and the other solutions (Figure 3.6 a, b, c). Remarkable differences are also found for the estimated net rotations, in terms of maximum tangential velocities reaching 4.1 cm/yr for GGS, 8.0 cm/yr for S15 and 13.4 cm/yr for S20 (Table 3.4 a, b, c). The net rotation poles for S15 and S20 are located quite close (approximately 450 km apart), whilst the GGS net rotation pole is about 800 km far from the S15 pole (Table 3.5 and Figure 3.8 a, b, c).

Table 3.4 a: Solution GGS, plate angular velocity components, rms and max. tangential velocities

PLATE		ω °/Myr	rms °/Myr	V_{tmax} cm/yr	rms cm/yr
	ω_X	-0.2036	0.0441		
PA	ω_Y	0.4765	0.0332		
	ω_Z	-0.9066	0.0001	11.6	0.2
	ω_X	-0.1868	0.0372		
NZ	ω_Y	-0.2384	0.0591		
	ω_Z	0.1559	0.0244	3.8	0.5
	ω_X	-0.1617	0.0368		
SA	ω_Y	0.1010	0.0370		
	ω_Z	-0.3509	0.0203	4.4	0.3
	ω_X	-0.0804	0.0282		
AF	ω_Y	0.0367	0.0281		
	ω_Z	-0.1101	0.0191	1.6	0.3
	ω_X	0.0451	0.0415		
AR	ω_Y	0.0425	0.0274		
	ω_Z	-0.0230	0.0291	0.7	0.4
	ω_X	-0.1708	0.0358		
EU	ω_Y	0.0356	0.0357		
	ω_Z	-0.0945	0.0248	2.2	0.4
	ω_X	0.2434	0.0791		
IN	ω_Y	0.3011	0.3306		
	ω_Z	0.0887	0.0884	4.4	3.5
	ω_X	0.3110	0.0477		
AU	ω_Y	0.5095	0.0482		
	ω_Z	0.0398	0.0265	6.7	0.4
	ω_X	-0.0697	0.0359		
NA	ω_Y	0.0124	0.0498		
	ω_Z	-0.3209	0.0403	3.7	0.5
	ω_X	-0.0763	0.0140		
AN	ω_Y	-0.0766	0.0183		
	ω_Z	0.1719	0.0356	2.3	0.4
	ω_X	-0.0936	0.0330		
Net rot	ω_Y	0.1948	0.0300		
	ω_Z	-0.2951	0.0133	4.1	0.3
σ_0			2.47		
WRMSE			4.68		

Table 3.4 b: Solution S15, plate angular velocity components, rms and max. tangential velocities

PLATE		ω °/Myr	rms °/Myr	V_{tmax} cm/yr	rms cm/yr
	ω_X	-0.3536	0.0671		
PA	ω_Y	0.5944	0.0712		
	ω_Z	-1.2115	0.0001	15.5	0.4
	ω_X	-0.3387	0.0635		
NZ	ω_Y	-0.1202	0.0806		
	ω_Z	-0.1479	0.0231	4.3	0.7
	ω_X	-0.3144	0.0637		
SA	ω_Y	0.2176	0.0729		
	ω_Z	-0.6549	0.0192	8.4	0.4
	ω_X	-0.2425	0.0623		
AF	ω_Y	0.1503	0.0702		
	ω_Z	-0.4136	0.0183	5.6	0.5
	ω_X	0.0517	0.0802		
AR	ω_Y	0.3119	0.0763		
	ω_Z	-0.2051	0.0497	4.2	0.7
	ω_X	-0.3236	0.0632		
EU	ω_Y	0.1530	0.0722		
	ω_Z	-0.3981	0.0234	6.0	0.5
	ω_X	0.0908	0.0918		
IN	ω_Y	0.4180	0.3189		
	ω_Z	-0.2153	0.0835	5.3	2.8
	ω_X	0.1583	0.0699		
AU	ω_Y	0.6264	0.0787		
	ω_Z	-0.2642	0.0250	7.8	0.8
	ω_X	-0.2224	0.0633		
NA	ω_Y	0.1293	0.0795		
	ω_Z	-0.6249	0.0381	7.5	0.5
	ω_X	-0.0763	0.0132		
AN	ω_Y	-0.0766	0.0172		
	ω_Z	0.1719	0.0336	2.3	0.4
	ω_X	-0.2463	0.0619		
Net rot	ω_Y	0.3117	0.0701		
	ω_Z	-0.5990	0.0127	8.0	0.4
σ_0			2.33		
WRMSE			2.25		

Table 3.4 c: Solution S20, plate angular velocity components, rms and max. tangential velocities

PLATE		ω °/Myr	rms °/Myr	V_{tmax} cm/yr	rms cm/yr
	ω_X	-0.5905	0.1117		
PA	ω_Y	0.7392	0.1235		
	ω_Z	-1.6153	0.0001	20.8	0.7
	ω_X	-0.5821	0.1107		
NZ	ω_Y	0.0066	0.1314		
	ω_Z	-0.5557	0.0219	8.9	0.9
	ω_X	-0.5529	0.1105		
SA	ω_Y	0.3618	0.1244		
	ω_Z	-1.0588	0.0180	13.9	0.7
	ω_X	-0.4796	0.1100		
AF	ω_Y	0.2943	0.1232		
	ω_Z	-0.8178	0.0172	11.0	0.7
	ω_X	-0.0975	0.1236		
AR	ω_Y	0.5407	0.1282		
	ω_Z	-0.5415	0.0540	8.6	1.0
	ω_X	-0.5622	0.1104		
EU	ω_Y	0.2970	0.1242		
	ω_Z	-0.8021	0.0220	11.4	0.8
	ω_X	-0.1477	0.1268		
IN	ω_Y	0.5623	0.3166		
	ω_Z	-0.6191	0.0783	9.4	1.7
	ω_X	-0.0801	0.1138		
AU	ω_Y	0.7707	0.1275		
	ω_Z	-0.6680	0.0234	11.4	1.1
	ω_X	-0.4608	0.1104		
NA	ω_Y	0.2736	0.1280		
	ω_Z	-1.0287	0.0358	12.9	0.7
	ω_X	-0.0763	0.0124		
AN	ω_Y	-0.0766	0.0162		
	ω_Z	0.1719	0.0316	2.3	0.4
	ω_X	-0.4847	0.1097		
Net rot	ω_Y	0.4561	0.1231		
	ω_Z	-1.0028	0.0119	13.4	0.7
σ_0			2.18		
WRMSE			1.95		

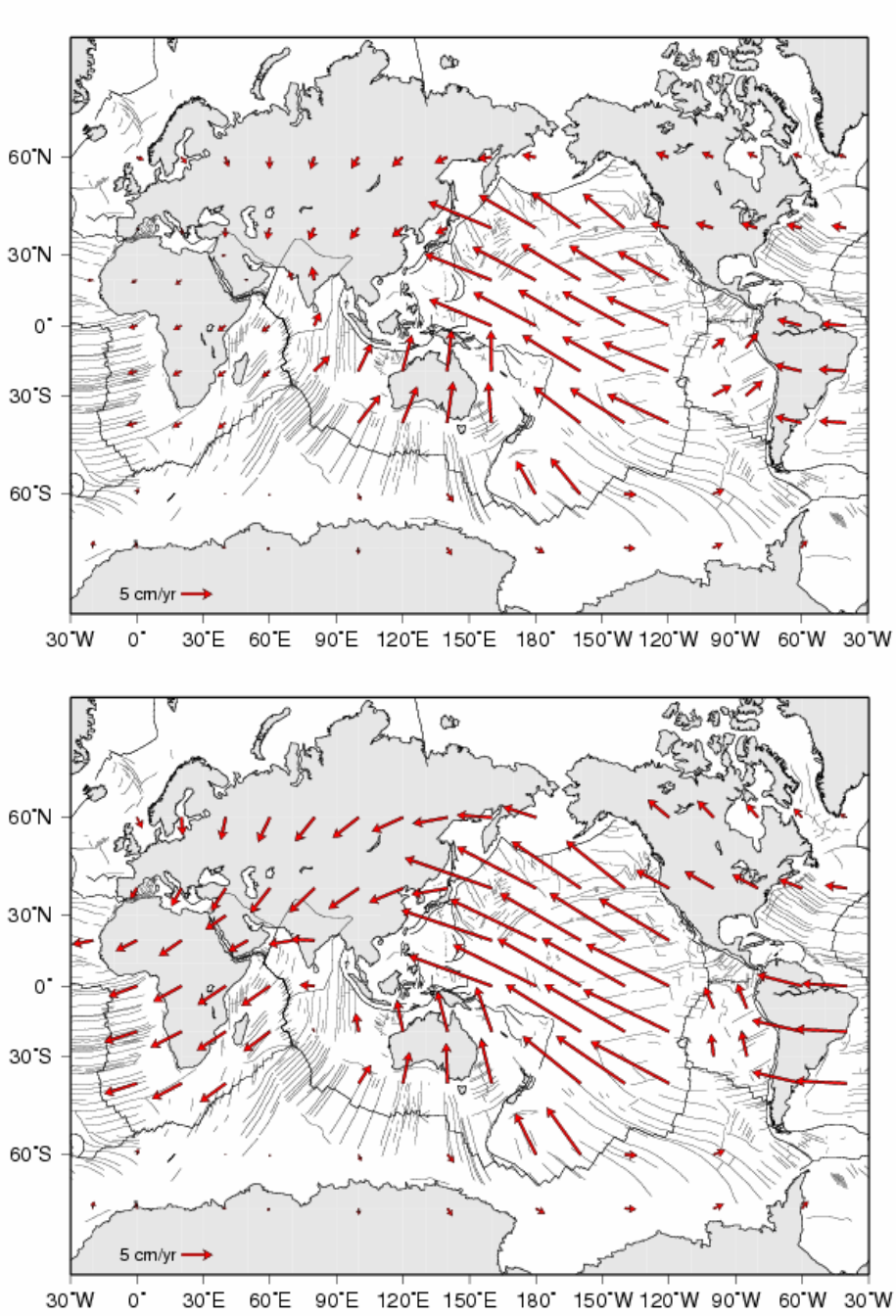

Figure 3.6 a, b: Plate motions with respect to mantle flow (Table 3.4 a, b and 3.5): a) GGS, lithosphere net rotation of 4.1 cm/yr and maximum PA tangential velocity of 11.6 cm/yr; b) S15, lithosphere net rotation of 8.0 cm/yr and maximum PA tangential velocity of 15.5 cm/yr;

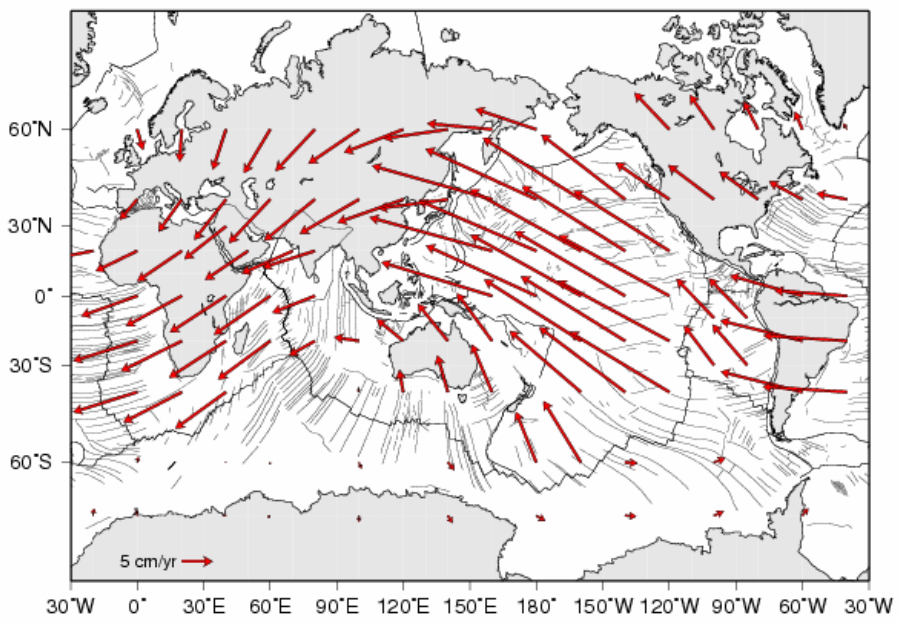

Figure 3.6 c: Plate motions with respect to mantle flow (Table 3.4 c and 3.5): c) S20, lithosphere net rotation of 13.4 cm/yr maximum PA tangential velocity of 20.8 cm/yr.

In this sense, the hypothesis of the ordered lithospheric flow, according to which all plates move westward (Figure 3.6 b, c), results to match better with the geological constraints, well agreeing with higher velocities and shallower asthenospheric source for the Hawaii and Society hotspot sources.

On the other hand, it is evident that at the boundaries of India and Nazca plates the continuity condition of the Eulerian equations fails, suggesting both these plates may experience significant sub-rotations here not considered and to reconsider the reliability of their ITRF00 sites included in our analysis (Heflin et al., 2005). In this respect, two of the three Indian sites (BAN2 and IISC) are quite close (about 5 km apart) so that they act as a unique site; therefore both India and Nazca plate kinematics are geodetically constrained by a minimum number of sites; moreover, doubts about the ITRF00 velocity of EISL (Eastern Island, Nazca plate) have been recently proposed (Kendrick et al., 2003).

Table 3.5: Plate poles and rotation rates

PLATE	GGS			S15			S20		
	Lat (°)	Lon (°)	Ω °/Myr	Lat (°)	Lon (°)	Ω °/Myr	Lat (°)	Lon (°)	Ω °/Myr
PA	-60.2	113.1	1.0442	-60.3	120.7	1.3950	-59.6	128.6	1.8720
NZ	27.2	-128.1	0.3406	-22.4	-160.5	0.3886	-43.7	179.4	0.8047
SA	-61.5	148.0	0.3994	-59.7	145.3	0.7584	-58.0	146.8	1.2481
AF	-51.2	155.5	0.1412	-55.4	148.2	0.5024	-55.5	148.5	0.9928
AR	-20.4	43.2	0.0662	-33.0	80.6	0.3768	-44.6	100.2	0.7714
EU	-28.5	168.2	0.1985	-48.0	154.7	0.5354	-51.6	152.2	1.0236
IN	12.9	51.0	0.3972	-26.7	77.8	0.4789	-46.8	104.7	0.8493
AU	3.8	58.6	0.5982	-22.2	75.8	0.6980	-40.8	95.9	1.0231
NA	-77.6	169.9	0.3286	-67.6	149.8	0.6757	-62.5	149.3	1.1600
AN	57.8	-134.9	0.2031	57.8	-134.9	0.2031	57.8	-134.9	0.2031
Net rot	-53.8	115.7	0.3658	-56.4	128.3	0.7188	-56.4	136.7	1.2036

In order to define analytically the global lithospheric flow both according to the *tectonic mainstream* definition of equation 1 (section 3.4) and on the basis of the our solutions, the coordinates of the continuity condition points at plate boundaries were estimated as weighted mean of their values on both sides (squared areas ratio $\left(\frac{A_p}{A_{PA}}\right)^2$ used as weights, Schettino (1999)) together their precisions.

Then, we preliminary estimated by least squares inversion the 7 parameters (the Fourier's coefficients) to assess their significance; finally, we estimated again only the significant parameters with their precisions, in order to define the 1 sigma latitude confidence interval of the *tectonic mainstream* for each solution (Figure 3.7 a, b).

The mean precisions are 7.3° and 6.8° for GGS and S15/S20 respectively, corresponding to about 750-800 km of uncertainty in latitude (Table 3.6).

Table 3.6: Fourier coefficients and *tectonic mainstream* latitude precisions (1 sigma confidence level)

	GGS	rms	S15	rms	S20	rms
a_0	0.000	0.000	0.000	0.000	0.000	0.000
a_1	-0.606	0.122	-0.508	0.122	-0.506	0.122
b_1	0.316	0.114	0.353	0.114	0.360	0.114
a_2	0.000	0.000	0.000	0.000	0.000	0.000
b_2	-0.254	0.071	0.000	0.000	0.000	0.000
a_3	0.000	0.000	0.000	0.000	0.000	0.000
b_3	0.000	0.000	0.000	0.000	0.000	0.000
Mean	(°)	rms	(°)	rms	(°)	rms
precision	7.3	0.5	6.8	0.2	6.8	0.2

Consequently, the best *tectonic mainstream* representation is band shaped; within this area the largest tangential motions occur (Figure 3.7 a, b). Moreover, about the Fourier's coefficients, it is worthwhile to note that:

- all the solutions show that a_0 is not significant (Table 3.6), so that mean latitude of the *tectonic mainstream* is zero,
- for GGS the significant parameters are a_1, b_1, b_2, whilst for S15 and S20 the only significant parameters are a_1, b_1 (latitude is simply a first order sinusoid w.r.t. longitude) and the *tectonic mainstreams* are just equal (Table 3.6)
- for S15 and S20 the net-rotation equators lie inside the corresponding *tectonic mainstream* band, defined by the 1 sigma latitude confidence intervals (Figure 3.9)

3.7 Conclusive remarks

The main purpose of this chapter has been to introduce the concept of *tectonic mainstream* on the basis of geological evidences and to prove its consistency by space geodesy data, in order to propose a new unified way to describe plate motions with respect to the underlying mantle. A parametric

function in the form of a 3rd order Fourier series ha been hypothesized for the *tectonic mainstream*.

The main result is a model allowing the estimation of plate kinematics on the basis of both velocities from space geodesy and geological evidences used as constraints. This model was applied by using velocities of 28 ITRF2000 sites suitably selected in stable intraplate areas leading to 3 possible solutions under different hypotheses about the Pacific hotspot source depths. The shallower the asthenospheric source, the faster results the velocity of the Pacific plate. For each solution, the significant parameters of the *tectonic mainstream* truncated Fourier series are estimated together their 1 sigma confidence interval. All the 3 reconstructions are confirming i) the tectonic mainstream and ii) the net rotation of the lithosphere. In the GGS case, the westward drift is only an average rotation, i.e., some plates (Nazca, Cocos, Juan de Fuca) still move eastward relative to the mantle. Assuming faster Pacific motions as the asthenospheric source of the hotspots would allow, the net rotation increases to a complete polarization in the remaining 2 solutions (S15 and S20), which match remarkably better with the geological constraints (Table 3.4). Moreover, for S15 and S20 the analytical expressions of the *tectonic mainstreams* are remarkably simpler than that hypothesized, just reducing to a first order sinusoid in longitude, quite close to the corresponding net rotation equators.

The shear wave splitting technique (e.g., Savage, 1999) is an independent tool for detecting the seismic anisotropy in the asthenosphere, which is considered the preferential orientation of olivine crystals in a sheared flowing mantle (Silver and Holt, 2002). The direction of the anisotropy between lithosphere and underlying mantle (e.g., Fisher et al., 1998; Montagner, 2002) aligns quite consistently with the absolute plate motions reconstructions, apart along subduction zones or other mantle anomalies.

Nevertheless, since solutions with faster and faster Pacific plate does not differ significantly as regards the agreement between space geodesy solution and geological constraints, it is not possible to assess an upper limit for the Pacific plate velocity and for the derived plates kinematic on their basis, and additional hypotheses should be introduced.

In this respect, even if the occurrence of a westerly polarized lithosphere motion cannot be considered at present a controversial phenomenon (Ricard et al., 1991; Gripp and Gordon, 2002 and reference therein, this paper), we feel that its origin is not yet completely clear, because it may be due to different combined effects hard to separate.

As previously noted, a mean lithospheric rotation rather than a global phenomenon has been so far preferred (e.g., Ricard et al. 1991) because it preserves the angular momentum of the Earth without rapidly decelerating its rotation speed. However, it has recently been shown that a global lithospheric rotation is physically feasible, although at variable velocities among the different plates (Scoppola et al., 2006). According to this model, plate tectonics would occur with the combination of a rotating planet under tidal torque, efficient internal convection, and lateral viscosity variations at the lithosphere-mantle interface where are supposed to occur thin hydrate layers with very low viscosity. The viscosity of the upper asthenosphere is still unknown, but the effective viscosity should be about 1000 times lower when measured for a horizontal shear with respect to vertical loading as simulated in classical post-glacial rebound studies (e.g., Scoppola et al., 2006). Moreover, new petrological and geophysical evidences are emerging of a very low viscosity between 100-150 km at the lithosphere base, in the low velocity zone (LVZ) representing the upper asthenosphere (e.g., Panza, 1980; Hirth and Kohlstedt, 1996; Holtzman et al., 2003; Rychert et al., 2005; Thybo, 2006; Aoudia et al., 2007; Melini et al., 2008). This layer is usually neglected and considered as a whole with the underlying higher viscosity lower asthenosphere.

Although we do not want to force the reader to accept the faster kinematic models (S15 and S20), which may be refined in further investigations, we underline that a global net rotation is more coherent with the geological and geophysical asymmetries which support more a complete rotation of the lithosphere rather than only a mean rotation.

About the tidal role, evidence is that the latitude range of the estimated tectonic *mainstream* is about the same of the Moon maximum declination range (± 28°) during the nutation period (≈18.6 years). Further indications come from the fact that the induced geopotential variations and the solid Earth tide modeling (McCarthy and Petit, 2004) generate maximum amplitudes of the Earth bulges (≈ 30 cm) propagating progressively within the same latitude range (Biagi et al., 2005). In particular, the track of the semi-diurnal bulge crest is about directed from E to W, as small circles moving from latitudes 28° to 18°, when the Moon moves from maximum to minimum declinations (the same happens at negative latitudes for the opposite bulge), thus suggesting a role of rotational and tidal drag effects (Bostrom, 2001).

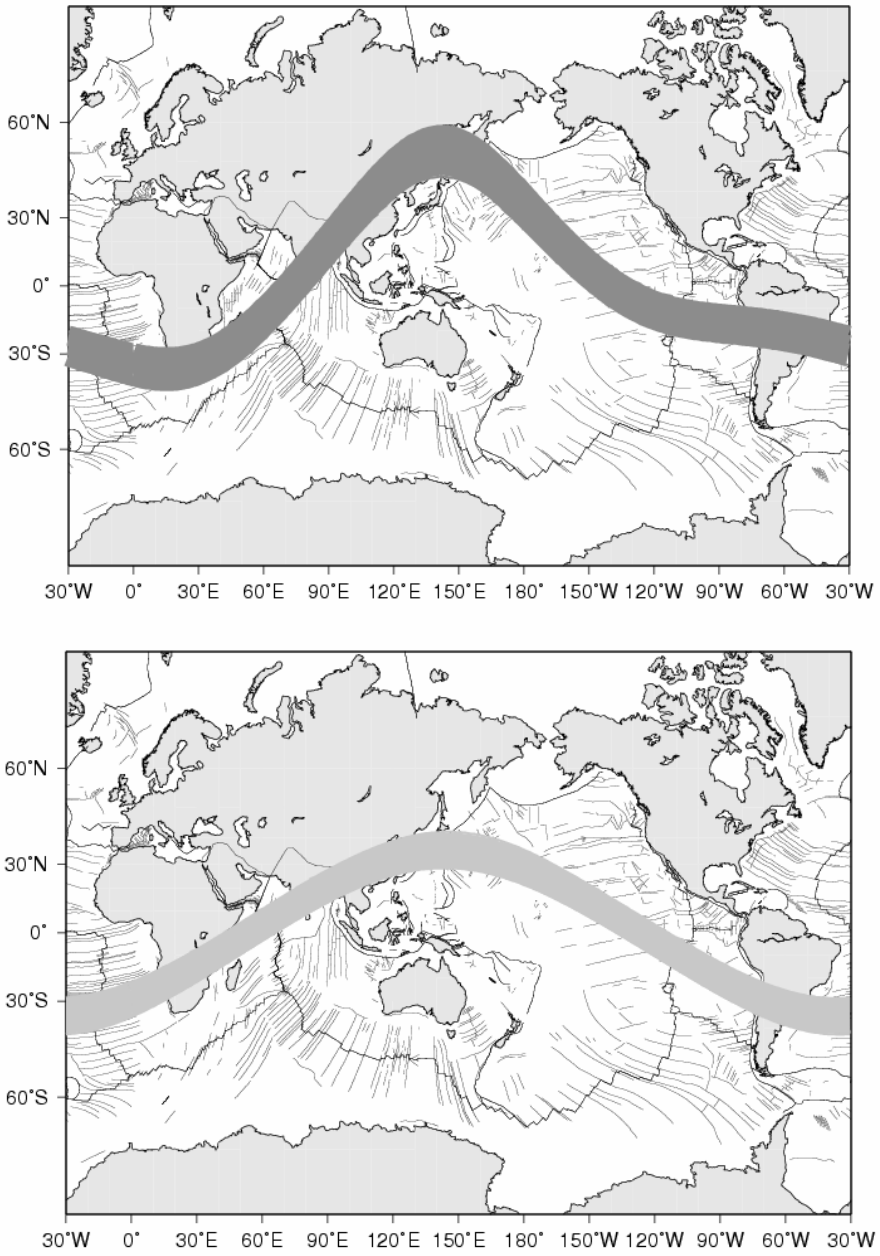

Figure 3.7: *Tectonic mainstream* representations (Table 3.6): a) dark grey, latitude confidence interval of ± 7.3° for GGS, b) light grey, latitude confidence interval of 6.8° obtained for S20 (PA maximum tangential velocity of 20.8 cm/yr and net lithospheric rotation of 13.4 cm/yr at 1 sigma confidence level).

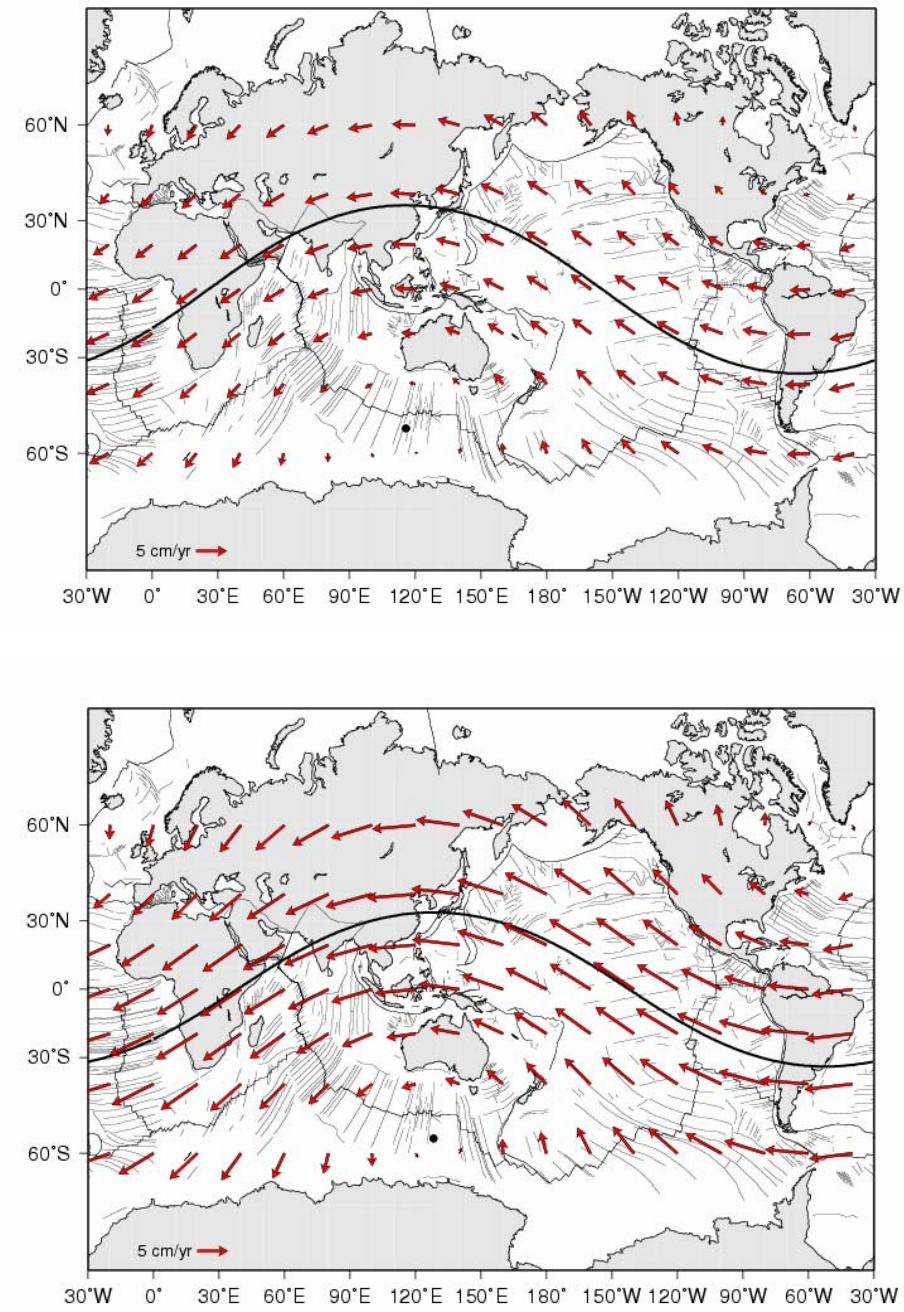

Figure 3.8 a, b: Global lithospheric net rotation, tangential velocities and equators: a) GGS solution, maximum tangential velocity of 4.1 cm/yr; b) S15, maximum tangential velocity of 8.0cm/yr;

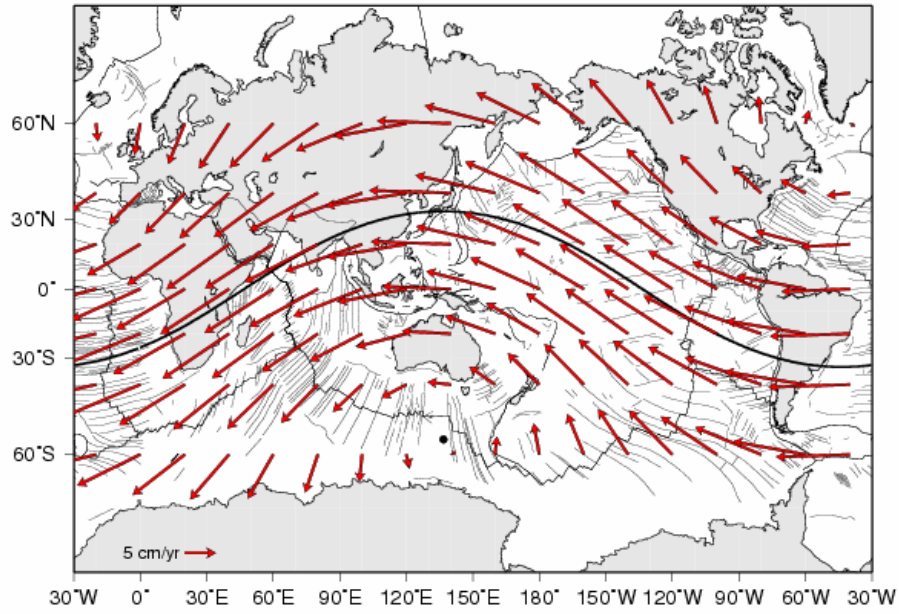

Figure 3.8 c: Global lithospheric net rotation, tangential velocities and equators: c) S20, maximum tangential velocity of 13.4 cm/yr.

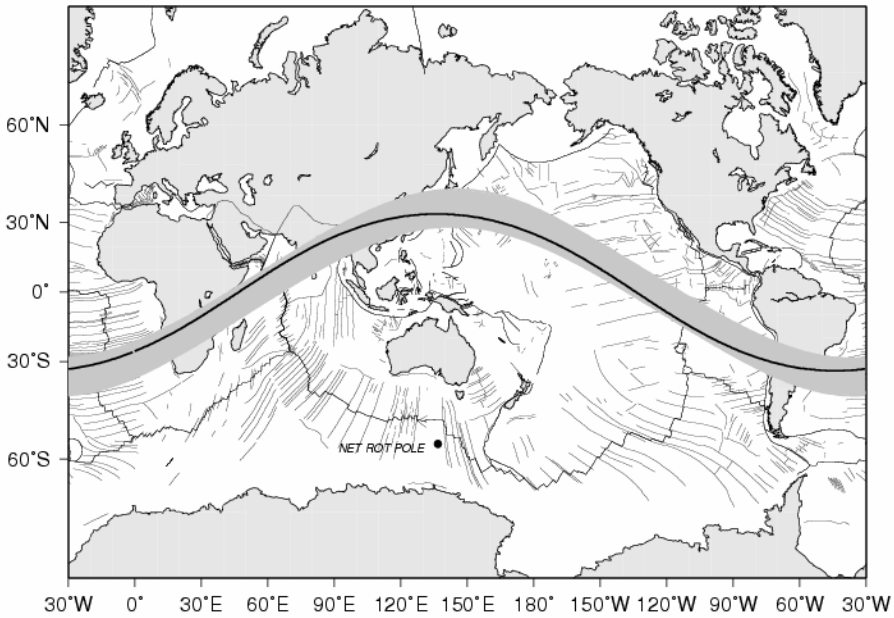

Figure 3.9: The net rotation equator lies within the *tectonic mainstream* latitude band, example relative to S20 solution.

4 Regional kinematic model

4.1 Introduction

In the general paradigm of plate tectonics, along a subduction zone the lower plate converges relative to the upper plate and penetrates the mantle. However, relative to a fixed point in the upper plate U, the lower plate L can converge, diverge or be stationary, and the subduction can be still active. As in a fold, the subduction hinge defines the section with the maximum curvature of the lithosphere. The subduction hinge is the area where the foreland lithosphere bends, entering subduction, The area is the curvature between the undeformed foreland and the slab. It may be several tens of km wide and is a migrating hinge, cross-cutting new sections of the foreland subducting lower plate. Therefore, relative to the lower plate, the subduction hinge always migrates towards it. Vice versa, relative to the upper plate, the subduction hinge can migrate away or towards it. Ideally, we can project the intersection of the deep location of the subduction hinge on the horizontal plane, and to infer its horizontal motion by means of geological (long term speed) and space geodesy data (present day). The transient subduction hinge H can converge, diverge, or be stationary, and the subduction rate V_S is given by the velocity of the hinge H minus the velocity of the lower plate L, i.e., $V_S=V_H-V_L$ (Doglioni et al., 2006). Therefore the subduction rate is not equal to the convergence rate, which can be either positive or negative, and the subduction can occur even if the lower plate diverges or is stationary relative to the upper plate in case the subduction hinge migrates away from the upper plate faster than the lower plate. We show here that the combination of lower plate and subduction hinge velocities relative to the assumed fixed upper plate can provide different kinematics even along a single subduction zone. The Apennines belt and related Tyrrhenian back-arc basin (Figure 4.1) are taken as an example of subduction zone where these parameters vary along strike. Using a dense GPS network widespread along the study area (Figure 4.2), we have analyzed and interpreted the different kinematics, comparing the results with geological studies. This chapter presents the

current GPS velocity field in the Italian area obtained combining three different permanent GPS network solutions.

It will be shown that at least four different regimes can occur along the Apennines belt, since the subduction rate depends both on the convergence or divergence rate and the velocity of the subduction hinge that can either converge or diverge relative to the upper plate, decreasing or increasing the speed of the subduction respectively. Along some segments, the subduction occurs even in spite of a lower plate diverging from the upper plate. The motion of the Apennines and the Adriatic deformed margins is also expressed in the deep and shallow HSRF.

4.2 Geodynamic setting: the Adriatic microplate and the Apennines subduction

The Apennines-Tyrrhenian system formed as accretionary prism (Bally et al., 1986) and back-arc basin respectively in the hangingwall of the Neogene to present arcuate W-directed subduction of the Adriatic continental and Ionian oceanic lithospheres (e.g. Doglioni et al., 1999; Panza et al., 2003; Faccenna et al., 2004). Moving along strike, the slab had and still has different behaviors, both in terms of seismicity (Pondrelli et al., 2004), surface geology and kinematics, due to the relevant anisotropies in thickness and composition of the downgoing lithosphere (Calcagnile and Panza, 1981; Carminati et al., 2005). The lower plate of the Apennines-Maghrebides subduction system is in fact composed of different types of lithosphere, inheriting pre-existing Mesozoic, Cenozoic and even active rifting episodes. An active rifting occurs in the Sicily channel (e.g. Corti et al., 2006), separating the Sicilian continental lithosphere from the main Africa plate (Figure 4.1). Moving E-ward, the Malta escarpment is a right-lateral active transtensional system (Doglioni et al., 2001) re-using a pre-existing Mesozoic continent-ocean transition between Sicily and the Ionian deep basin (Catalano et al., 2001). The transition between the Ionian and the Adriatic continental lithosphere is the conjugate margin of the Malta escarpment. This margin should likely be considered active since plate kinematic models predict independent and different velocities of the Adriatic plate (e.g. Battaglia et al., 2004). The deformed margins of the Mesozoic Adriatic plate are inferred in Figure 4.1. They are chiefly made of passive continental margin sequences shortened by the Apenninic, Alpine and Dinaric subduction zones-related orogens.

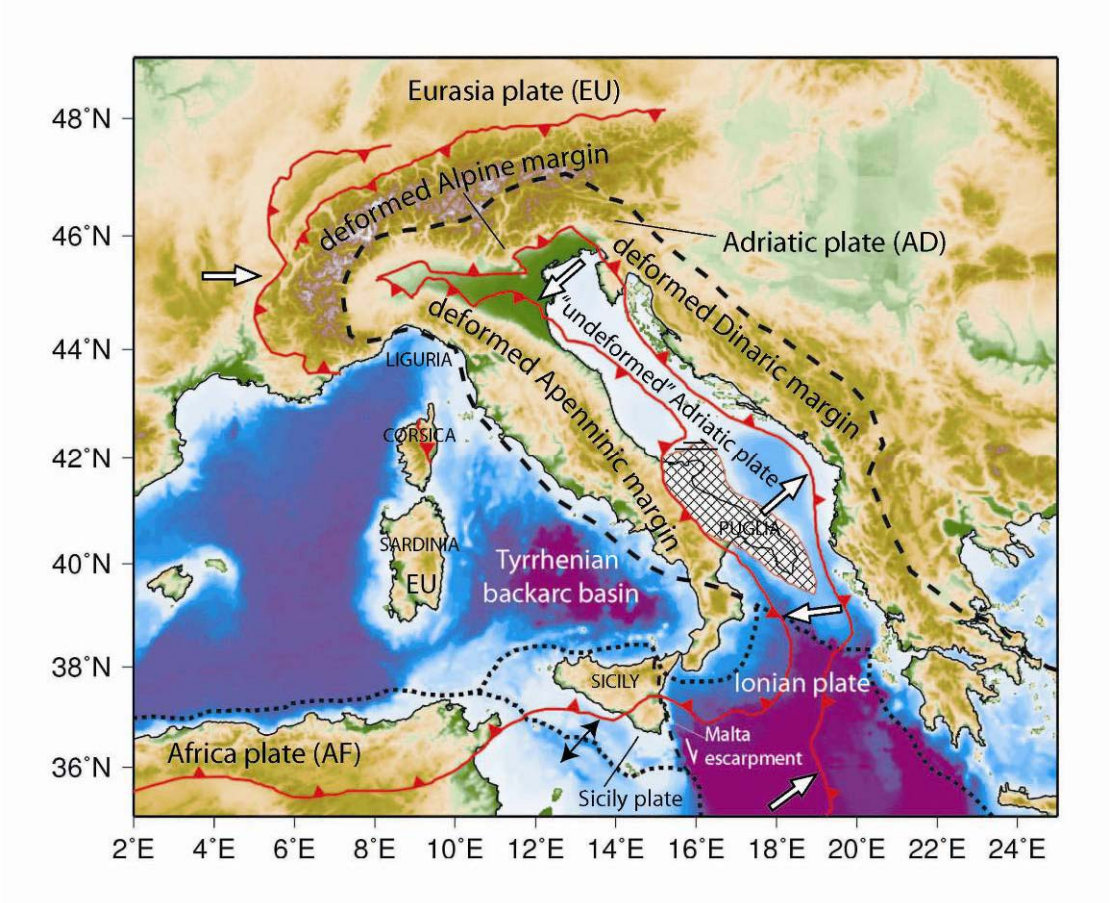

Figure 4.1: A) Along the Apennines subduction, the footwall is composed by four plates, the Adriatic, Ionian, Sicilian and African lithospheres. The Adriatic microplate subducts underneath the Apennines and the Dinarides, whereas it overrides the European plate along the Alps. The Adriatic "undeformed" part is restricted in the central-northern part of the Adriatic Sea. Part of it is uplifted by a lithospheric buckling in the Puglia region (squared area), and the remaining part is mostly tilted by the Apennines foreland monocline, associated to the subduction hinge. The black dashed line limiting the border of the continental part of the Adriatic microplate is inferred after some retrodeforming of its margins. A large part of the Adriatic original lithosphere has disappeared along the subduction zones bordering the plate. The Ionian (partly oceanic) lithosphere retreats right laterally with respect to the continental lithosphere of Sicily, which is in turn moving NE with respect to Africa, generating the rift in the Sicily channel.

In the Alps the Adriatic plate overrode the Eurasia plate, whereas along the Apennines and Dinarides, the Adriatic lithosphere represents the footwall plate. Most of the Adriatic original lithosphere has disappeared along the Apennines and Dinarides subduction zones, possibly with oceanic crust at

the leading edge. The Ionian (partly oceanic) lithosphere has a differential right-lateral retreat with respect to Sicily continental lithosphere. The latter is spreading apart with respect to Africa, generating the Sicily channel rift (Figure 4.1). The Adriatic plate underwent rifting episodes throughout the Mesozoic and became separated from the Africa plate with the opening of the Ionian basin, which age and nature are still matter of debate (Catalano et al., 2001). Since the Cretaceous, the Alpine subduction developed carrying the northern and western margins of the Adriatic plate over the Eurasia plate.

Contemporaneously, the Adriatic plate subducted Eurasia toward NE-ward along the Dinarides. Since Oligocene times, the Adriatic plate inverted its behavior along its western margin, and switched from being the upper plate of the Alpine subduction, to the lower plate during the Apennines subduction (Doglioni et al., 1998). However within the Adriatic plate, different kinematic behaviors can be distinguished. For example, the Puglia foreland is uplifting (Doglioni et al., 1994), whereas the central-northern Adriatic Sea is subsiding as the Po Basin to the N (Doglioni, 1994). Practically all the Adriatic plate is subject to ongoing deformation; in fact the area unaffected by horizontal deformation (compression, strike-slip, rifting) is undergoing either tilting and subsidence (the whole Adriatic Sea and Po Basin) or uplift (Puglia). The different vertical behaviors can be ascribed to the Apennines slab retreat (subsidence) or lithospheric buckling (uplift).

Therefore no GPS sites can be considered completely untouched by active deformation within the Adriatic plate (Figure 4.2).

4.3 Velocity field of the Italian area

The complete GPS network solution arises from the combination of three main sub-networks (Figure 4.2): the Italian network, composed of 102 permanent sites, 91 located in Italy and other 11 in the surrounding countries; the Austrian Reference Extended (ARE) network (Pany et al., 2001) and the REGAL network (Calais et al., 2000).

We implement a rigorous combination strategy based on the complete covariance matrices and a convenient handling of constraints, as described in Davies and Blewitt (2000). The combination of independent solutions provides a valuable means to compare coordinate and velocity solutions at common sites, and to minimize the systematic errors associated with each individual processing strategy (e.g. Nocquet and Calais, 2004).

4.3.1 Italian area network

At present the permanent GPS sites installed in the Italian area together with the historical late-nineties permanent sites constitute a dense network covering the whole country with a mean inter-site distance of about 60 km.

A total of 102 sites were considered including a few located in the surrounding area. The network is formed by stations owned by different agencies and authorities, primarily by the INGV Integrated National GPS Network (RING, Selvaggi et al., 2006), the Italian GPS Fiducial Network of the Italian Space Agency (IGFN ASI, Vespe et al. 2000), the European EUREF network (Bruyninx, 2004), and minor clusters owned by regional authorities and universities. We selected a limited time span, from DOY 1/2003 to DOY 54/2007 because most of the GPS sites were installed in the last few years. The velocity uncertainties of each site have been evaluated in detail using the error analysis technique developed by Williams (2003).

We processed the GPS phase data in six regional clusters, each containing at least 11 common anchor sites, i.e. selected sites based on station performance and geographical distribution, used as core sites for the reference frame definition and the cluster combination.

We have analyzed the daily RINEX files with the Bernese Processing Engine v.5.0 (Beutler et al., 2007) applying the quasi-ionosphere-free (QIF) strategy for the ambiguity resolution and constraining each daily solution to the coordinates of MATE (Matera) to 0.01 mm (apriori sigma). Subsequently, each solution has been unconstrained (Davies et al. 2000) removing the apriori constraints and adding loose translation and scale constraints, then the loosely constrained cluster solutions of each day have been merged into daily loosely constrained solutions (Bianco et al., 2003).

In order to express the velocity field in a coherent reference frame, we adopt the official ITRF2005 (International Terrestrial Reference Frame), recently released by the International Earth Rotation and Reference Systems Service (Altamimi et al., 2007). The daily combined network solutions were rigidly transformed into the ITRF2005 frame estimating translations and scale parameters. There are 13 core sites contributing to the rigid transformation and globally the weighted RMS of the residuals after the transformation is about 2-3 mm. The official ITRF2005 solution contains embedded offsets for each site data history, i.e. different sets of coordinates and velocities are provided for different time spans; nevertheless we choose a set of fiducial sites whose velocities are at any time constant over the entire period.

4.3.2 ARE network

The daily solutions of various GPS networks in the Eastern Europe area are available at the Observatory Lustbuehel (OLG, Graz). We considered the Austrian Reference Extended solutions (ARE) that contain some Austrian reference sites and also the permanent sites from the Central European Geodynamic Research Project (CERGOP). The daily solutions are available in SINEX (Solution INdependent EXchange) format containing coordinate estimates and covariance matrices. They were obtained with different versions of the processing software and with sporadic changes in the analysis procedures through the years. The time interval considered in our analysis span from DOY 221/1998 until DOY 365/2006. We recognize differences in the daily solutions, the majority of them (unitl DOY 287/2006) tightly constrained to a single site (0.01 mm apriori sigma), the remaining solutions loosely constrained (about 4 m apriori sigma). To properly set the reference frame, all the daily solutions were unconstrained, removing the apriori covariance, adding minimal constraints and subsequently rigidly transformed into the ITRF2005 reference solution. Due to the limited extension of the network a simple translation and scale Helmert transformation was applied. A maximum number of 23 anchor sites contribute to the Helmert transformation through the time series, but occasionally outliers were isolated and edited from the transformation itself, thus on the average, 10-13 sites did actually contribute. For the anchor sites, the global weighted RMS of the coordinate residuals after the transformation was only slightly higher (3-4 mm) than for the Italian network.

4.3.3 The REGAL network

We used the available velocity solution of the permanent GPS network on the western Alps (Calais et al., 2000). The solution file contains loosely constrained site velocity and coordinates obtained from daily coordinate solutions (from DOY 001/1996 to DOY 200/2003) processed by Nocquet and Calais (2004) with the GAMIT-GLOBK software (King and Bock, 2002; Herring et al., 1990). The overall network consists of 58 sites, 27 of them being strictly REGAL sites whereas the others are spread all over the Western Europe. The apriori constraints are 10 m for the coordinates and 1 m/yr for the velocities.

Since the daily solutions were not available, the coordinate/velocity solution has been aligned to the ITRF2005 reference frame through a 14 parameter Helmert transformation after applying the corresponding 14 inner constraints to the covariance matrix. Seven anchor sites contribute to the

transformation yielding a global weighted RMS of residuals of a few mm in the coordinates and a few tenths of mm/yr in the velocities.

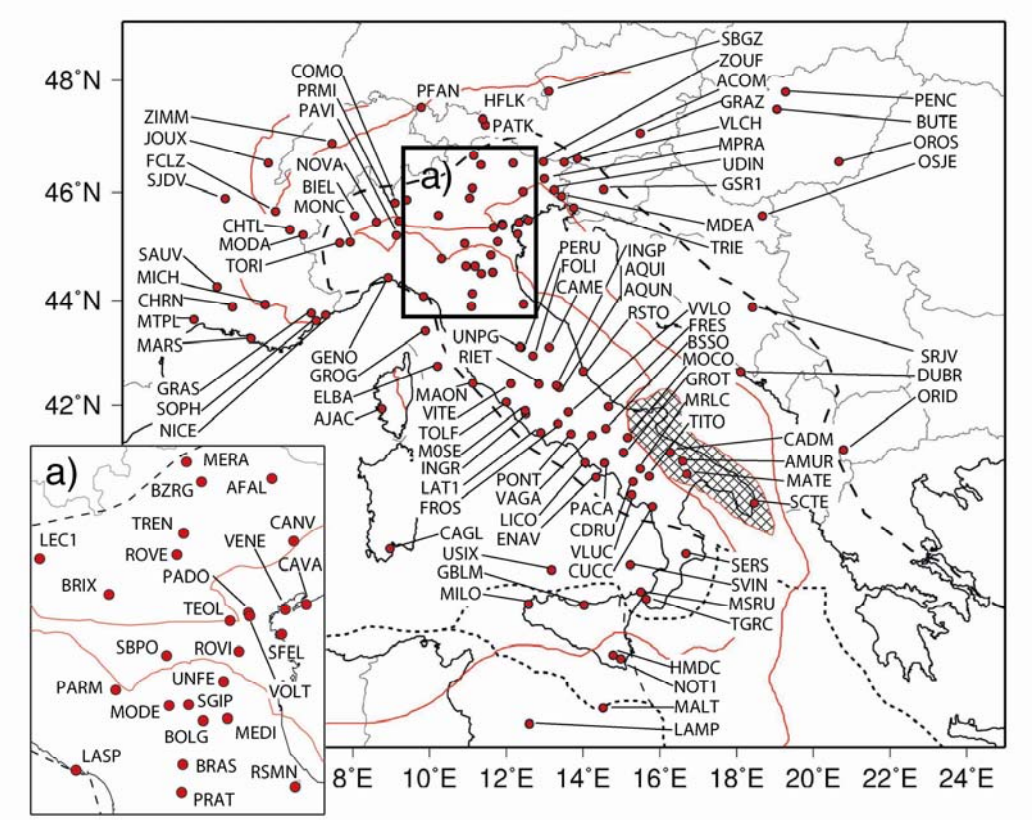

Figure 4.2: Acronyms and red spots indicate GPS stations used in this study. Very few sites are located outside the deformational area. Moreover those few sites are located in the subsiding foreland area. Therefore there are no good kinematic constraints on the Adriatic microplate.

4.3.4 Time series analysis

Since the two available time series (Italian and ARE networks) differ substantially in terms of repeatability and spectral content, we prefer to estimate the velocity fields separately and to combine the two velocity fields thereafter.

Thus all the daily solutions were stacked separately into normal equation matrices and site positions and velocities were estimated simultaneously along with annual signals and sporadic offsets at epochs of instrumental changes. The estimated parameters will depend on the whole covariance matrices and we note that the covariances between sites are effective in

tightening up weakly constrained velocities, e.g. when the time series is very short or badly conditioned. As a result we could observe a rather good spatial coherence in the velocity field also for those sites that nominally should suffer from high systematic errors due to their short observation period. In a few sites we judge the horizontal velocities acceptable even if derived from time series as short as 1.5 years. Concerning the vertical motion, since the intrinsic repeatability of the vertical component is a factor of 2-4 worse than the horizontal component, we found that the four-year period is not sufficient for a reliable estimation and most vertical movements do not exceed the noise.

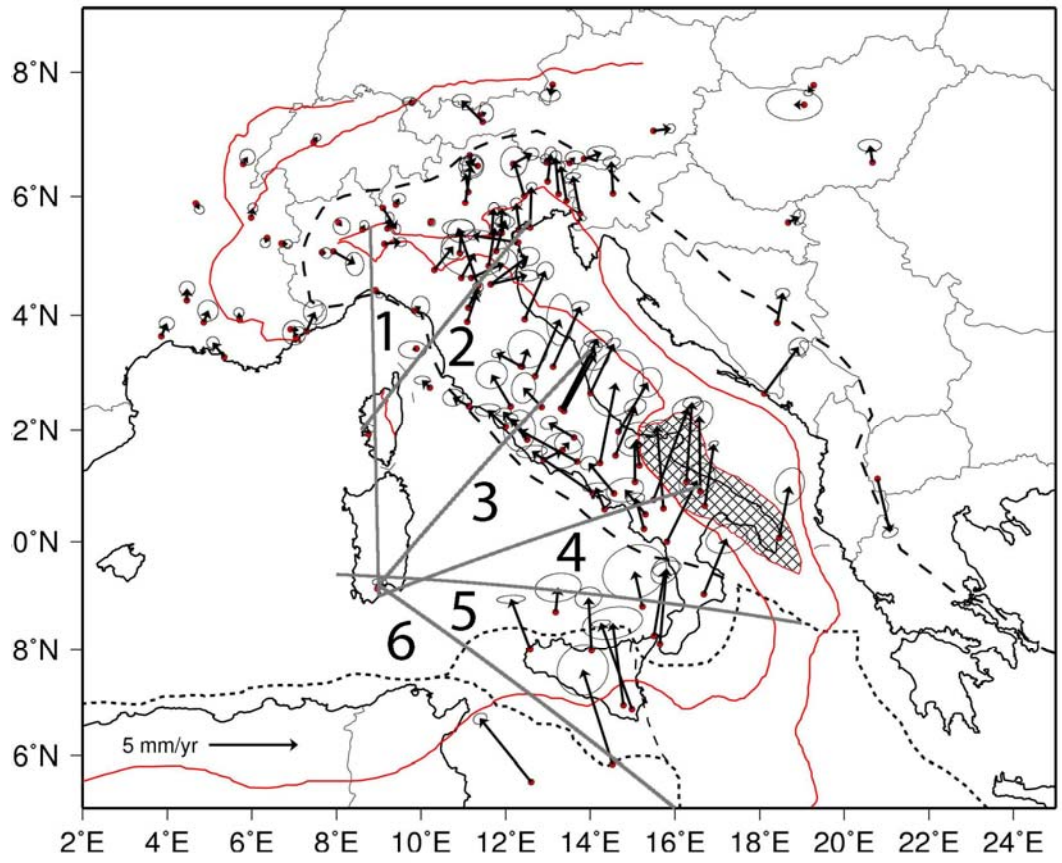

Figure 4.3: GPS velocities with respect to Eurasia and rescaled ellipses at 68% probability level. Confidence ellipses include the variance of the rotation vector defining the reference frame estimated in ITRF2005. Grey lines are the sections (1-6) along which velocities and uncertainties at 68% probability level are projected (Figure 4.9). Note the relevant change in direction between the sites located in the western central and southern Apennines with respect to the eastern side, providing evidence for a major tectonic change and transtensional rift along that boundary.

The whole velocity field of the Italian area is shown in Figure 4.3 with respect to the Eurasian reference frame, the ellipses being the 2 degrees of freedom, 68% confidence region. The velocity components and errors of each site are reported in Tables 4.1, 4.2 and 4.3 at the end of the Chapter 4.

4.3.5 Error analysis

The formal standard deviations associated with the velocity estimates are known to be underestimated, depending on the deviation from normality of the detrended residuals. For independent randomly distributed residuals, the formal error decreases as $1/\sqrt{n}$ where n is the number of daily solutions. A number of studies have demonstrated that the GPS time series show significant temporal correlations that must be taken into account to get reliable estimates of the velocity uncertainties (Williams et al., 2004; Mao et al., 1999; Johnson and Agnew, 1995, and references therein). In particular, the spectral content of geodetic time series is dominated by white noise at high frequencies and a rising power density at low frequencies.

We scaled the formal errors of the GPS rates using the approach developed in Williams (2003), accounting for a power-law noise and a constant white noise term estimated directly from the detrended residuals. We estimate three parameters (the spectral index κ, white noise and colored noise amplitudes) for each time series component after subtracting a linear trend and an annual sinusoid. The three-parameter model characterizes the noise content of each GPS site, allowing the spectral index to range continuously from a pure white noise (κ=0), through flicker noise (κ=-1) up to a random walk (κ=-2) noise. Thus, the estimates allow scaling the formal errors associated to each site velocity in proportion to the noise amplitudes and length of the time series. We obtained scale factors spread between the tenth and ninetieth percentiles of 3.2 and 9.7, with a median value of 5.7. Generally, the vertical rate component presents a slightly higher scale factor (median 6.5) than the planar component (median 5.2). In the east and north components the estimated spectral index ranges between κ=-0.2 and κ=-0.9 (average -0.60) with an average spectral amplitude of 1.2 mm/yr$^{-\kappa/4}$, thus being halfway between white noise and flicker noise. The Median Time $T_{1mm/yr}$ for the velocity uncertainty to reach 1 mm/yr, relevant for the detection of changes in velocity, is on average 0.5 yr, very close to other findings (Williams et al., 2004; Beavan, 2005).

To test the consistency of the scaled errors with the velocity repeatability, we have evaluated the mutual velocity differences at overlapping sites. A total of 30 independent site velocity differences can be formed and their

residuals could be useful to test the reference system realization. The overall WRMS of the velocity residuals are 0.4 and 3.6 mm/yr (horizontal and vertical) and the medians of the scaled uncertainty are 0.6 and 2.5 mm/yr (horizontal and vertical). The normalized χ^2 (per degree of freedom) is χ_v^2=1.62 which has to be compared with the higher value of χ_v^2=16.5, obtained without scaling the velocity errors. Since the systematic differences (rotation-translation and scaling of the velocity fields) are not statistically significant, we conclude that the scaled velocity errors are consistent with the velocity repeatability.

4.4 Africa-Eurasia convergence

We estimate the plate rigid motion directly from the official ITRF2005 velocity solution. The rigid plate motion is statistically inferred using a simple χ^2 test-statistics to select the coherent subset of sites defining a stable plate, as suggested in Nocquet et al. (2001). Starting from three central European sites (pilot triad: WSRT, WTZR and ZIMM) a total of 24 sites result assigned to a stable plate with χ_v^2=1.46. The absolute ITRF2005 Eurasia pole and rotation rate are 55.85°N, 95.72°W and 0.266 ± 0.003°/Myr, consistent with previous ITRF2000 and recent ITRF2005 poles (Fernandes et al., 2003; Kreemer et al., 2003; D'Agostino and Selvaggi, 2004; Serpelloni et al., 2005; Altamimi et al., 2007). A few central European sites, including POTS, BOR1, LAMA and JOZE, are surprisingly rejected both at 95% and 99% significance level. We argue that the associated errors are probably underestimated, i.e. too small if compared to their velocity residuals and should be recalibrated in successive ITRF realization. Furthermore all the Siberian sites are systematically rejected from being rigidly connected with the central Europe region. In particular, all the sites located east of ARTU (58°E) have a 2-3 mm/yr W-ward residual velocity pattern that cannot be accommodated by a variance rescaling.

The ITRF2005 Africa Euler pole is estimated using the same χ^2 test procedure, starting from a triad located west of the East African Rift (MAS1, GOUG and HRAO); the final selection is composed by 10 sites. The relatively high misfit (χ_v^2=4.76) suggests that the associated ITRF2005 variances could be underestimated by the same χ_v^2 factor, or the rigid plate model is inadequate for these sites. Scaling the ITRF2005 velocity variances by the same factor leads to a substantially equivalent Euler pole, accepting a total of 10 sites belonging to the African plate. Thus we conclude that the pole is

rather stable nevertheless the declared ITRF2005 variances are probably underestimated by the same factor. The estimated absolute pole and rotation rate are 49.40°N, 83.06°W and 0.268 ± 0.003°/Myr, consistent at 1-sigma level with the recent ITRF2005 value (Altamimi et al., 2007).

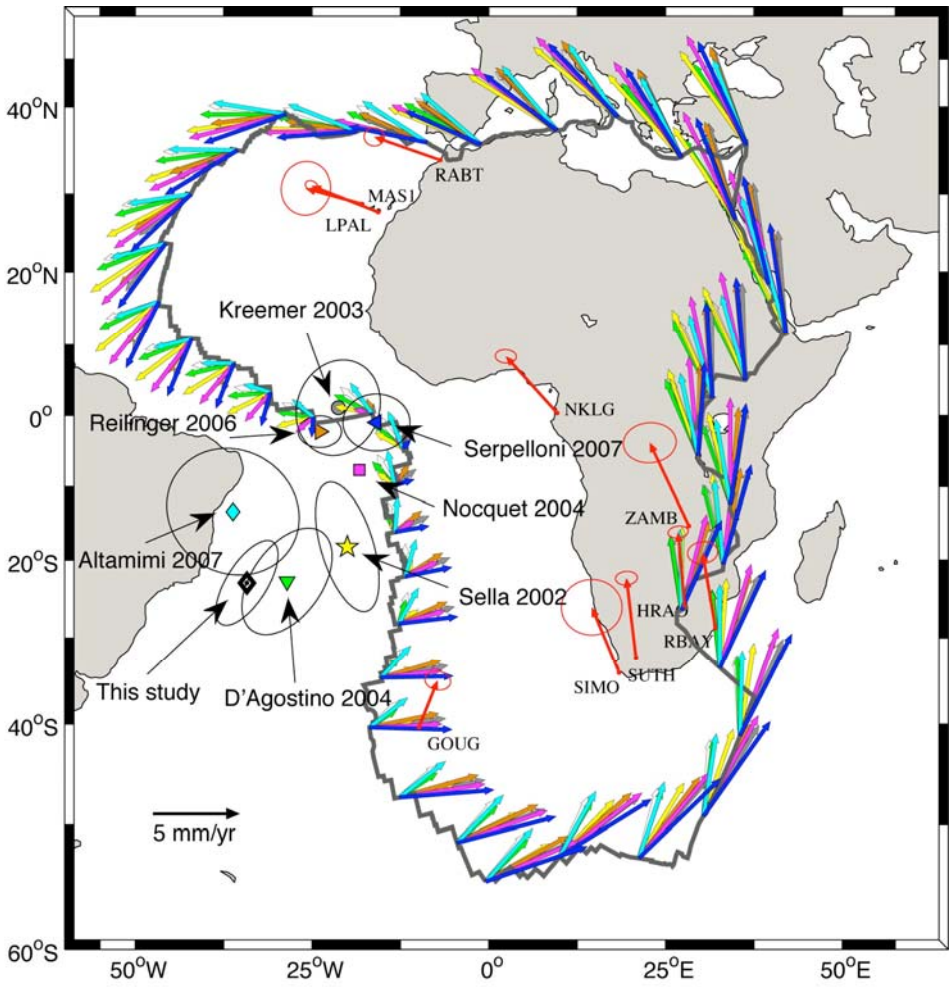

Figure 4.4: Different estimates of the African poles with respect to Eurasia: from this work, from Sella et al. (2002), Kreemer et al. (2003), D'Agostino and Selvaggi (2004), Nocquet and Calais (2004), Reilinger et al. (2006), Serpelloni et al. (2007) and Altamimi et al. (2007). The relative velocities along the African plate boundary are shown in different colors according to the corresponding rotation pole.

The estimated poles and uncertainties are reported in Table 4.4 and 4.5, the velocity residuals of the Eurasian and African sites are reported in Table 4.6, all at the end of this Chapter.

The relative Africa-Eurasia pole obtained in this work is in good agreement with the poles of Sella et al. (2002), D'Agostino and Selvaggi (2004) and Altamimi et al. (2007), and differ substantially from those published by Kreemer et al. (2003), Nocquet and Calais (2004), Serpelloni et al. (2007) and Reilinger et al. (2006), as shown in Figure 4.4. The map showing the different relative Euler poles exhibit surprisingly the same SE-NW convergence in the Mediterranean region, thus indicating that the convergence velocity in the Mediterranean region is relatively insensitive to the selection and time span of stations used to estimate the rotation vector. Differences arises as the plate motion is propagated along the African margin, again the most significant differences arise from the Kreemer et al. (2003), Reilinger et al. (2006) and Serpelloni et al. (2007) poles, that could probably be explained by the different realization of the absolute Africa plate motion reflecting the poorly geographic coverage of the African geodetic network.

4.5 The Adriatic microplate kinematics

The existence of an Adriatic microplate lying at the margin of Eurasian and African plates has been under discussion for years, considering both the assumption of an independent microplate (Ward, 1994), and proposing the Adriatic area as a promontory of the African plate (Channell, 1996). Global scale plate kinematic models, such as NUVEL1-A (DeMets et al., 1994), based on geological and geophysical data, or REVEL (Sella et al., 2002), based on recent space geodesy data, did not include the Adriatic plate motion, but they substantially presented different estimated velocities of the major plates (i.e. Eurasia and Africa) at this common boundary. The Adriatic microplate motion has been recently interpreted as the combination of two blocks (i.e., north Adriatic and south Adriatic) with independent kinematics (Battaglia et al., 2004) or as the relative motions of two blocks attached to the major plates (Oldow et al., 2002). These different interpretations arise from the fact that the Adriatic boundaries are not completely known and the Adriatic motion is only weakly constrained; in fact this microplate is generally not taken into account in global plate datasets (e.g. Bird, 2003). The Adriatic deformation zones involve a major part of the Italian peninsula and most of the Italian

GPS stations lie inside the deformed Appenninic and Alpine margins of the Adriatic microplate boundaries (Figure 4.1).

Exploiting our new GPS velocity field, we attempt to estimate different Euler poles of the Adriatic microplate using the blind χ^2 test mentioned before. Our best model (AD1) results from the pilot triad (PADO, ROVI, VENE) and supplies a set of 13 consistent sites located both inside and outside the undeformed part of Adriatic plate. The normalized post-fit is rather good (χ_v^2=1.72) and the pole parameters are reasonably uncorrelated, revealing a coherent rigid plate motion. With respect to Eurasia, the AD1 pole and rotation rate are 45.29°N, 7.65°E and 0.216 ± 0.023°/Myr . The χ^2 test rejects systematically all the sites located inside the deformed area S of 44°N (Figure 4.3) producing a significant misfit in the south Adriatic region (AMUR, CADM, DUBR, MATE, SCTE), where lithospheric buckling is active (Doglioni et al., 1994). These sites move to the N instead of NNE predicted from AD1 motion (Figure 4.5). On the other hand, the consistency of these sites in defining a separate south Adriatic block is poor and leads to a bad-conditioned pole estimate. In alternative, considering the entire Adriatic block as a whole (AD1 plus south Adriatic sites) the fit gets even worse (χ_v^2 = 17.08), the relative pole shifts to west 44.34°N, 3.78°E and the rate halves to 0.123 ± 0.030°/Myr.

A further model (AD2) is instead computed selecting eight GPS stations located in the Po basin, within the red line of Figure 4.1, the less deformed part of the Adriatic plate (exception is SFEL, probable outlier). In this case the estimates present a higher misfit (χ_v^2 = 6.98) with respect to AD1; the relative pole is near AD1 (45.45°N, 8.57°E) but the rotation rate is much higher (0.327 ± 0.103)°/Myr (Figure 4.5). Although the rotation rates are different (AD1 about 1.6 times AD2), the high uncertainty of the AD2 estimate prevents a reliable distinction from AD1. The Adriatic poles with respect to Eurasia and ITRF2005 are reported in Tables 4.4, 4.5 and 4.7; those in HSRF are in Table 4.7, and the residual velocities of the sites selected to estmate AD1 and AD2 are reported in Table 4.8, all the Tables at the end of this Chapter.

The high variability observed between different pole realizations is similar to what observed by other authors (Battaglia et al., 2004; Grenerczy et al., 2005), precluding the eventual interpretation of the whole Adriatic region moving as a rigid plate. Neither the more elaborate block model seems to be able to adequately represent the complexity of the Adriatic kinematics (Battaglia et al., 2004). The weakness of the Adriatic pole estimates seems to originate from the particular site placement, restricted in a small region where different geodynamic settings coexist.

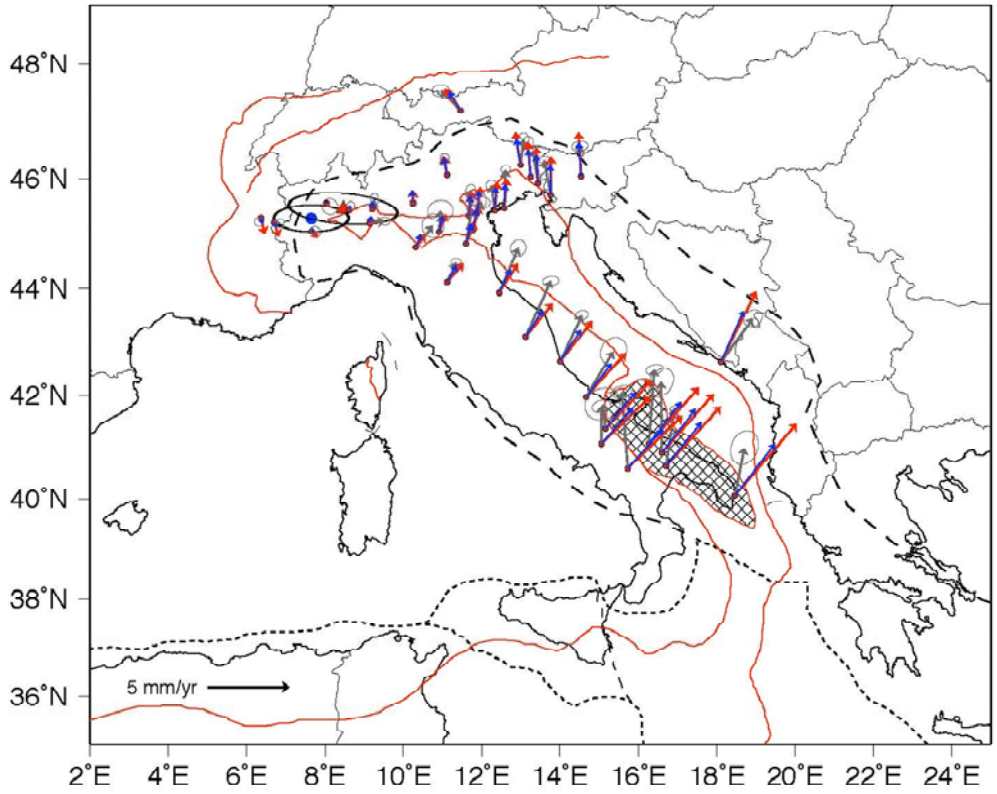

Figure 4.5: Comparison among AD1 (blue vectors) and AD2 (red vectors) solutions for the Adriatic microplate motion with respect to Eurasia, GPS velocities are in grey.

Most of the sites defining AD1 are located in presently active areas deformed either by the Apennines (BRAS, TORI), Alps (CHTL, MODA, PATK, NOVA, TREN), Dinarides (MDEA) or the subsiding foredeep of the Apennines (VENE, PADO, SBPO and ROVI), as shown in Figure 4.1 and Figure 4.2. The sites located in the eastern side of the central-northern Apennines show a gradual decrease in velocity moving NW-ward. This slowing down has generally been interpreted as related to the rotation of the Adriatic microplate with a pole located in NW Italy. However, the sites are all located in the allocthonous hangingwall of the Apennines subduction zone, which is NE-ward retreating along its northern arm. A number of independent evidences indicate that the depth of the slab, the bac-karc spreading, the arc volcanism, the seismicity and the shortening in the accretionary prism decrease moving from the central to the northwestern Apennines. Therefore, the apparent coherence found when estimating poles

is not necessarily related to the rotation of the Adriatic lower plate, but could be attributed to the variation of the Adriatic slab retreat rate relative to the upper European plate, decreasing from SE to NW along the Apennine belt (Doglioni, 1991). Under this hypothesis, any Adriatic pole estimate results weak and rather unconstrained if a comprehensive slab retreat model is not considered.

4.6 Motion relative to the mantle

We compute the motion of the Italian area relative to the HSRF (Figure 4.6), introducing the net rotation angular velocity to switch from the No-Net-Rotation frame (ITRF2005) to the HSRF (Jurdy, 1990; Cuffaro and Jurdy, 2006). In particular, we transform the ITRF2005 velocities into the deep and shallow HSRF (Crespi et al., 2007, Cuffaro and Doglioni, 2007), assuming a lithospheric net-rotation angular velocity computed by Crespi et al. (2007), (Chapter 3) . For each site, we apply the simple linear relationship, valid if velocities are expressed in geocentric Cartesian coordinates

$$\vec{V}_{HSRF} = \vec{V}_{NNR} + \vec{V}_d$$

where $\vec{V}_d$ is the velocity contribution due to the net rotation of lithosphere. It is possible to apply this simple addition under the hypothesis that introducing the Adriatic plate into the global model does not affect significantly the estimate of the net rotation vector.

In the deep HSRF the motion of Adriatic area is very low, while in the shallow HSRF it is SW-ward at about 5 cm/yr. The HSRF velocity directions are not truly consistent with the direction of mantle flow, as detected by seismological methods (Figure 4.7, Lucente et al., 2005).

The shear wave splitting technique (e.g., Savage, 1999) is an independent tool for detecting the seismic anisotropy in the asthenosphere, which is considered the preferential orientation of olivine crystals in a sheared flowing mantle (Silver and Holt, 2002). At global scale, the direction of the anisotropy between lithosphere and underlying mantle (e.g., Fisher et al., 1998; Montagner, 2002) aligns quite consistently with the absolute plate motions reconstructions, apart along subduction zones or other mantle anomalies. In the Italian area, this analysis shows seismic anisotropy W-E directed in most of the Tyrrhenian Sea, becoming parallel to the subduction strike along the Apennines (e.g. Lucente et. al., 2006; Baccheschi et al., 2007). This is consistent with a W to E mantle flow that is kinematically required by the E-ward slab retreat, regardless it is the cause or the consequence of the rollback (Doglioni et al., 1999). Since the Adriatic slab sinks even if the lower plate is diverging

relative to the upper plate, it confirms how the retreat is related to the interplay between slab and the hosting mantle, i.e., slab pull or E-ward mantle flow. However, most of the subducted Adriatic plate beneath the Apennines can be inferred as continental on the basis of the passive continental margin sediments accreted in the accretionary prism. Continental lithosphere is by definition lighter than the underlying mantle, questioning the role of the slab-pull.

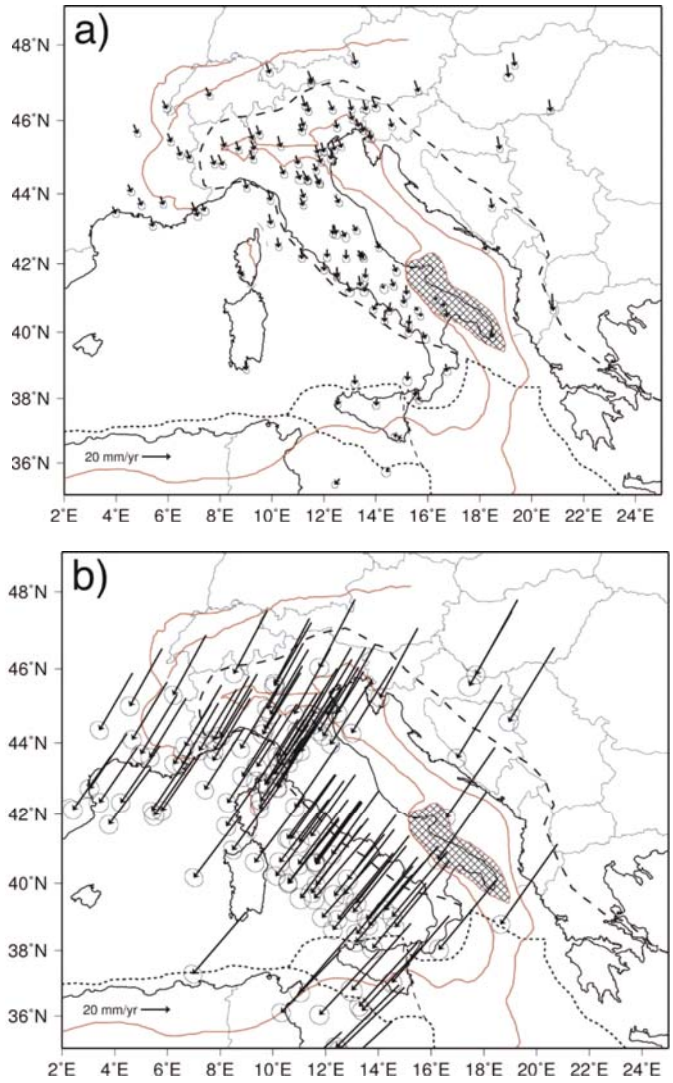

Figure 4.6: Velocities in the deep (a) and shallow (b) hotspot reference frames of Crespi et al. (2007).

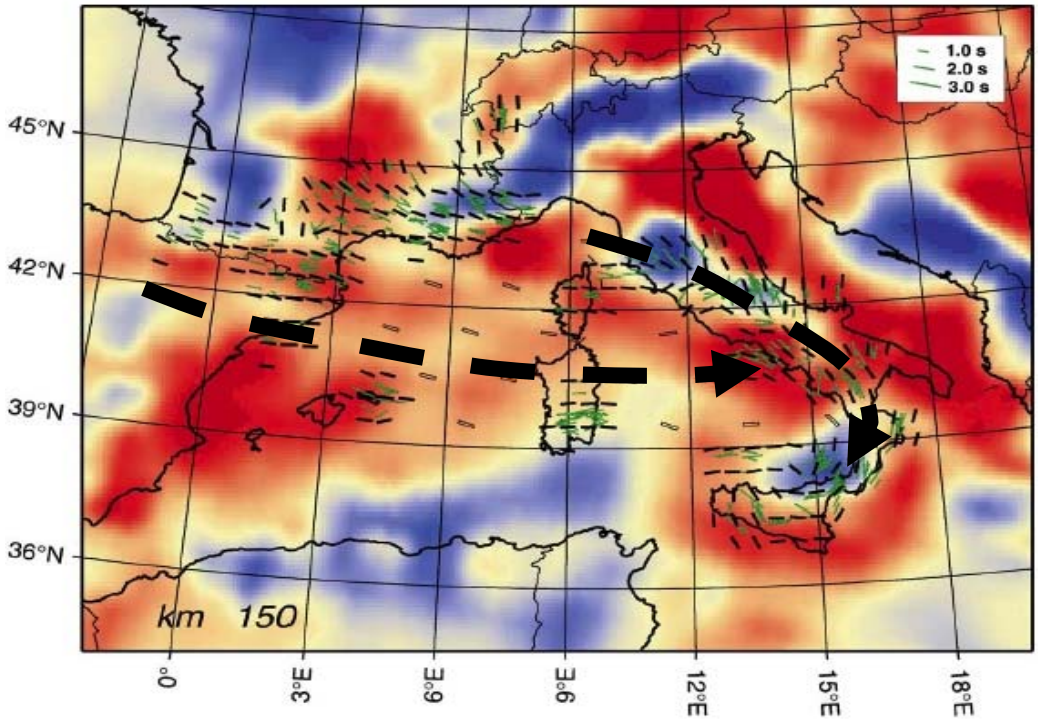

Figure 4.7: The shear wave splitting technique detects the elastic anisotropy in the Earth's interior related to the preferred orientation of minerals in the flow or deformation direction. The horizontal mantle flow pattern in the Italian area is defined by the directions indicated by the black bars. Large dashed arrows indicate the possible circulation around the slab. P-wave velocity anomalies at 150 km depth (red negative, blue positive) in the background (modified from Lucente et al., 2006).

According to this complicated framework, we think that it is not possible to infer geodynamic conclusions about the Italian area by applying a global scale model; we rather prefer to analyze the velocity field under a different approach.

4.7 Basic kinematics along a subduction in the upper plate reference frame

In order to describe the details of the kinematics across the Apennine belt, we wish to recall first some simple concepts on the subduction kinematics (Doglioni et al., 2006).

Let us consider a reference frame with three points, one attached to the upper plate (U), a second attached to the lower plate (L), and the third on the transient subduction hinge (H), as in Figure 4.8. The point located on the upper plate is taken as fixed, i.e. its velocity is $V_U=0$ by definition. The motion of the two remaining points is considered relative to the fixed upper plate; in this frame, V_L is the velocity of the lower plate and V_H is the velocity of the hinge. If L and/or H move towards the fixed point U, then their velocities are assumed to be negative. If the L and/or H diverge from the upper plate, then V_H and V_L are positive.

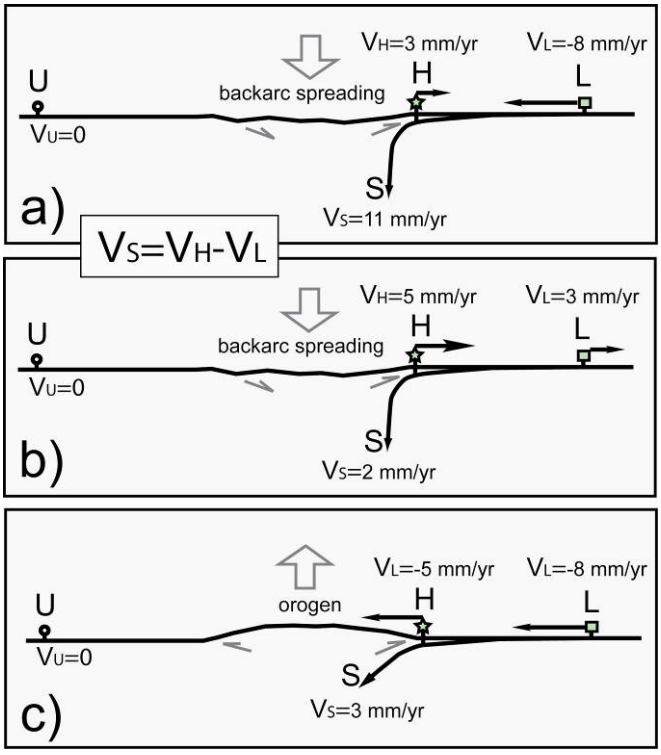

Figure 4.8: Basic kinematics of subduction zones, assuming fixed the upper plate U. The lower plate is L, and the transient subduction hinge, H. The movements diverging from the upper plate are positive, whereas they are negative when converging. The subduction rate is $V_S=V_H-V_L$. Values are only as an example. The case a) has H diverging and L converging, whereas in b) also L is diverging. In these settings, a low prism and back-arc spreading form and they are more typical of W-directed subduction zones. In case c) L and H converge and to form a double verging more elevated orogen (modified after Doglioni et al., 2006).

Particular attention will be given to the effects of the kinematics of lower plate and hinge on the subduction velocity V_S. This is defined as the lithosphere entering the subduction zone per unit time and can be calculated simply by $V_S=V_H-V_L$ (Doglioni et al., 2006). V_L is easily derived from plate motion models. The exact determination of the hinge location is not easy due to the wideness of the rounded area characterized by dip changes from the horizontal lower plate lithosphere to the inclined downgoing slab. In general, the location of the hinge zone has been assumed to be close or coincident with that of the subduction trench (e.g. Heuret and Lallemand, 2005). However, the amount of accretion, i.e., the mass transfer from the lower to the upper plate, increases the volume of rocks in the hangingwall of the slab, partly inhibiting the bac-karc spreading. Asthenospheric intrusion at the subduction hinge can also decrease the space for the back-arc spreading. Moreover, the extension in the hangingwall of the subduction hinge also contributes to render difficult the inference of the exact location of the subduction hinge from surface observations. As explained in detail in Doglioni et al. (2007), due to the complexity of defining an accurate determination of H, the value of V_H is possibly underestimated, so that V_S has to be considered only as a minimum estimate of the subduction rate.

In order to show that different kinematic and tectonic settings coexist along a single subduction zone, with the aim of quantifying even as minimum estimates the different subduction rates of the Adriatic plate, we have analyzed the motions of selected, mostly Italian, GPS stations located on upper and lower plates and on the accretionary prism along sections through the Apennines.

4.8 Variable rates along the Apennines subduction

The horizontal GPS velocities are projected along some representative sections (Figures 4.3, 4.9, 4.10) in order to highlight the different velocity trends across and along the Apenninic belt and to compare the components of V_H and V_L perpendicular to the trench (Figure 4.11, Figure 4.12).

From this paper and other analyses (Devoti et al., 2002; Oldow et al., 2002; Hollenstein et al., 2003; Battaglia et al., 2004; Serpelloni et al., 2005), the Corsica-Sardinia block (represented by CAGL and AJAC) displays a motion consistent with Eurasia. This block is considered a remnant of the upper plate boudinage in the bac-karc setting of the Apennines subduction (Gueguen et al., 1997). Therefore Corsica-Sardinia can be chosen as the upper plate of the

subduction system and both CAGL and AJAC can be considered representative of U to select sections perpendicular to the Apennine chain (Figure 4.3). In Figure 4.9, the extensional and compressional regimes with respect to Eurasia are differentiated respectively by white and grey half spaces.

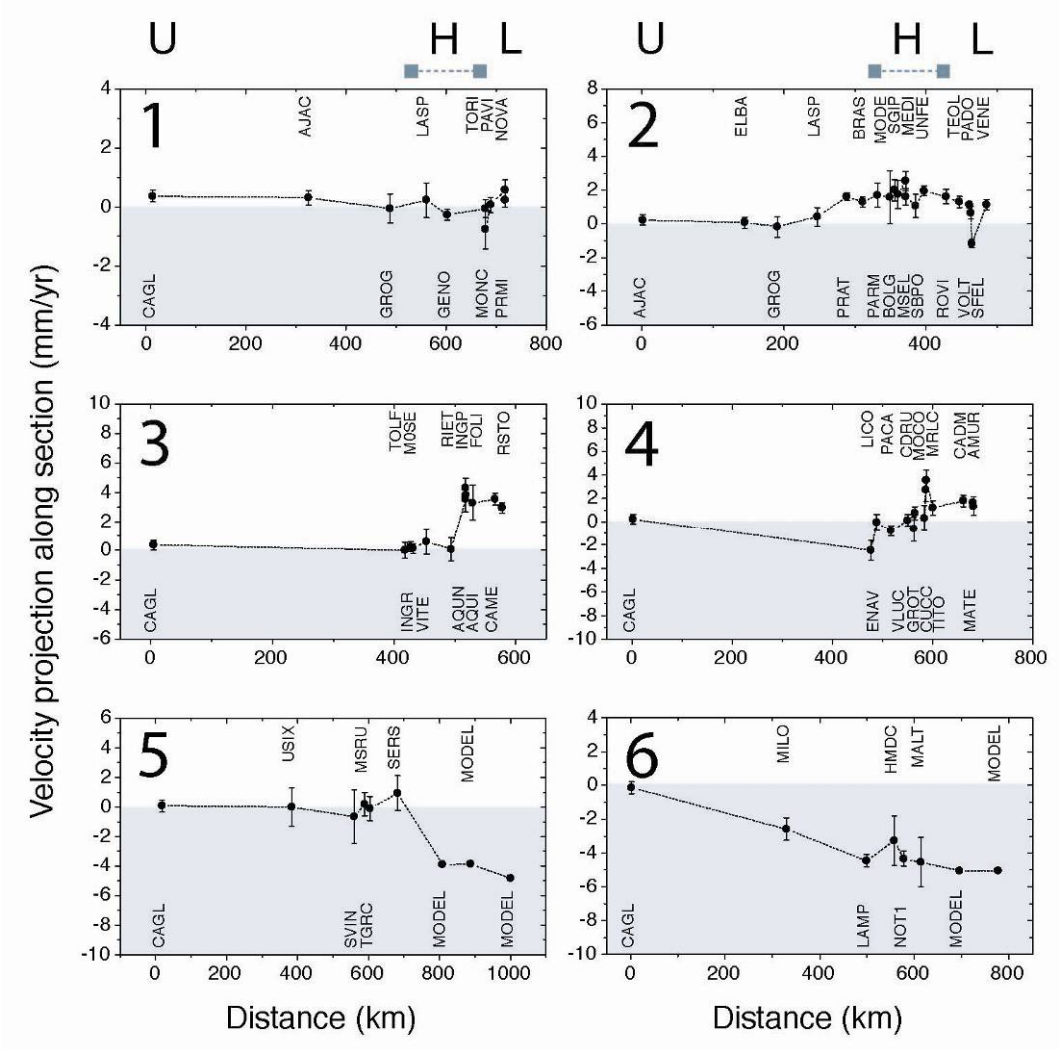

Figure 4.9: Residual velocity components with respect to Eurasia and uncertainties at 68% probability, plotted as a function of distance along the sections of Figure 4.3. Grey and white indicate respectively the areas of convergence and extension with respect to the upper plate U (V_U=0), defined by the Eurasian frame, Corsica (AJAC) - Sardinia (CAGL). H, subduction hinge (the grey bar indicates uncertainty of its location), and L, lower plate. In sections 5 and 6, with MODEL are indicated hypothetical African sites whose velocities are computed from our Africa-Eurasia rotation vector.

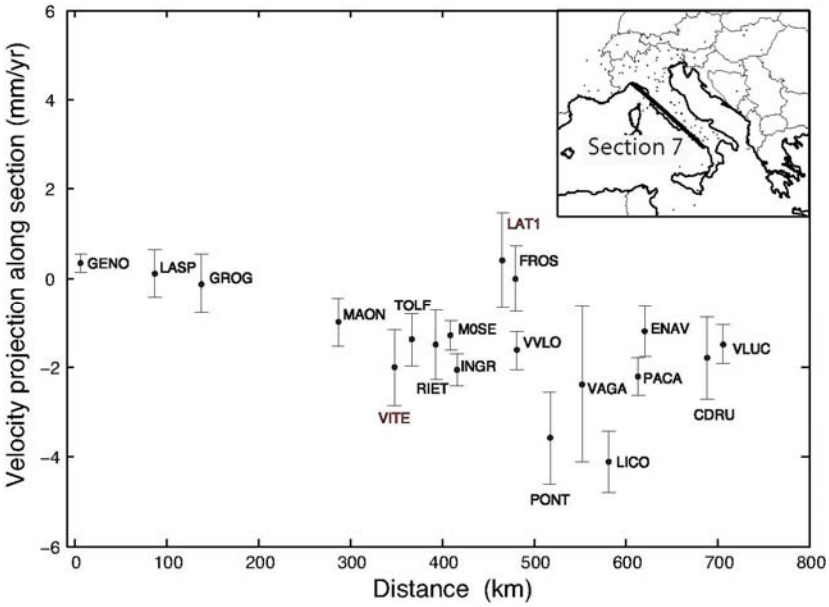

Figure 4.10: Residual velocities with respect to Eurasia. Along the Tyrrhenian side of the belt an unexpected along strike compression is visible, with the southern sites moving NW-ward faster than the northern sites.

Due to the sparse order distribution of the GPS sites and the presence of Adriatic Sea, section 2 is the only one entirely crossing the Apenninic belt, and ending toward the Venice area, considered part of the stable foreland in the Adriatic lower plate. The extension smoothly starts at LASP station, near the eastern margin of the Tyrrhenian Sea (Figure 4.2), reaching a maximum of about 2 mm/yr. In sections 3 and 4, crossing the Tyrrhenian Sea and the central and southern Apennines, the transition is steeper and the extension reaches its maximum value, about 3-4 mm/yr.

Exceptions to the extensional behavior are section 1, where neither extension nor compression is prevalent, and section 4, site ENAV, located in the Neapolitan volcanic area. In section 5 the limited number of GPS sites and the geographical shape of the Calabria region (Figure 4.3) prevent a robust kinematic definition; however a low extension rate of about 1 mm/yr is identified across the southern Tyrrhenian Sea. Conversely, section 6 displays an unambiguous convergence trend. In these last two sections are shown hypothetical African sites whose velocities are computed by our Africa-Eurasia rotation vector. As expected, all these African sites lie well below the

zero line, in the convergence grey area.

The increased density of GPS sites along the western Tyrrhenian Apennines strike allows evidencing a rather well defined pattern of NW-directed residual velocities, showing a compression component from SE to NW (Figure 4.10). In the Calabrian arc the transition between the NW and the NE velocity directions occurs at about 40°N (Figure 4.3) and corresponds to the paleomagnetic declination variations evident in Pleistocene sediments (Sagnotti and Meloni, 1993). It is unclear yet the cause of this compression component able to produce a mean velocity variation from about 2.4 to 0 mm/yr along this section. In our opinion it is not possible to simply hypothesize a residual component of the Africa–Eurasia convergence, rather a coupling between lithosphere and mantle circulation around the slab (Montuori et al., 2007; Baccheschi et al., 2007). Alternatively, it could represent part of the dissipation of the Africa-Eurasia relative motion, or an unidentified tectonic deformation associated to the counterclockwise rotation in the western Apennines back-arc setting.

We further analyzed the Apennine belt using six cross-sections (Figure 4.11) on which we projected the velocity component relative to CAGL or AJAC. These sections highlight five different geodynamic settings.

From Corsica to Liguria and south Piemonte in the northern Apennines, there is no significant relative motion: H, L and U have consistent motion within the errors (Figure 4.12a), although GENO might not correctly represent the subduction hinge, being located in the stretched Alps. Moving from the Corsica-Sardinia block to NE, through Emilia and Veneto regions, the site of UNFE, assumed to be fairly representative of the subduction hinge, is moving away from the upper plate faster than sites located more to NE in the foreland, like VENE, so that $V_H > V_L$ (Figure 4.12b). Ongoing extension documented in the central-northern Apennines (Hunstad et al., 2003) is consistent with the positive value of V_H (i.e., the hinge migrates toward the foreland), that explains the active spreading of the Tyrrhenian back-arc basin. The same geodynamic setting is evidenced in Figure 4.12c.

In southern Apennines the setting changes (Roure et al., 1991), suggesting a slower velocity of the diverging hinge with respect to the foreland, i.e., both H and L move away from the upper plate, but the lower plate L seems faster. In this setting the slab is paradoxically moving away with respect the upper plate and subduction would result negative, Figure 4.12d. This is compatible with the paucity of geological and geophysical data supporting active compression at the southern Apennines front, while active extension is widespread in the belt (Scrocca et al., 2005).

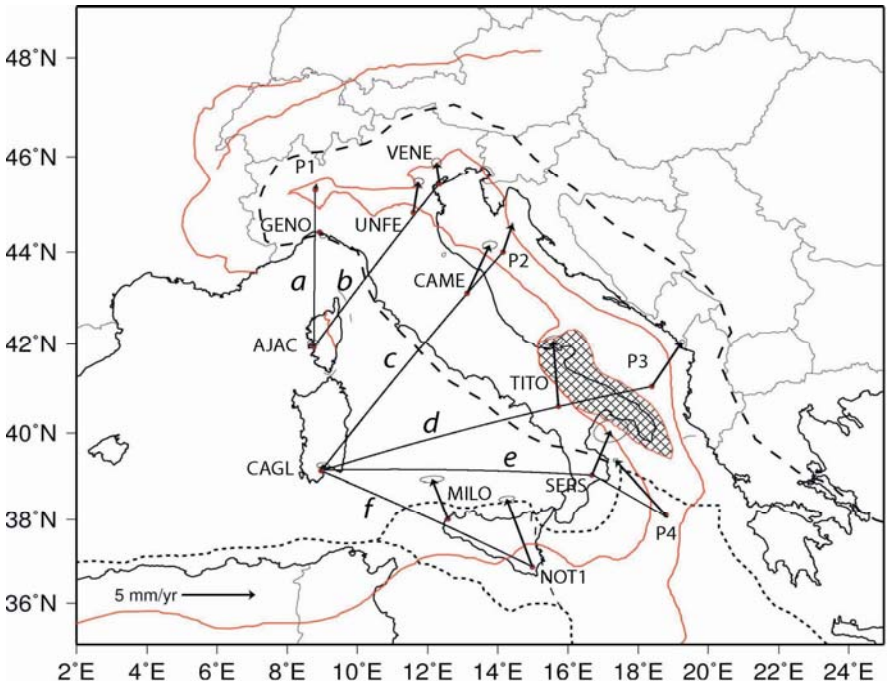

Figure 4.11: Selected sections across the Apenninic arc: Cagliari (CAGL) and Ajaccio (AJAC), which are on the Sardinia-Corsica continental boudin, are considered part of Eurasia. GENO, Genova; UNFE, Ferrara; VENE, Venice; CAME, Camerino; TITO, Tito; SERS, Sersale; MILO, Trapani; NOT1, Noto; P1-2-3-4 velocities come from the Adriatic-Eurasia and Africa-Eurasia rotation vectors.

In a cross-section from Sardinia to Calabria and Ionian basin, the setting changes again (Figure 4.12e). In this case, the Ionian (L) is converging relative to U. During present times, it is doubtful if and how fast Calabria (H) is still moving E-ward relative to Sardinia (U), in the frame of still active extension of the Tyrrhenian (Goes et al., 2004; Pondrelli et al., 2004; D'Agostino and Selvaggi, 2004). Anyway our GPS data seem to support a still active extension at a rate of about 1.1 mm/yr (Figure 4.12, e). On the other hand, both seismicity and seismic reflection profiles suggest active, although slow, extension in the Tyrrhenian Sea (Scrocca et al., 2003; Doglioni et al., 2004; Pondrelli et al., 2004; Chiarabba et al., 2005). An increase of accretion in the Ionian prism of the Apennines should provide an upper plate crustal thickening and widening, partly preventing back-arc extension. Along this section we observe the fastest subduction rate (Figure 4.12e) with a minimum value of about (5.0 ± 2.2) mm/yr.

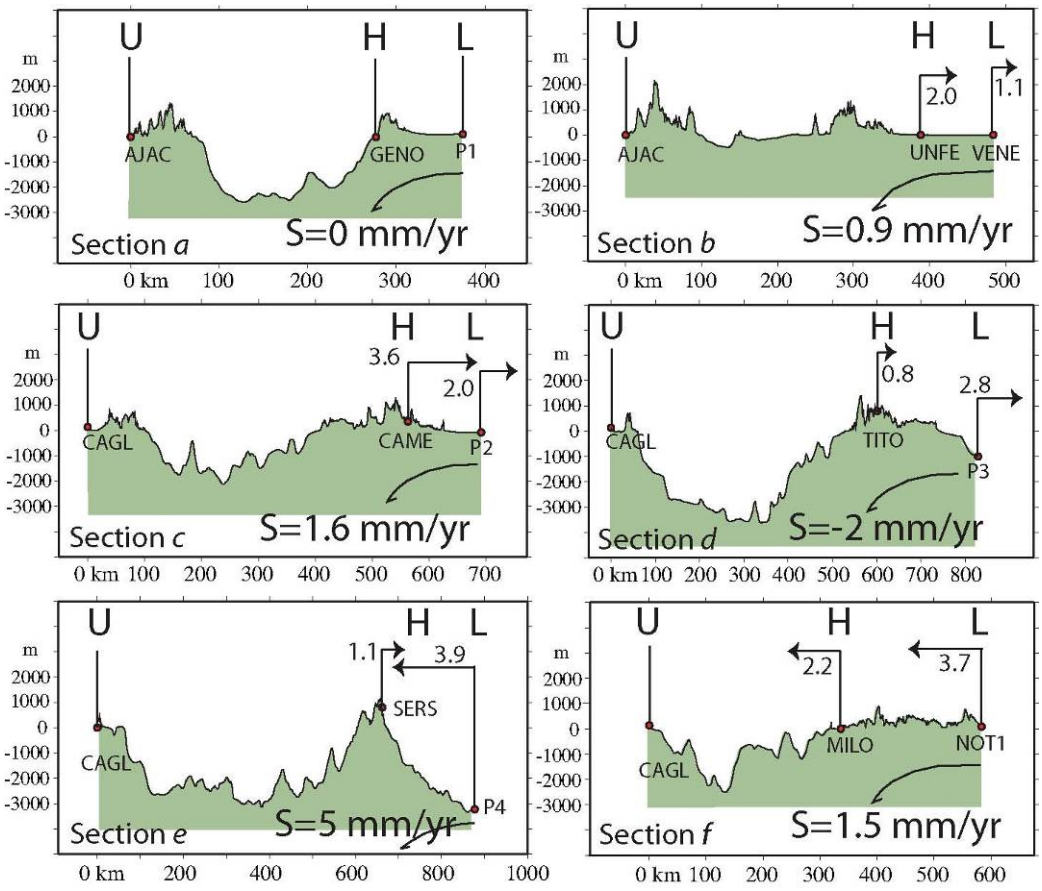

Figure 4.12: Topographic profiles along the sections shown in Figure 4.11. Along the Apenninic arc different relationships between U, H and L occur. The upper plate U is considered fixed (Sardinia-Corsica, CAGL and AJAC). The inferred subduction rates (S) are minimum estimates, as explained in Doglioni et al. (2007). Note that each section has different geodynamic settings and variable subduction rates. The rates of H and the lower plate L, projected on the sections, are in mm/yr. Section a) shows no significant relative motion and hence yields a zero subduction rate. Both sections b) and c) have H diverging from U faster than L. Section d) has the subduction rate paradoxically negative, pointing for a detachment of the slab but from the surface. The fastest subduction rate is along the Calabrian arc (section e) where H diverges and L converges. Section f) rather shows L converging faster than H.

From Sardinia to Sicily, and from Sicily foreland to S, the Africa velocities (V_L) are oriented towards CAGL, but in northern Sicily (H) the movement is slower than in the foreland to S. In this setting (Figure 4.12f), H is approaching U, with a slower velocity than the lower plate L, i.e., $|V_L|>|V_H|$. This is consistent with the compressive seismicity both south and north of Sicily (Chiarabba et al., 2005). The back-arc area along this section is then shrinking.

However, in the southern Tyrrhenian Sea, different settings may coexist in a single area due to the 3D nature of the subduction. For example, in northern Sicily, convergence of the hinge relative to the upper plate in a NW-SE section concurs with an E-W extension related to the divergence of the hinge in Calabria. Therefore compressive-transpressive tectonic features overlap with extensional-transtensional faults in the southern Tyrrhenian Sea. This is consistent with seismic section interpretation and seismicity of the area (Chiarabba et al., 2005; Jenny et al., 2006; Montuori et al., 2007).

4.9 Discussion and conclusions

The updated GPS velocity field of the Italian area shown in this paper gives a detailed view of the motion around the Apennines, an accretionary wedge formed in the hangingwall of a W-directed subduction zone. The Apennines slab is composed by at least four different lithospheric segments with variable thickness, composition and velocity (the Adriatic, Ionian, Sicily and Africa domains). Each segment behaves differently in terms of tectonic setting and subduction rate. Extension appears more concentrated across the Apennines belt, whereas compression is evident along most of the eastern side. An unexpected along strike SE-NW compression is detected along the Tyrrhenian side of the western Apennines. Any attempt to estimate a rigid Adriatic pole results in a weak and rather unconstrained estimate. Consequently, we suggest that the variable Adriatic slab retreat rate could play an important role in the kinematic setting of the region.

In the Sicilian segment, the Tyrrhenian margin is undergoing a NNW-SSE-directed compression along the lithospheric heterogeneity (the transition between continental Sicily and the southern Tyrrhenian oceanic crust), while extension is contemporaneously operating along the E-W direction. Slow extension rate (at mm/yr level) is detected in the Tyrrhenian back-arc basin. A decrease or even a stop of the rifting in the Tyrrhenian Sea (in spite of normal fault-related seismicity (Pondrelli et al., 2004) has been proposed as

related to the end of the slab rollback (D'Agostino and Selvaggi, 2004), although active convergence is documented between the Ionian Sea and the upper plate (e.g. Sardinia). As an alternative explanation, an increase of mass transfer from the lower to the upper plate in both areas has been proposed (Doglioni et al., 2007). Normal faulting in the prism may further enlarge the upper plate close to the subduction hinge, inhibiting the widening and measuring of the back-arc spreading. Nevertheless an extensional component is still visible (Figure 4.12e).

The Apennines are an example denoting variable rates of subduction and different interplay between the behavior of H and L relative to U. The subduction rate is decreased or increased as a function of whether the subduction hinge converges or diverges relative to the upper plate, plus the convergence or divergence rate of the lower plate. The five main settings are 1) almost null motion of H and L (Figure 4.12a, Liguria); 2) H diverges faster than L relative to U (Figure 4.12b and c, northern and central Apennines); 3) H diverges slower than L (Figure 4.12d, Puglia); 4) H diverges and L converges (Figure 4.12e, Calabria); 5) H converges slower than L (Figure 4.12f, Sicily). The transition between the different geodynamic settings can be either gradual (e.g. from section a to c), or along restricted transfer zones (e.g. between sections: c-d, Tremiti alignment; d-e, Apulian escarpment and e-f, Malta escarpment). The subduction rate is generally positive and ranges between 0 and 5 mm/yr from northern Apennines to the Calabrian arc; V_S is negative (Figure 4.12d) when the lower plate diverges faster than the hinge. This kinematic setting seems a paradox but might represent the final evolution of the subduction zone.

At this stage we can infer some general considerations: 1) Variable geodynamic settings may coexist along a single subduction system (Figure 4.12); 2) The subduction rate V_S is not equal to the convergence rate, but it is rather given by the relation $V_S=V_H-V_L$ (Figure 4.8); 3) Subduction can occur even if the lower plate L diverges from the upper plate, if H moves away faster than L (Figure 4.12); 4) In some areas, as in the southern Tyrrhenian sea, the 3D geometry of the back-arc spreading enables the coexistence of different geodynamic settings, e.g., NW-SE compression and E-W extension are co-working in the same area.

The presence of different geodynamic settings supports a passive nature of these plate boundaries, which can rather be controlled by the far field plate velocity and the slab-mantle interaction, e.g. the relative E-ward mantle flow detected at a global scale in the HSRF (Crespi et al., 2007).

Table 4.1: Italian network, coordinates in degree, horizontal velocities in mm/yr (ITRF2005 Eurasia reference frame), uncertainties, correlation between N and E components and time span

Site	Lon	Lat	E	N	±E	±N	corr	T
ACOM	13.515	46.547	0.29	0.29	0.55	0.37	0.07	3.5
AFAL	12.175	46.527	1.06	0.58	0.40	0.34	0.04	3.5
AJAC	8.763	41.927	-0.04	0.31	0.39	0.23	-0.03	3.9
AMUR	16.604	40.907	-0.06	4.28	0.77	0.86	0.26	1.6
AQUI	13.350	42.368	1.83	3.52	0.41	0.33	0.17	4.0
AQUN	13.379	42.337	1.73	3.20	0.86	0.88	0.08	1.5
BIEL	8.048	45.560	0.19	-0.20	0.48	0.49	-0.05	2.1
BOLG	11.357	44.500	-1.15	3.28	0.89	0.47	0.05	2.1
BRAS	11.113	44.122	0.56	1.18	0.30	0.29	0.06	4.2
BRIX	10.233	45.564	0.04	0.00	0.22	0.22	0.01	4.0
BSSO	14.594	41.545	1.12	2.77	0.62	0.49	0.20	2.0
BZRG	11.337	46.498	-0.71	0.22	0.27	0.21	0.02	4.0
CADM	16.274	41.077	0.32	4.54	0.53	0.33	0.29	3.3
CAGL	8.973	39.135	0.11	0.38	0.42	0.20	-0.01	4.2
CAME	13.124	43.111	1.54	3.40	0.49	0.29	0.14	4.0
CANV	12.435	46.008	-0.57	1.92	0.76	0.86	0.04	2.6
CAVA	12.583	45.479	0.07	2.32	0.29	0.25	0.07	4.0
CDRU	15.305	40.489	-1.16	1.39	1.06	0.69	0.20	1.5
COMO	9.096	45.802	0.74	-1.19	0.27	0.32	-0.02	4.0
CUCC	15.816	39.993	1.71	3.46	1.02	1.01	0.22	1.5
DUBR	18.110	42.649	1.95	2.64	0.57	0.52	0.19	2.9
ELBA	10.211	42.752	-0.44	0.41	0.45	0.23	0.03	4.0
ENAV	14.335	40.582	-0.49	1.24	0.72	0.25	0.22	2.2
FOLI	12.701	42.948	1.40	3.20	0.75	1.46	0.06	1.0
FRES	14.669	41.973	1.66	2.81	0.80	0.84	0.15	1.5
FROS	13.349	41.648	0.37	0.43	0.83	0.65	0.08	1.4
GBLM	14.026	37.990	-0.17	2.98	0.75	0.60	0.10	2.1
GENO	8.921	44.419	0.24	-0.25	0.21	0.18	-0.03	4.2
GRAS	6.921	43.754	0.45	-0.05	0.31	0.22	-0.10	4.2
GRAZ	15.494	47.067	0.97	0.13	0.27	0.26	0.08	4.2
GROG	9.892	43.426	-0.22	-0.06	0.79	0.49	0.00	1.6
GROT	15.060	41.072	-0.01	2.29	0.58	0.39	0.24	2.2
GSR1	14.544	46.048	-0.10	1.80	0.49	0.29	0.11	4.0
HFLK	11.386	47.312	0.36	0.14	0.42	0.52	0.01	4.0
HMDC	14.783	36.958	-0.61	4.65	1.70	0.93	0.24	1.7
INGP	13.316	42.382	2.07	3.95	0.82	0.49	0.17	3.4
INGR	12.515	41.827	-1.36	1.59	0.43	0.23	0.15	4.0
LAMP	12.606	35.499	-2.89	3.55	0.38	0.32	0.22	4.1
LASP	9.840	44.073	0.36	0.24	0.51	0.59	0.01	1.7

LAT1	12.901	41.470	1.02	0.53	1.14	0.99	0.01	0.9
LEC1	9.407	45.857	0.17	0.35	0.38	0.31	-0.02	3.5
LICO	14.050	40.876	-3.42	2.35	0.87	0.35	0.19	2.1
M0SE	12.493	41.892	-0.86	0.99	0.37	0.27	0.14	4.0
MALT	14.526	35.837	-1.68	5.29	1.45	1.45	0.07	0.7
MAON	11.131	42.428	-0.90	0.48	0.58	0.48	0.06	1.8
MATE	16.705	40.648	0.51	3.50	0.26	0.18	0.34	4.2
MDEA	13.436	45.924	-0.34	1.97	0.26	0.24	0.08	3.9
MEDI	11.647	44.519	2.04	0.51	0.68	0.32	0.07	4.2
MERA	11.157	46.668	0.17	-0.60	0.60	0.67	0.00	2.1
MILO	12.584	38.007	-1.09	2.85	0.81	0.22	0.19	4.0
MOCO	15.159	41.370	-0.17	1.50	1.09	0.98	0.16	1.3
MODE	10.949	44.628	0.76	1.39	1.93	1.34	0.00	1.0
MONC	7.927	45.073	1.21	-0.70	0.51	0.66	-0.05	1.8
MPRA	12.988	46.240	0.19	1.54	0.34	0.41	0.06	4.0
MRLC	15.489	40.756	1.96	5.20	0.89	0.63	0.26	2.2
MSEL	11.647	44.519	2.13	1.59	0.64	0.53	0.06	2.1
MSRU	15.508	38.263	0.62	3.71	0.79	0.77	0.26	1.6
NOT1	14.990	36.875	-1.76	4.88	0.53	0.20	0.33	4.2
NOVA	8.614	45.447	0.11	0.24	0.25	0.25	-0.04	4.0
ORID	20.794	41.127	0.71	-3.03	0.45	0.29	0.43	4.0
OSJE	18.681	45.560	0.60	0.30	0.36	0.44	0.21	2.7
PACA	14.556	40.870	-1.43	1.72	0.45	0.38	0.22	3.2
PADO	11.896	45.411	0.24	0.63	0.29	0.40	0.06	4.0
PARM	10.312	44.764	1.07	1.32	0.67	0.71	0.00	1.4
PAVI	9.136	45.202	0.93	0.11	0.32	0.25	-0.02	4.0
PERU	12.394	43.110	0.31	1.01	1.12	1.06	-0.05	1.0
PONT	13.685	41.438	-3.24	1.76	0.90	1.18	0.03	0.8
PRAT	11.099	43.885	0.54	1.60	0.22	0.23	0.06	4.0
PRMI	9.202	45.462	0.15	0.59	0.24	0.33	-0.02	4.0
RIET	12.857	42.407	-1.04	1.09	0.69	0.87	0.09	1.5
ROVE	11.042	45.893	0.32	2.09	0.68	0.59	0.01	2.1
ROVI	11.783	45.086	0.49	1.64	0.55	0.36	0.05	2.1
RSMN	12.451	43.933	1.16	2.72	0.48	0.51	0.09	2.3
RSTO	14.002	42.658	1.32	2.79	0.38	0.32	0.19	4.2
SBPO	10.920	45.050	0.07	1.26	0.78	0.66	0.03	1.8
SCTE	18.467	40.072	0.58	2.91	0.85	1.04	0.20	1.1
SERS	16.689	39.035	1.29	3.14	1.18	0.83	0.24	1.5
SFEL	12.291	45.229	-2.56	0.39	0.29	0.23	0.07	4.0
SGIP	11.183	44.635	1.84	0.81	0.79	0.86	0.04	1.8
SJDV	4.677	45.879	0.20	-0.35	0.28	0.25	-0.14	4.1
SVIN	15.234	38.802	-0.44	1.98	1.82	1.54	0.14	1.0
TEOL	11.677	45.342	0.11	1.51	0.31	0.36	0.05	2.9
TGRC	15.651	38.108	0.38	4.29	0.81	0.44	0.30	3.4
TITO	15.724	40.601	-0.36	4.67	0.63	0.36	0.29	4.0
TOLF	12.000	42.063	-1.01	0.95	0.72	0.34	0.11	3.0

TORI	7.661	45.063	0.23	-0.04	0.31	0.30	-0.07	4.0
TREN	11.122	46.072	-0.16	1.03	0.28	0.23	0.01	3.6
TRIE	13.764	45.709	-0.41	2.13	0.42	0.19	0.10	3.9
UDIN	13.253	46.037	-0.18	2.05	0.35	0.39	0.08	2.7
UNFE	11.599	44.832	0.36	2.16	0.33	0.27	0.06	4.0
UNPG	12.356	43.119	-1.36	0.74	0.28	0.24	0.12	4.0
USIX	13.179	38.707	0.14	1.39	1.31	0.81	0.14	1.3
VAGA	14.234	41.415	0.88	4.53	1.59	1.89	0.18	2.0
VENE	12.332	45.436	-0.20	1.52	0.32	0.31	0.07	4.0
VITE	12.120	42.417	-1.07	1.81	0.89	0.79	0.07	1.5
VLUC	15.266	40.230	-0.46	1.71	0.51	0.32	0.21	4.0
VOLT	11.911	45.384	0.01	1.39	0.26	0.15	0.06	4.0
VVLO	13.623	41.869	-1.44	0.84	0.48	0.38	0.17	4.0
ZIMM	7.465	46.877	0.20	0.29	0.20	0.20	-0.06	4.2
ZOUF	12.974	46.557	-0.08	0.19	0.28	0.27	0.05	4.0

Table 4.2: ARE network, coordinates in degree, horizontal velocities in mm/yr (ITRF2005 Eurasia reference frame), uncertainties, correlation between N and E components and time span

Site	Lon	Lat	E	N	±E	±N	corr	T
BBYS	19.151	48.751	-1.68	-0.19	1.35	0.63	-0.01	3.4
BOGO	21.035	52.476	-0.04	-0.25	0.22	0.17	-0.04	8.3
BOR1	17.074	52.277	0.27	-0.64	0.22	0.17	-0.03	8.3
BRAI	27.973	45.267	-1.85	-2.48	2.20	1.13	-0.06	1.8
BUCU	26.126	44.463	-0.62	-2.09	0.18	0.16	0.13	7.7
BUTE	19.057	47.480	-0.56	0.00	1.61	0.89	0.00	2.2
BZRG	11.337	46.498	0.02	0.57	0.48	0.26	-0.02	8.0
CAME	13.124	43.111	1.65	4.19	0.59	0.29	0.00	6.5
COST	28.658	44.161	-0.22	-4.76	5.25	3.35	-0.03	1.0
CRAI	23.765	44.337	-2.09	-4.22	10.34	5.34	-0.02	1.1
DRES	13.730	51.029	-0.04	-0.07	0.54	0.34	-0.01	7.1
DUBR	18.110	42.649	1.13	3.73	1.39	0.59	-0.03	5.1
GANP	20.323	49.034	-0.70	0.42	1.21	0.67	-0.02	3.1
GOPE	14.786	49.913	0.60	-0.77	0.17	0.13	0.00	8.3
GRAZ	15.494	47.067	0.49	0.13	0.38	0.22	0.00	8.3
GSR1	14.544	46.048	0.38	1.88	1.50	0.68	-0.04	5.8
HFLK	11.386	47.312	0.06	0.29	0.34	0.23	0.02	8.3
JOZE	21.032	52.097	0.70	-0.75	0.21	0.17	-0.03	8.3
KATO	19.036	50.253	1.40	-4.86	1.68	0.84	-0.02	3.3
KRAW	19.921	50.066	0.31	-0.52	0.80	0.46	-0.06	3.9
LAMA	20.670	53.892	-0.48	-0.53	0.36	0.25	-0.03	8.3

MATE	16.705	40.648	0.35	4.10	0.62	0.29	0.04	5.8
MEDI	11.647	44.519	1.40	1.57	0.41	0.24	0.02	8.3
MIKL	31.973	46.972	-1.61	-1.06	0.89	0.50	0.00	4.1
MOPI	17.274	48.372	-0.31	-0.18	0.23	0.16	0.02	8.3
NYIR	22.136	47.835	-0.42	-1.29	1.73	0.80	0.03	4.0
OBE2	11.280	48.086	-0.45	0.02	0.52	0.29	0.00	5.3
ORID	20.794	41.127	0.36	-3.28	0.70	0.32	-0.01	6.3
OROS	20.671	46.555	-0.15	0.96	0.68	0.35	0.02	5.0
OSJE	18.681	45.560	-0.22	0.13	0.65	0.31	0.01	4.9
PADO	11.896	45.411	0.38	0.88	0.74	0.37	-0.01	5.0
PATK	11.460	47.207	-1.20	1.19	0.54	0.38	0.01	8.1
PENC	19.282	47.789	-0.32	-0.42	0.25	0.18	0.01	8.3
PFAN	9.785	47.515	-0.14	0.09	0.40	0.22	0.01	8.3
POLV	34.543	49.602	-1.31	-0.83	0.45	0.30	0.01	5.3
POTS	13.066	52.379	-0.03	-0.87	0.34	0.24	-0.01	8.3
PRAT	11.099	43.885	0.21	2.51	0.97	0.48	0.01	3.4
RAMO	34.763	30.597	-6.71	6.64	1.01	0.57	0.01	7.2
ROVI	11.783	45.086	-0.15	3.19	2.17	1.17	0.02	2.0
SBGZ	13.110	47.803	-0.14	-0.60	0.59	0.36	0.01	7.9
SIBI	24.146	45.781	-0.28	-1.30	3.04	1.57	-0.03	1.7
SOFI	23.395	42.555	0.83	-2.59	0.52	0.30	0.03	8.3
SRJV	18.414	43.867	0.32	1.68	0.40	0.28	0.02	7.0
SUCE	26.237	47.635	0.15	0.57	2.49	1.30	-0.07	1.8
SULP	24.015	49.835	-0.41	-0.37	0.89	0.48	-0.01	5.2
TUBO	16.593	49.205	0.32	-0.46	0.65	0.33	-0.05	5.2
UNPG	12.356	43.119	-0.93	0.06	0.76	0.34	0.00	5.8
UZHL	22.298	48.631	-0.35	-0.97	0.23	0.20	0.01	7.3
VARN	27.923	43.202	-1.59	-2.23	4.00	2.32	-0.04	1.3
VENE	12.332	45.436	0.44	1.63	0.19	0.14	0.04	8.3
VLCH	13.851	46.606	0.99	0.35	0.82	0.40	-0.01	4.4
WROC	17.062	51.113	-0.43	-0.93	0.39	0.25	-0.03	8.3
WTZR	12.879	49.144	0.14	-0.21	0.19	0.15	0.01	8.3
ZECK	41.565	43.788	-2.33	-0.16	0.73	0.46	0.02	5.8
ZIMM	7.465	46.877	-0.14	0.17	0.20	0.15	0.03	8.3
ZOUF	12.974	46.557	-0.33	0.39	1.85	0.92	-0.01	3.7
ZYWI	19.206	49.686	0.16	-0.25	1.16	0.63	-0.03	3.3

Table 4.3: REGAL network, coordinates in degree, horizontal velocities in mm/yr (ITRF2005 Eurasia reference frame), uncertainties, correlation between N and E components and time span

Site	Lon	Lat	E	N	±E	±N	corr	T
AJAC	8.763	41.927	-0.57	0.50	0.49	0.43	-0.01	3.5
BRST	-4.497	48.380	0.41	1.49	0.80	0.58	-0.01	4.6
CAGL	8.973	39.135	-0.27	0.43	0.29	0.21	-0.07	7.4
CHIZ	-0.408	46.133	1.05	1.63	0.79	0.71	-0.01	2.8
CHRN	4.862	43.881	0.25	0.65	0.62	0.63	-0.01	2.7
CHTL	6.359	45.304	-0.10	-0.28	0.31	0.30	0.01	4.3
EBRE	0.492	40.820	-0.03	0.63	0.37	0.28	-0.08	7.5
FCLZ	5.986	45.642	0.10	0.53	0.30	0.30	-0.01	5.1
GENO	8.921	44.419	0.07	0.33	0.32	0.30	-0.01	6.2
GRAS	6.921	43.754	-0.36	0.33	0.19	0.13	-0.12	7.6
GRAZ	15.494	47.067	-0.11	-0.01	0.15	0.14	0.01	7.6
HFLK	11.386	47.312	0.19	0.48	0.17	0.17	-0.02	6.9
JOUX	5.796	46.528	0.25	0.39	0.46	0.48	-0.01	3.3
JOZE	21.032	52.097	-0.08	-0.71	0.24	0.18	-0.09	7.6
KOSG	5.810	52.178	0.44	0.21	0.20	0.14	-0.06	7.6
LAMP	12.606	35.499	-3.82	3.50	0.61	0.45	0.00	4.3
MANS	0.155	48.018	0.33	1.44	0.68	0.55	-0.05	4.2
MARS	5.354	43.278	-0.65	0.82	0.37	0.35	-0.02	5.0
MATE	16.705	40.648	0.73	3.85	0.22	0.15	-0.08	7.6
MEDI	11.647	44.519	1.94	2.25	0.19	0.17	-0.04	7.4
MICH	5.717	43.924	-0.05	0.40	0.31	0.28	-0.03	5.0
MODA	6.710	45.213	0.33	-0.04	0.28	0.27	-0.03	4.8
MTPL	3.865	43.637	0.31	0.72	0.45	0.40	-0.01	4.2
NICE	7.300	43.725	0.47	1.08	0.70	0.73	-0.01	2.6
NOT1	14.990	36.875	-2.03	4.63	1.20	0.90	-0.03	2.5
NOTO	14.990	36.875	-3.36	3.53	0.45	0.36	0.01	4.7
OBER	11.280	48.086	-0.26	0.18	0.29	0.33	0.00	4.6
POTS	13.066	52.379	-0.28	-0.61	0.16	0.14	-0.03	7.6
RABT	-6.854	33.997	-4.45	4.02	1.19	0.77	-0.03	3.2
SAUV	4.467	44.255	0.01	0.65	0.46	0.45	-0.01	3.7
SFER	-6.206	36.464	-2.62	2.05	0.58	0.43	-0.04	7.3
SJDV	4.677	45.879	0.15	0.44	0.28	0.24	-0.03	5.8
SOPH	7.054	43.611	-0.12	0.30	0.71	0.74	0.00	2.5
STJ9	7.684	48.621	0.72	0.07	0.38	0.40	0.00	3.6
TETN	-5.363	35.561	-4.33	1.95	1.53	1.02	0.00	3.2
TLSE	1.481	43.560	0.38	0.68	0.94	0.82	-0.01	2.4
TORI	7.661	45.063	-0.04	-0.24	0.27	0.25	-0.05	6.8
TOUL	1.481	43.560	-0.32	0.77	0.50	0.44	-0.02	3.9
UPAD	11.878	45.406	0.55	2.35	0.24	0.26	-0.03	5.9

VILL	-3.952	40.443	0.00	1.33	0.45	0.33	-0.05	7.6
WELS	7.351	48.415	0.57	0.36	0.74	0.79	-0.02	2.7
WSRT	6.605	52.914	0.35	0.40	0.24	0.23	0.02	6.1
WTZR	12.879	49.144	-0.02	-0.09	0.13	0.14	0.00	7.5
ZIMM	7.465	46.877	0.78	0.54	0.19	0.18	-0.06	7.6

Table 4.4: ITRF2005 poles, angular velocities and errors at 68% probability level

Plate	Lon	Lat	s_{maj}	s_{min}	Az	Ω	±Ω	X^2	N
	º	º	º	º	º	º/Myr	º/Myr		
EURA	-95.72	55.85	1.2	0.1	-116	0.266	0.002	1.46	24
AFRI	-82.96	49.09	1.2	0.5	92	0.267	0.002	2.04	10
AD1	-43.38	63.44	6.1	0.1	92	0.418	0.024	1.72	13
AD2	-28.40	62.01	15.40	0.2	99	0.513	0.218	6.98	8

Table 4.5: ITRF2005 angular velocity components and covariance matrix

Plate	ω_X	ω_Y	ω_Z	σxx	σyx	σyy	σzx	σzy	σzz
		º/Myr				(rad/Myr)² ·10⁻⁹			
EURA	-0.015	-0.149	0.220	1.025	0.152	0.055	1.155	0.180	1.376
AFRI	0.021	-0.173	0.201	0.848	0.081	0.258	-0.051	-0.020	0.375
AD1	0.136	-0.128	0.374	43.524	8.673	1.816	44.567	8.898	45.709
AD2	0.212	-0.114	0.453	183.633	36.331	7.297	188.058	37.227	192.680

Table 4.6: Sites selected to estimate the ITRF2005 rotation poles: coordinates in degree, residual velocities and error ellipsis axes in mm/yr, azimuth of the semi-major axis in degree.

SITE	Lon	Lat	E	±E	N	±N	Up	±Up	s_{maj}	s_{min}	Az
EURA											
BOGO	21.035	52.476	0.11	0.74	-1.00	1.05	-1.81	4.77	1.05	0.74	-178.0
CAGL	8.973	39.135	-0.14	0.26	0.10	0.24	0.25	0.60	0.26	0.24	105.2
CASC	-9.419	38.693	0.18	1.33	0.76	1.03	0.95	3.79	1.33	1.03	88.1
GENO	8.921	44.419	0.39	0.51	-0.18	0.60	0.39	2.08	0.61	0.51	172.0
GRAS	6.921	43.754	-0.13	0.18	0.18	0.18	-0.28	0.29	0.18	0.17	138.7
HERS	0.336	50.867	0.37	0.25	-0.23	0.25	1.35	0.32	0.25	0.25	151.7
IENG	7.639	45.015	0.31	1.16	-0.83	1.16	2.04	3.89	1.16	1.16	55.9
KOSG	5.810	52.178	-0.10	0.16	0.20	0.15	1.61	0.28	0.16	0.15	112.3
LROC	-1.219	46.158	0.13	0.49	-0.11	0.58	1.31	1.82	0.58	0.49	179.2
MDVO	37.224	56.027	-0.11	0.26	0.45	0.32	2.41	0.91	0.32	0.26	170.5
MOBN	36.570	55.115	-0.02	0.43	-0.68	0.58	1.28	1.69	0.58	0.43	171.1
NPLD	-0.340	51.421	0.31	0.33	-0.49	0.43	1.68	1.38	0.43	0.33	179.6
NVSK	83.235	54.840	-1.22	0.97	-0.15	1.02	7.96	2.83	1.02	0.97	171.1
OBER	11.280	48.086	0.12	0.28	-0.05	0.24	1.06	0.79	0.28	0.24	95.9
OPMT	2.335	48.835	-0.40	0.79	-0.75	0.99	1.06	3.35	0.99	0.79	177.5
PTBB	10.460	52.296	0.30	0.57	-0.40	0.69	1.56	2.39	0.69	0.57	174.5
REDU	5.145	50.001	0.47	0.93	-1.01	0.84	3.93	3.98	0.93	0.84	92.6
SJDV	4.677	45.879	0.23	0.47	-0.61	0.63	1.55	2.55	0.63	0.47	-179.6
UZHL	22.298	48.631	-0.29	0.56	-0.62	0.71	-0.07	2.34	0.71	0.56	175.4
WROC	17.062	51.113	-0.05	0.98	-0.25	1.08	3.76	3.60	1.09	0.97	164.8
WSRT	6.605	52.914	-0.16	0.15	0.06	0.15	0.60	0.29	0.16	0.14	120.4
WTZR	12.879	49.144	0.14	0.15	-0.08	0.14	1.51	0.23	0.15	0.14	129.3
YEBE	-3.089	40.524	-0.35	0.42	0.04	0.42	3.37	1.42	0.43	0.42	127.4
ZIMM	7.465	46.877	0.09	0.17	-0.09	0.17	2.32	0.42	0.18	0.16	140.5
AFRI											
GOUG	-9.881	-40.348	-0.20	0.62	0.69	0.56	-10.48	1.81	0.62	0.56	101.8
HRAO	27.687	-25.889	0.50	0.42	-0.07	0.37	-0.85	0.78	0.42	0.37	96.4
LPAL	-17.894	28.763	0.81	1.43	-0.48	1.54	2.63	6.11	1.55	1.42	-163.0
MAS1	-15.633	27.763	0.14	0.37	-0.04	0.33	0.93	0.62	0.38	0.33	-100.0
NKLG	9.672	0.354	-0.86	0.53	-0.12	0.42	-1.34	1.23	0.53	0.41	97.2
RABT	-6.854	33.997	0.32	0.61	-0.90	0.54	0.07	1.65	0.61	0.54	79.3
RBAY	32.078	-28.795	0.13	0.77	-0.09	0.65	-0.01	2.55	0.77	0.65	89.4
SIMO	18.440	-34.187	-1.52	1.70	-0.08	1.61	-13.49	6.02	1.70	1.61	92.7
SUTH	20.811	-32.379	-0.29	0.48	0.60	0.42	1.73	1.04	0.48	0.42	93.0
ZAMB	28.311	-15.425	-0.85	1.47	0.45	1.16	1.50	4.93	1.47	1.16	87.5

Table 4.7: Adriatic plate relative angular velocities and errors at 68% probability level

Plate	Lon	Lat	smax	smin	Azi	Ω	± Ω
	º	º	º	º	º	º/Myr	º/Myr
relative to Eurasia							
AD1	7.65	45.29	1.0	0.4	90	0.216	0.023
AD2	8.57	45.45	1.5	0.4	95	0.327	0.103
relative to deep hotspots							
AD1	57.62	44.94	36.9	18.7	88	0.111	0.037
relative to shallow hotspots							
AD1	136.79	-52.73	21.3	10.1	94	0.791	0.095

Table 4.8: Sites selected to estimate the Adriatic rotation poles: coordinates in degree, residual velocities and error ellipsis axes in mm/yr, azimuth of the semi-major axis in degree.

SITE	Lon	Lat	E	±E	N	±N	Up	±Up	s_{maj}	s_{min}	Az
AD1 (*blind selection*)											
BRAS	11.113	44.122	-0.04	0.35	0.16	0.40	1.25	0.26	0.40	0.35	172.2
CHTL	6.359	45.304	-0.18	0.29	0.11	0.34	3.03	1.24	0.34	0.29	179.1
GSR1	14.544	46.048	0.05	0.52	-0.22	0.57	0.77	0.43	0.63	0.45	143.9
MDEA	13.436	45.925	-0.21	0.27	0.26	0.40	0.56	0.66	0.41	0.26	166.7
MODA	6.710	45.214	0.22	0.26	0.24	0.31	1.95	1.12	0.31	0.26	172.9
NOVA	8.614	45.447	0.10	0.24	-0.04	0.48	1.82	0.37	0.48	0.24	181.0
PADO	11.896	45.411	0.17	0.27	-0.62	0.56	1.55	0.25	0.56	0.27	180.0
PATK	11.460	47.208	-0.50	0.54	0.07	0.38	0.31	1.54	0.54	0.38	89.8
ROVI	11.783	45.087	0.29	0.52	0.42	0.46	-0.59	0.73	0.53	0.46	82.8
SBPO	10.920	45.051	-0.13	0.75	0.29	0.86	0.68	0.73	0.86	0.75	175.3
TORI	7.661	45.063	0.06	0.29	-0.04	0.69	1.12	0.35	0.69	0.29	174.5
TREN	11.122	46.072	0.07	0.30	0.01	0.28	-1.39	0.39	0.30	0.28	81.3
VENE	12.332	45.437	-0.26	0.30	0.14	0.44	-0.26	0.22	0.44	0.30	179.1
AD2 (*sites located on the undeformed Adriatic microplate*)											
CAVA	12.583	45.479	-0.08	0.30	0.53	0.50	-0.32	0.50	0.50	0.30	173.8
PADO	11.896	45.411	0.06	0.29	-0.85	0.66	1.55	0.25	0.66	0.29	178.9
PAVI	9.136	45.203	0.66	0.33	-0.14	0.63	-0.49	0.49	0.64	0.32	173.8
PRMI	9.202	45.463	0.03	0.25	0.30	0.84	-1.40	0.59	0.84	0.25	182.1
ROVI	11.783	45.087	0.11	0.57	0.21	0.52	-0.59	0.73	0.58	0.51	64.3
SBPO	10.920	45.051	-0.32	0.83	0.21	0.93	0.68	0.73	0.93	0.82	167.4
TEOL	11.677	45.343	-0.11	0.31	0.13	0.55	0.91	0.36	0.55	0.31	180.2
VENE	12.332	45.437	-0.37	0.33	-0.15	0.56	-0.26	0.22	0.56	0.33	176.6

5 Can Earth's rotation drive plate tectonics?

5.1 Introduction

In the previous chapters we have seen that it is possible to give a kinematic representation alternative to current models of plate motion introducing an analytical form for the westward drift of the lithosphere.

The formulation of the model is based on two fundamental assumptions: the velocity of the reference plate (PA) with respect to the mantle may double its standard value, thus considering indirectly a shallower hotspot source; the lithosphere and the asthenosphere are decoupled at their interface by the presence of a heterogeneous low viscosity layer.

Following our model, plate motion occurs as an ordered undulated flow along which all the plates move at different velocities having a west-directed component. Then, the net-rotation of the lithosphere emerges as a process at global scale that cannot be easily interpreted as simply due to a balance of forces internal to the solid Earth. On the other hand, if we consider all the possible mechanisms generated within the Earth, none is able to account for a westward drift of the lithosphere.

The supply of energy for plate tectonics and the basic mechanisms that move the tectonic plates are far to bee entirely understood. A number of papers tried to provide evidence for a system driven only by lateral density heterogeneities controlled by the thermal cooling of the Earth, particularly with the cool slab pulling the attached plates (e.g., Conrad and Lithgow-Bertelloni, 2003). However, a number of issues contradict a simple thermal model capable to generate the Earth's geodynamics (Anderson, 1989). Moreover, the geological and geophysical asymmetries of rift and subduction zones as a function of their polarity (e.g., Doglioni et al., 2007), suggest that plate tectonics is also controlled by an astronomical mechanical shear adding to the thermal cooling fuel (Scoppola et al., 2006).

The interest in Earth's rotation as driving plate tectonics goes back to the theory of Wegener and a number of papers in the early seventies (e.g. Bostrom, 1971; Knopoff and Leeds, 1972). This relation is based on the observation that plates have, for example, a westerly directed polarization

relative to Antarctica (Le Pichon, 1968) or relative to the hotspot reference frame (Ricard et al., 1991; Gripp and Gordon, 2002). This fundamental issue has been basically abandoned after few papers formulated the hypothesis that the viscosity of the asthenosphere is too high in order to allow a complete decoupling of the overlying lithosphere (Jordan, 1974). However new evidences suggest the presence of a ultra-low seismic velocity at the top of the asthenosphere (Rychert et al., 2005), which might correspond to the presence of a layer with much lower viscosity than so far expected in the low-velocity layer (Aoudia et al., 2007), as introduced in Chapter 1.

This chapter does not have the role to give answers, or numerical models of plate dynamics, but to formulate hypothesis and, on the basis of results previously presented, to find experimental evidences in support of our hypothesis.

5.2 Classical models of plate motion driving forces

The question about the forces that drive plates has been the subject of intense debate ever since the plate tectonic theory was first accepted by the geologic community in the late 1960's. The major concern is whether mantle convection and the activity of mantle plumes dominate the driving forces of plate motion, or whether surface boundary and plate forces, such as slab pull and ridge push provide the most important forces. The argument is basically whether the plates are passively riding along on the top of a mantle convection cell, or whether the plates themselves are active drivers, dragging along with them the mantle below.

In plate tectonics it is assumed that the inertia and acceleration of the individual plates are nonexistent or negligible, and thus the plates are in dynamic equilibrium. Therefore the sum of the torques acting on a plate must be zero (Forsyth and Uyeda, 1975). This assumption seems reasonable enough, in fact plate motion estimated by space geodetic observations are steady at least from the last few million years, and the internal rigidity of plates can be considered a good approximation at large scale (Chapter 1).

A number of forces have been postulated since the dawn of the tectonic theory, mainly including ridge push, slab pull, trench suction, collisional resistance and basal drag (Richardson, 1992; Weil, 1996). In the past ten years, many scientists have begun to assume that the boundary and body forces of the plates, rather than the frictional drag produced by mantle convection, are the most dominant group of forces driving plate motions (Figure 5.1).

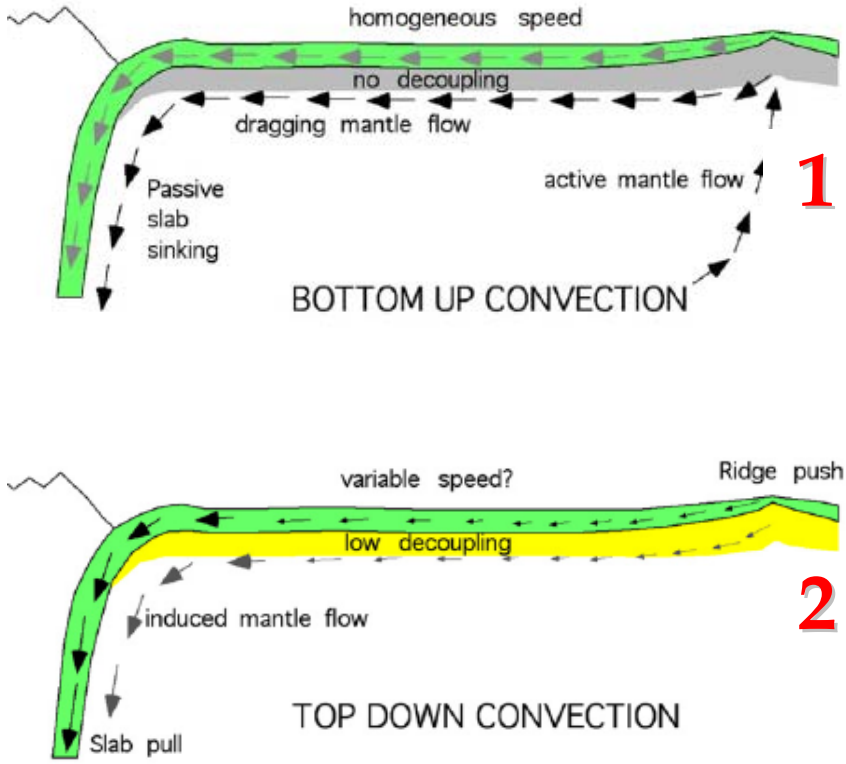

Figure 5.1: Two classical models of plate motion driving mechanisms: 1) mantle convection heated from below, the bottom up convection with a passive role of plates; 2) boundary forces producing top down convection, with an active role of plates (from Doglioni et al., 2007).

The main forces acting on the lithosphere are subdivided into coupled and uncoupled forces with respect to the mantle (Carlson et al., 1983a, b; Jurdy and Stefanick, 1988). Mantle drag need high coupling (high viscosity) between the lithosphere and the asthenosphere to be effective (e.g., Bercovici, 1998; Conrad and Lithgow-Bertelloni, 2003). On the contrary, the ridge push, the slab pull and the tidal drag should need low coupling (low viscosity) to be efficient.

The ridge push has been considered in two different manners, as a body force and as a boundary force. As a body force, ridge push has been attributed to the cooling and thickening of the oceanic lithosphere with age

(McKenzie, 1968; McKenzie, 1969; Richardson, 1992; Vigny et al., 1991). This type of force can be thought of as created by the horizontal pressure gradient attributable to the cooling and thickening of the oceanic lithosphere and calculated as this force integrated over the area of the oceanic portion of a given plate (Lister, 1975). The alternative, ridge push as a boundary force, is caused by the "gravity wedging" effect (Bott, 1993). This effect results from warm, buoyant mantle upwelling beneath the ridge crest which causes a topography-induced horizontal pressure gradient. Here the force would be acting as a boundary force at the edge of the lithospheric plate, proportional to the length of the ridge, and not as a body force over the entire oceanic portion of the plate.

The slab pull forces are derived from the negative buoyancy of the cold subducting lithosphere and are dependent on the angle, temperature, age and volume of the subducting slab, as well as the length of the respective trench (Chapple and Tullis, 1977). Slab pull is considered a boundary force, and from most estimates is responsible for some of the largest forces, or torques in the driving system (Wilson, 1993). Several empirical studies have shown a strong correlation between plate velocities and age of subducting oceanic lithosphere for plates with long subduction boundaries (Forsyth and Uyeda, 1975; Chapple and Tullis 1977). This might suggest that slab pull is the dominant acting force, estimated of about $3 \cdot 10^{13}$ $N \cdot m^{-1}$ (Turcotte and Schubert, 1982). However, there are several moving plates that have little or no portion of subducting boundaries; therefore it is important to look for other contributing forces.

The resistive forces are exerted on the overriding plate in a subduction zone at the contact with the descending slab. This force is thought to result in a shear stress that is distributed over the subduction thrust interface, that dips in the direction of the plate's interior (Wilson, 1993). However, tectonic resistive forces are considered equal and opposite in sign to the force exerted on the subducting plate, and therefore do not contribute greatly to the net driving force for plate motion (Meijer and Wortel, 1992).

Another force generally considered is the trench suction observed in the overriding plate at subduction zones as a net trench-ward pull, many times resulting in back arc extension (Forsyth and Uyeda, 1975; Chase, 1978). Trench Suction is thought to result from small-scale convection in the mantle wedge, driven by the subducting lithosphere. This force is difficult to isolate from other forces because of the little knowledge about mantle convection in the shallow subsurface (Ziegler, 1993). Related to trench suction is slab roll-back caused by the small-scale convection current on the back-side of

subducting slabs. This current produces a pull away from the trench, consequently rolling back the hinge of the subducting slab. This phenomenon is observed today in the Adriatic plate, along the Appenines (Devoti et al., 2008) and in Hellenic Arc of Greece.

The last major force, basal shear traction or basal drag is important because of its relevance to the fundamental question of whether plate motions are active or passive. Basal shear traction is the resistance or dragging force associated with the interface between the upper mantle and the lithosphere. Today this force is thought to be small, but until we know more about the coupling between the lithosphere and the mantle is better constrained, we cannot be certain how important it is. It is thought to have a small magnitude per unit area, but when spread over the entire under-surface of big plates can result in a large cumulative resistance.

The lack of good correlation between plate velocity and surface area has traditionally been used to argue against basal shear traction as an important driving force. In recent models researchers have considered the basal shear traction a passive force, either driving or resisting plate motion, but not dominating plate motion (Richardson, 1992).

Other researchers consider drag forces playing an important role in driving plate motion, while the plates remain passive (Vlaar and Wortel, 1976; Jacoby et al., 1980). In this case the lateral motion of the plates would be caused by the mantle's exertion of a drag force on the overriding lithosphere, above warm upwellings. Here, the shear traction is estimated to be small per unit area and would be proportional to the horizontal, or toroidal, component of the upper-mantle's flow velocity relative to the overlying plate velocity (Ziegler, 1993). But it is important to point out that the mechanics of upper-mantle flow are poorly constrained at this time.

There are several evidences that cast doubts about each single mechanism in driving plate motion. The mantle drag hypothesis is contrasting with volcanologic (the hotspots) and seismologic evidences (the LVZ layer) that claim for a low coupling between the asthenosphere and the mantle.

The slab pull hypothesis is based on the assumption that only plates with a subducting margin can move, being the velocity of plate proportional to the length of this margin. However, there are plates moving without subducting slabs and modelling showing contradictions in the early stage of subduction initiation (Cloetingh et al., 1982); moreover the mean value of the extensional strength (integrated along the lithosphere thickness) has been evaluated on average as $8 \cdot 10^{12}$ $N \cdot m^{-1}$ (Stuwe, 2002), possibly exceeding the mean value estimated for the slab pull traction. The slab pull has a number of further

counterarguments, such as it is inferred on the assumption that the slab is heavier than the country mantle, but several uncertainties remain on the composition of both bodies at variable depth; if the pull of the slab would induce plate motion, we would expect tensional strength along the slab, on the contrary, seismological studies show that down–dip compression affects most of the slabs, all below 300 km (Isacks and Molnar, 1971), some of them even at shallower depth (e.g., Frepoli et al., 1996).

Then, excluding all the driving forces based on a strong coupling between the lithosphere and the asthenosphere; the remaining, the ridge push and the slab pull are not able to account for all the peculiarities connected with plate tectonics in a unified, ordered view as requested by the model of west-ward drift of lithosphere (Doglioni et al., 2007; Crespi et al., 2007).
In our opinion, the two most compelling candidates acting at global scale are the Earth's rotation and the tidal drag. If plate kinematics is regulated by a combined action of the forces connected with these two processes, a signature should be evidenced in global tectonic processes too.
In this chapter we want to analyze some experimental evidences linking tectonics to the Earth's rotation and tidal drag.

5.3 The variable rotation vector of the Earth

The variability of the Earth's rotation vector relative to the body of the planet or in inertial space is caused by the gravitational torque exerted by the Moon, Sun and planets, displacements of matter in different parts of the planet and other excitation mechanisms. The observed oscillations can be interpreted in terms of mantle elasticity, Earth flattening, structure and properties of the core-mantle boundary, rheology of the core, underground water, oceanic variability, and atmospheric variability on time scales of weather or climate (Lambeck, 1980).

Let us choose $\hat{x}$, $\hat{y}$ and $\hat{z}$ as a terrestrial system of reference, the ITRF. The $\hat{z}$ axis is oriented along the Earth's mean rotation axis, the $\hat{x}$ axis is in the direction of the adopted origin of longitude and the $\hat{y}$ axis is orthogonal to $\hat{x}$ and $\hat{z}$ axes and in the plane of the 90° E meridian. The angular rotation of the Earth may be written as $\vec{\Omega} = \Omega_0 \cdot (m_x \cdot \hat{x} + m_y \cdot \hat{y} + (1 + m_z) \cdot \hat{z})$, or in matrix form

$$\vec{\Omega} = \Omega_0 \cdot \begin{pmatrix} 0 \\ 0 \\ 1 \end{pmatrix} + \Omega_0 \cdot \begin{pmatrix} m_x \\ m_y \\ m \end{pmatrix}$$

Where the second term may be interpreted as a perturbation of the mean conventional rotation vector of the Earth (first term), where Ω_0 is the mean angular velocity, m_x m_y are the orientation variation of the instantaneous pole with respect to the conventional pole in the terrestrial frame, and m_z is the fractional variation in the rotation rate.

Then, the polar motion is represented by a series of instantaneous coordinates x, y of the instantaneous rotation pole with respect to a reference pole $\bar{x}_p$, $\bar{y}_p$ (McCarthy and Petit, 2004). The relation between m_x, m_y and the coordinates is $m_x = (x - \bar{x}_p)$ and $m_y = -(y - \bar{y}_p)$. The units are given in milliarcseconds (1mas =4.8481· 10^{-9} rad and an arc of 1mas from the center of the Earth at distance equal to the polar radius is 1mas=3.1cm).

The difference between the astronomically determined duration of the day and the mean solar day, defined as T_0 =86400 s, is called length of day (LOD) although it really represents the excess of length of day.

The relationship between the Earth's angular velocity Ω and LOD is

$$\Omega = \Omega_0 \cdot (1 - \frac{LOD}{T_0}) = \Omega_0 \cdot (1 + m_z) = \Omega_0 - \frac{\Omega_0}{T_0} \cdot LOD$$

where the nominal value of the Earth's angular velocity is
Ω_0 = 72921151.467064 picorad/s and T_0 =86400 s
then we have

$$m_z = -\frac{LOD}{T_0} \text{ and}$$

$$\Omega = \Omega_0 - 0.843994809 \cdot LOD$$

where Ω is in picoradians/s and LOD in milliseconds.

As obvious, the relations show that LOD and Ω have opposite sign, if LOD increase Ω decrease and vice versa (Figure 5.2).

We have seen that the Earth experiences periods with faster spin rates and periods with slower spin rates with respect to the reference mean spin rate Ω_0. Accordingly, the polhody, i.e. the trace of polar motion on the Earth's surface, is larger when the Earth spins slower and vice versa.

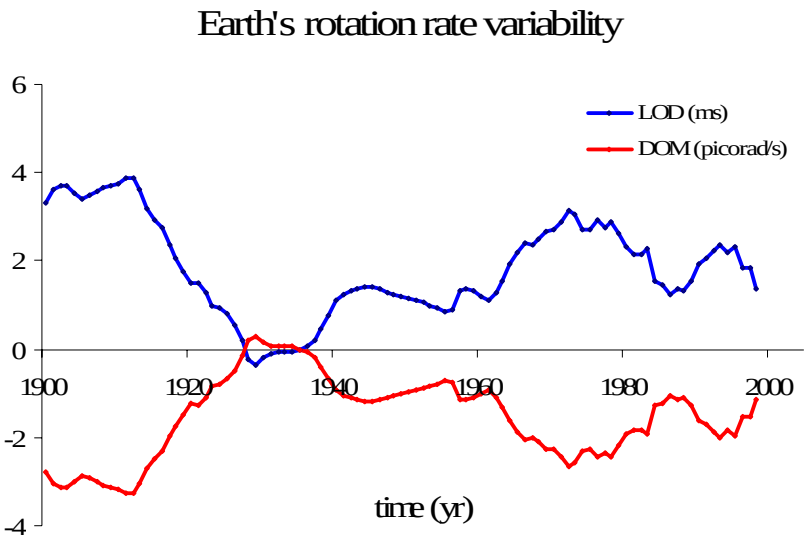

Figure 5.2: Time series of averaged yearly LOD and variations of Ω; the specular trend testifies the opposite sign between the two time series. Data from IERS: series JPL and combined C04.

The solid Earth tides are deformations of the Earth caused mainly by the attraction of the Sun and Moon (Melchior, 1983) that induce limited variations of the Earth's rotation vector. The tidal phenomenon implies a change of the tensor of inertia; these tidal effects are associated with solid Earth deformations which in turn, induce Earth rotation variations with amplitude as large as 0.001s and period ranging from a few days to the secular slowing-down of the Earth rotation (Paquet et al., 1997). The diurnal and semi-diurnal tides (sectorial and tesseral) are not able to excite the Earth's rotation vector, due to their symmetry. The largest tidally induced LOD fluctuations are due to the fortnightly zonal tides, with amplitudes within 1ms; minor effects are due to monthly, semi-annual, and annual zonal tides (Dickey, 1995; Paquet et al., 1997).

The tides, being generated by the Sun and the Moon, have period known with high precision but the amplitudes and the phases are depending on the rheological properties of the Earth and thus have to be measured. The mantle inelasticity amplifies the tides and introduces a delay in the Earth response. In particular the secular slowing down of the Earth rotation is mainly the consequence of a permanent phase lag in the deformation of the inelastic

equatorial bulge due to the Moon attraction; its amplitude is estimated at 1.7ms per century (0.017ms/yr) (IERS-EOP web site). The inelastic rheological parameters are presently not yet well determined from the theoretical point of view; thus Earth rotation observations provide complementary information to that obtained by seismology, nutation data, tidal records and satellite geodesy.

The Earth spin has a variable rate now and in the past. The duration of day was about 19 hours 2.5 Ga ago, 21 hours 0.5 Ga ago, and it is increasing during the last 500 Ma at a rate of about 1.79 ms/century (Denis et al., 2002). This deceleration of the Earth is, for the most part, compensated by the enlarging of the Moon orbit of 38.2±0.7mm/yr (Dickey et al., 1994) in order to maintain the angular momentum of the system.

Actually, the long term variations of the Earth's angular velocity are mainly due to two different components with opposite effects: the tidal dissipation and the decrease of Earth oblateness, respectively acting to slow and to increase the Earth's angular velocity. The latter is commonly explained by the effects of the action of the tidal brake and the last ice age (Wahr, 1988); the postglacial rebound induces a net transfer of material within the Earth toward higher northern latitudes, decreasing the Earth's moment of inertia and thereby decreasing LOD. What really happens to the Earth is that it slowly tends to become less oblate (due to the secular deceleration) and at the same time its oblateness is oscillating at different frequencies, due to a variety of excitation factors. Consequently, there are shorter time scale variations of the LOD with wavelength of decades, or even seasonal and higher frequency oscillations (e.g., Kane and Trivedi, 1990; Dickey, 1995; Paquet et al., 1997; Schuh et al., 2001). Marcus et al. (1998) have shown how oceanic circulation pattern can for example generate LOD variations on seasonal and shorter time scales. Periodic LOD fluctuations, typically on annual and semi-annual time scales, have been inferred as excited by global atmospheric circulation (Chao, 1989). Other variations on decade time scales of the LOD have been attributed to climate factors (Klyashtorin, 2001; Varga et al., 2005), solar activity (Georgieva, 2002; Chapanov, 2006) and exchanges of angular momentum between the core and the mantle (e.g., Jault et al., 1988; Jault and Le Mouel, 1990).

Variations in either the rate of rotation or in the geocentric direction of the rotation axis (i.e., polar motion) will perturb the centrifugal force and so will deform the Earth, affecting observed station coordinates and surface gravity measurements depending from latitude.

The centrifugal potential is composed by a constant, a linear and quadratic terms in m_i; the first is the bulge, the second in spherical coordinates is

$$V(\theta,\lambda) = \frac{1}{2}\Omega_0^2 R^2 (\sin 2\theta \cdot (m_x \cdot \cos\lambda + m_y \cdot \sin\lambda) + 2m_z \cdot \sin^2\theta)$$

where R is the geocentric distance of the site. Following Gipson and Ma (1998), the radial displacement due to variations of Earth's rotation is

$$\Delta R = \frac{h}{g} \cdot V(\theta,\lambda,m) \cong -h \cdot (53\sin 2\theta \cdot (m_x \cdot \cos\lambda + m_y \cdot \sin\lambda) + 0.25 \cdot m_z \cdot \sin^2\theta)$$

where the nominal value of Ω_0, R and g have been introduced, h~0.6 is the vertical Love number, ΔR is in mm if m_x, m_y are in arc seconds and m_z in ms/day. The maximum variation of the first two terms occurs at 45° of latitude with peak amplitude of about 15 mm, whereas the peak-to-peak displacement due to m_z occurs at the equator and may reach maximum 0.6 mm. The East displacement is

$$\Delta E \cong 106 \cdot l \cdot \cos\theta \cdot (m_x \cdot \sin\lambda - m_y \cdot \cos\lambda)$$

and the North is

$$\Delta N \cong l \cdot (106 \cdot \cos 2\theta \cdot (m_x \cdot \cos\lambda + m_y \cdot \sin\lambda) + 0.25 \cdot m_z \cdot \sin 2\theta)$$

where $l \sim 0.085$ is the horizontal Love number. We can note that the rotation rate (m_z) does not affect the east component and is practically negligible in the north component, since the horizontal are about ¼ than the vertical deformations.

The secular deceleration of the Earth's rotation is able to produce stresses on the lithosphere that depend on latitude. The differential stress

$$\tau(a) = \sigma_{\theta\theta}(a) - \sigma_{\lambda\lambda}(a)$$

(a is the equatorial radius, θ the co-latitude and λ the longitude) is a good indicator of the tectonic feature of lithosphere. According to the model of Almavict and Legros (1991) the temporal dependence $\tau(a)$ of the differential stress may be approximated as

$$\tau(a) \approx 1.22 \cdot 10^5 \cdot t \cdot \sin^2\theta \quad (t \text{ in Myr})$$

thus implying, for instance, that during 100 Myr, the accumulated differential stress may be larger than 120 bars. This value exceeds the accepted mean value of the mechanical strength of continental lithosphere. According to the Brace-Goetze diagrams, the mean value of the extensional strength (integrated along the lithosphere thickness) is about 10^{12} N·m^{-1}, corresponding to specific stress of 10 MPa or 100 bars (Stuwe, 2002). Thus, the secular deceleration has to be considered a significant source of tectonic stress accumulating over geological times, studied as the origin of the break-up of

lithospheric plates or planet crust (Melosh, 1977) and possibly with a shorter time-scale role.
Deglaciation and plate motion contribute to modify the Earth's figure and therefore to activate polar wandering (TPW); Almavict and Legros (1991) estimated with a simplified model that this effect produce stresses in the lithosphere of about 40 bars for each degree of TPW.

The solid tide stresses induce only up to 5×10^3 Pa (0.05 bar), whereas in ocean basins, water loading builds stresses up to nearly 5×10^4 Pa (0.5 bar) (Cochran et al., 2004). This stress change is much smaller than the typical stress drop of earthquakes, but its rate is generally larger than that of tectonic stress accumulation. Therefore the tidal stress could trigger an earthquake when the stress in the focal region is close to the critical level to release an earthquake (Tanaka et al., 2004).

5.4 Evidence of latitude-depending seismicity

The global distribution of seismic events is not random, but mainly follows plate margins and deformation areas (Figure 1.3, Chapter 1). However, within the spatial pattern defined by the plate interactions, we want to analyze if it is possible to identify other global patterns. To this aim, we have analyzed the global distribution of seismic events for magnitudes $M \geq 7.0$, which release about 90% of the elastic energy of plate tectonics, considering a global seismic catalog covering the largest time span, satisfying the requirement of completeness.

The Centennial Catalog is a global catalog of locations and magnitudes of instrumentally recorded earthquakes (Engdahl and Villaseñor, 2002). This is a catalog of large earthquakes, created with the purpose of giving a realistic picture of the seismicity distribution in the Earth. It has been assembled by combining existing catalogs, reducing all available magnitudes for each earthquake to a common, corrected magnitude and relocating the earthquakes with available arrival time data. It extends from 1900 to April 2002 and its completeness is practically ensured for magnitudes $M_w \geq 7.0$. To expand the time span, we have added all the events with $M_w \geq 7.0$ from the USGS/NEIC global catalog. The updated dataset consists of 1719 events with $M \geq 7.0$, from 1900 to September 2007.
The distribution of the number of events per latitude classes shows that (Figure 5.3) polar region are not affected by seismic activity, the maximum number of events is in the class $-10 < \text{Lat} \leq 0$ N, 65% of the events falls in the

class -30< Lat ≤+30 N and that 28% of the events occurs at the middle latitudes of the northern hemisphere.
The normalized energy computed by the classical relationship (Kanamori, 1977) shows that more than 70% of the elastic energy is radiated in the range -30°< Lat ≤30° N (Figure 5.3), the same range of the *tectonic mainstream*, the ideal line along which the net rotation velocity of lithosphere with respect to the mantle is maximum (Chapter 3).
All these patterns support a rotational and astronomical tuning of plate tectonics: at low latitudes, plates tend to move faster, transform faults are longer, seismic activity is globally higher, etc.

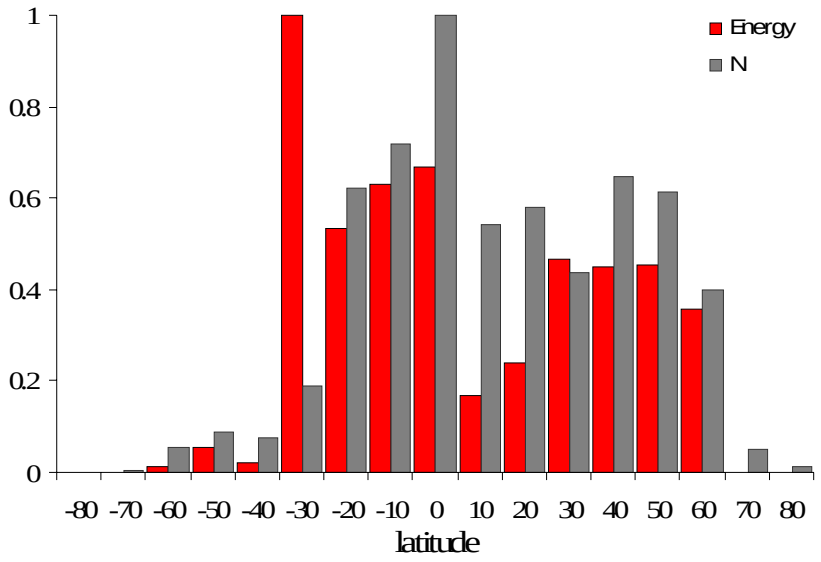

Figure 5.3: Distribution of normalized N and E grouped in 10° latitude intervals, from the Global catalog of earthquakes with $M_w \geq 7.0$ (1900-2007) - MGE7 global. The outstanding energy release of the Chile earthquake (1960, $M_w=9.5$) is well visible. Polar regions are silent whereas the seismic activity is maximum at low latitudes.

5.5 LOD and seimicity time series

Varga et al. (2005) have shown the existence of a relationship between the event occurrence per year (N) and LOD time series, as LOD increases, N is

higher and vice versa. Similar relation exists between the energy released globally by large events per year and LOD.

We started from this evidence, to make here a deeper analysis by analyzing the time series of LOD, detrended from secular drift, N and $\log_{10}$E considering a time span of more than a century (1900-2007).

The LOD time series is composed by the yearly averaged series of JPL (1832-1997) completed with the combined C04 solutions up to 2007, provided by the IERS (Bizouard and Gambis, 2008). The LOD series selected in our analysis overlaps the seismicity time span (from 1900-2007) and has been detrended from secular drift.

The N time series consists of the yearly number of events occurred from 1900 to September 2007, the $\log_{10}$E time series is the $\log_{10}$ of the global seismic energy yearly released. Since we are interested to identify long periods, the two time series are smoothed with a 5 yr moving average (a low-pass filter). To make an effective comparison, the two time series have been normalized. The normalization of a series $y(t)$ is made classically by defining

$$y_{norm}(t) = \frac{y(t) - y_{\min}}{y_{\max} - y_{\min}}$$

where y_{max} and y_{min} are respectively the maximum and minimum values assumed by y.

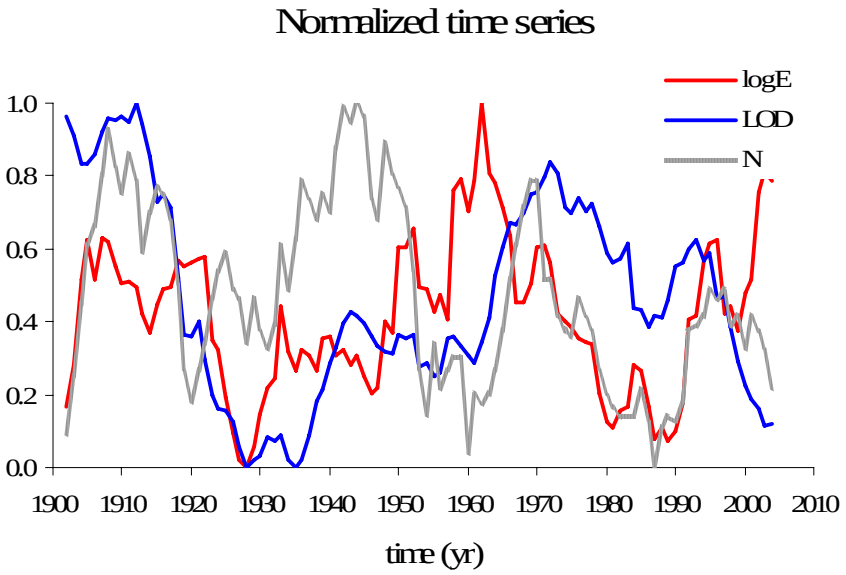

Figure 5.4: Normalized time series of LOD, N, number of earthquakes (M≥7.0), and $\log_{10}$E.

Figure 5.4 shows the LOD, $\log_{10}E$ and N time series after the normalization. The search for non-random processes in the normalized time series of LOD, $\log_{10}E$ and N is performed firstly by the Lomb normalized periodogram (Press et al., 1992).

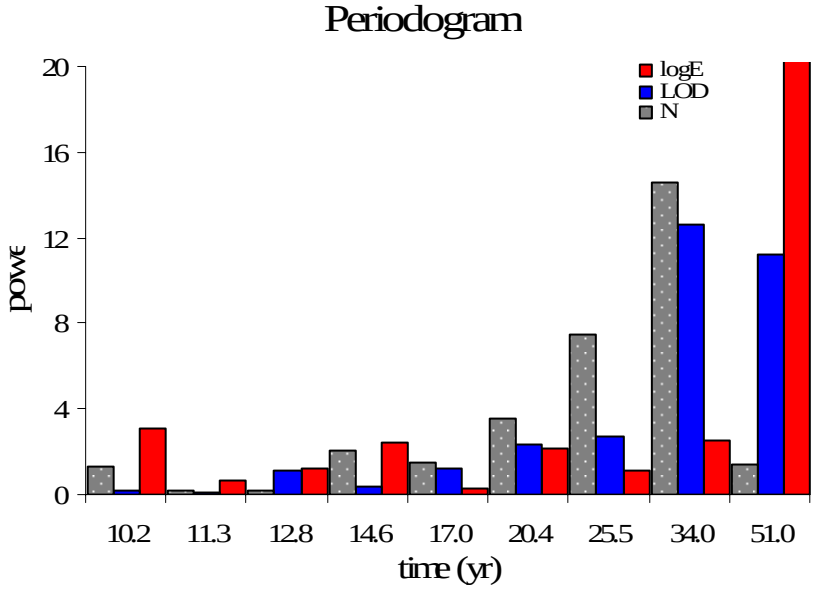

Figure 5.5: Periodograms of LOD, seismicity (N) and $\log_{10}E$.

LOD and N have significant peaks centered at 34 yr, corresponding respectively to normalized powers of 12.6 and 14.6, well beyond the value of 7.6, limit of the 95% level. The LOD and $\log_{10}E$ time series have significant periods at 51 yr, corresponding to normalized powers of 11.2 and 27.5 respectively. It is worth noting that the temporal interval covered by the two time series are rather limited (102yr), so that the detection of long periodicities is affected by a low resolution. In fact the frequency resolution of a spectral analysis is defined as the inverse of the temporal length of the sequences, i.e.

$$f_s = \frac{1}{\Delta T}$$

f_s represents the minimum frequency step of the time series analysis.

In our case $\Delta T = 102 yr$, then $f_s = 0.0098 yr^{-1}$. We have seen that the highest peak is detected at a period of 34yr, equivalent to the frequency of $f = 0.0294 yr^{-1}$; then, the nearest peaks that could be really detected correspond to the frequency interval $f = 0.0294 \pm 0.0098 yr^{-1}$ equivalent to the time interval of 25.5 - 51.0 *yr*. Therefore, we can conclude that the peaks identified in LOD, $\log_{10}$E and N are effectively significant but the time series are too short to detect with good resolution the real value of these periodicities (Figure 5.5).

After, we have analyzed the cross-correlation between the sequences with an efficient FFT-based algorithm in the frequency domain. The procedure is equivalent to convolution with one of the two sequences reversed in time (Orfanidis, 1996). At time lag 0, the cross correlation between LOD and N is 0.79, whereas between LOD and $\log_{10}$E is 0.81, both significant at 95% confidence level (Figure 5.6).

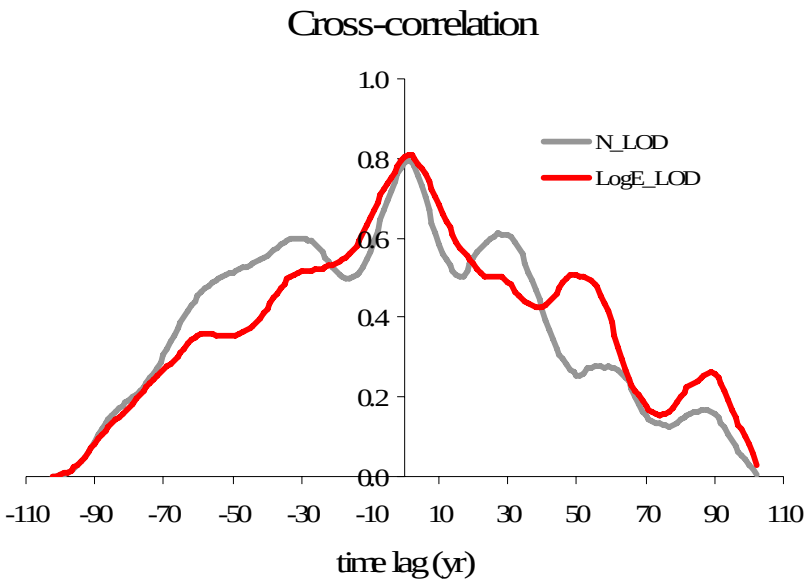

Figure 5.6: Cross-correlation between LOD and N; the line of the 95% significance level (in red) shows that the time lag between the two series is insignificant.

The magnitude squared coherence estimate is a positive normalized function of frequency and indicates how well one series corresponds to the other at each frequency. The magnitude squared coherence of LOD and N starts saturation till about 0.65 after about 20 yr; a higher level of coherence at low frequency is obtained between LOD and $\log_{10}$E, though they reach the asymptotical value of 0.78 after about 30 yr (Figure 5.7).

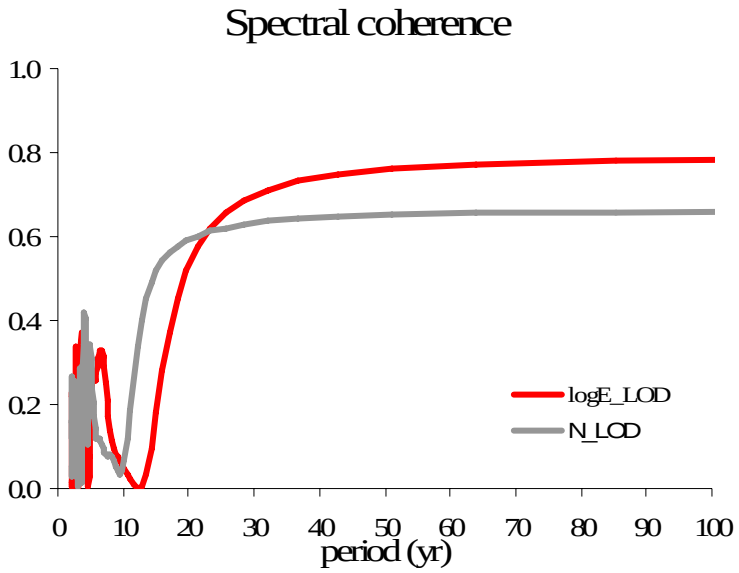

Figure 5.7: Magnitude squared coherence between LOD, N and LOD, $\log_{10}$E. The latter are more coherent at long periods than the first two. The saturation value (0.65) is reached after 20 yr, the second (0.78) after 30 yr.

It has been shown that seismicity is not able to significantly modify the LOD: the large M=9.3 Sumatra 2004 earthquake generated a LOD variation of few microseconds, within the level of observational error (Chao and Gross, 2005). Therefore the seismicity cannot be responsible of the larger and long-term LOD oscillations, and we argue that the process responsible for the LOD oscillation is the same as the one controlling the seismicity variation.

Wang et al. (2000) have demonstrated a correlation between mounting stress and increase of the LOD along faults in China. The correlation appears

most typically on decade time scales and seems to be direction-dependent. However, it is easy to show that Earth's rotation variations alone induce minute deformations that depend from latitude.

5.6 Solid Earth's energy budget and the plate tectonics expenditure

In plate tectonics it is assumed that the acceleration of the individual plates are nonexistent or negligible, and thus the plates are in dynamic equilibrium. Therefore the sum of the torques acting on a plate must be zero (Forsyth and Uyeda, 1975).

At present, the solid Earth can be considered in energetic equilibrium: the energy sources that keep running its dynamical processes and the most significant phenomena that are the consumers of terrestrial energy resources are equivalent in magnitude (Appendix 1). Thus it is natural to assume that the balance is in quasi equilibrium, i.e. there is no statistically meaningful difference between the total of energy rate income and energy rate expenditure. This circumstance allows for relatively small energy sources to influence global tectonic processes. Thus, the tidal despinning can influence the plate tectonic process through the westward mantle flow process (Bostrom, 1971; 2000; Knopoff and Leeds, 1972). Small perturbations in the velocity of rotation trigger the release of a large amount of energy and seismicity (Press and Briggs, 1975).

The energy rate necessary to move the Earth's shields, i.e. to move the thicker lithosphere relative to the underlying poorly developed low velocity channel (as in the Baltic area), has been estimated at about 4 10^{18} J/yr (Knopoff, 1972). Similar value is found by considering the energy of formation of tectonic dislocations that can be estimated as the consumers of energy rate $\dot{E}$ necessary for lateral displacement of the lithosphere plates relative to the viscose mantle. Thus, it can be written as in Maslov (1991):

$$\dot{E} = \chi \cdot \omega^2 \cdot \frac{a^4 \cdot \pi^2}{4 \cdot h} = \chi \cdot v^2 \cdot \frac{a^2 \cdot \pi^2}{4 \cdot h} = \chi \cdot v^2 \cdot \frac{D^2}{h}$$

One classical value of mantle viscosity is $\chi=10^{22}$ Poise, the plate angular (lateral) speed ω=1.7 °/yr·10^{-6} (v=2 cm/yr), a=6.371·10^8 cm and the thickness of the crust h=100 km one gets $\dot{E}$ =1.27·10^{19} J/yr. In above equation $D=\pi \cdot a/2$

(D=1·10^9 cm) serves as horizontal scale of the plates. If we consider the whole lithosphere this value must be multiplied for 4πa^2, obtaining $\dot{E}$ =6.1·10^{19} J/yr.
Recent papers show a model of post-seismic relaxation indicating viscosity values of 10^{18} Poise (Melini et al., 2008; Aoudia et al., 2007, and references therein). Consequently, the power needed to move one plate of large dimension could be significantly lowered possibly to about $\dot{E}$ =1.27·10^{15} J/yr, and to $\dot{E}$ =6.1·10^{15} J/yr for the whole lithosphere.

The tidal friction in the Earth-Moon system can be determined on the basis of the temporal variation of the total rotational energy

$$E_T = \frac{1}{2} C\omega^2 + \frac{1}{2} a_m^2 n_m^2 \cdot \left(\frac{M \cdot M_m}{M + M_m}\right) - G\frac{M \cdot M_m}{a_m}$$

Here C,ω and M are the polar moment of inertia, the angular speed and the mass of the Earth, and a_m, n_m and M_m are the Earth-Moon distance, the Moon's orbital speed and the mass of the Moon, respectively, while G stands for the gravitational constant. Using Kepler's third law and conservation of momentum in the Earth-Moon system we obtain:

$$\dot{E} = C(\omega - n_m)\dot{\omega}$$

This expression gives $\dot{E}$ =1.2·10^{20} J/yr by introducing the parameter's values provided by the IERS. Most of this dissipation occurs in the oceans and shallow seas and only a limited part in the mantle.
According to Ray (2001) the tidal dissipation in the mantle amounts maximum to 0.42·10^{19} J/yr, whereas the total oceanic and shallow seas dissipation is about 0.75·10^{20} J/yr (Egbert and Ray, 2000).
Therefore the residual available power, about 0.6·10^{20} J/yr, could be larger than the one required to move the lithosphere with respect to the mantle.
In this respect, the power expenditure is linked to the squared velocity through a family of viscosity-dependent parabolas (Figure 5.8).
Then, our simplified model is defined by the red parabola branches delimited by the green line, that is the maximum estimate of lithospheric net rotation (Crespi et al., 2007) and the blue line, that is the maximum residual available power from tidal deceleration that could contribute to plate motion.

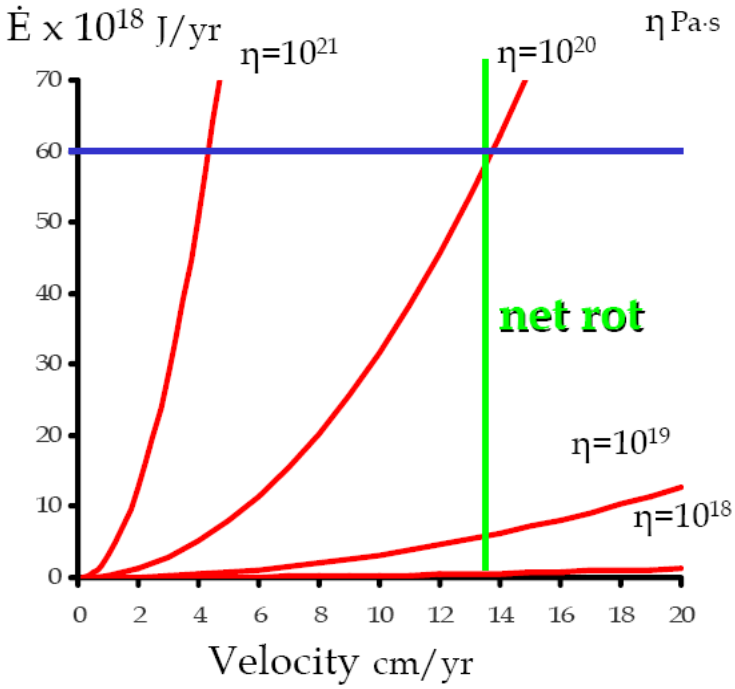

Figure 5.8: Diagram showing the dependence of the dissipated energy from velocity. The family of curves indicating the possible dissipation path at a given viscosity is in red. The green line is the maximum estimate of lithospheric net rotation (Crespi et al., 2007); the blue line is the maximum residual available power from tidal deceleration that could contribute to plate motion.

5.7 Geological and geophysical evidences

Tectonic features on Earth show profound asymmetries as a function of their geographic polarity. A long list of signatures marks the distinction between orogens and related subduction zones and rift zones (Doglioni et al., 2003; 2007). These differences can be observed not comparing east- versus west-facing structures, but moving along the undulated flow of plate motions (Crespi et al., 2007). The E- or NE-directed slabs are less inclined (<50°), the related orogens are more elevated (>1000 m) with respect to the steeper W-directed slabs where the accretionary prisms have much lower average elevation (-1250 m), as shown in Figure 5.9. The rocks outcropping along the orogens related to the E- NE-directed subduction zones represent the entire crustal and upper mantle section, whereas the opposite W-directed slab, the

accretionary prisms are mostly composed of sedimentary, upper crustal rocks, showing that the first orogens have much deeper decollement planes with respect to the second ones. The regional monocline is in average less inclined (<3°), the foredeep has lower subsidence rates (<0.2 mm/yr) along E- or NE-directed subduction zones with respect to the W-directed class where the regional monocline is steeper (in average >6°) and the foredeep-trench subsidence is much faster (>1 mm/yr). Along the E- or NE-directed subduction zones, the subduction hinge moves toward the upper plate, whereas it generally moves away from the upper plate along the opposite W-directed subduction zones. This asymmetric behavior implies, on average, a three times faster lithospheric recycling into the mantle along W-directed subduction zones and provides evidence for polarized mantle convection. Gravity, heat flow anomalies, seismicity, etc. also support these differences. Moreover, along rift zones, the eastern flank is, on average, 100-300 m shallower than the western flank (Figure 5.9).

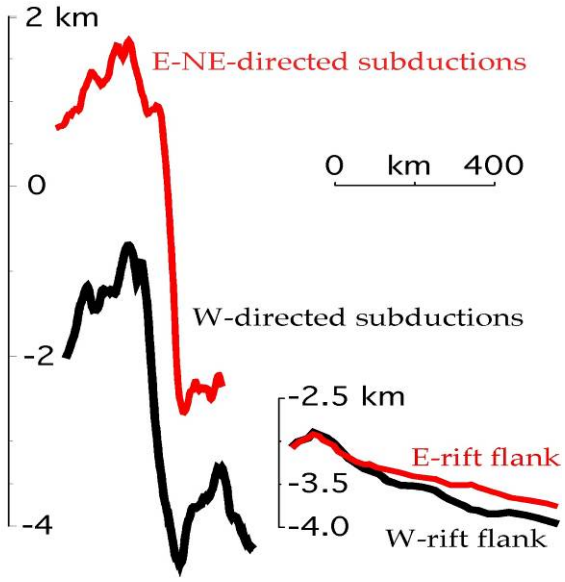

Figure 5.9: Average topographic-bathymetric comparison of subduction zones (left) and rift zones (right). The elevation is higher in the E- or NE-directed subduction zones and the E-flank of rift zones.

All these features have been interpreted as related to the "eastward" relative motion of the asthenosphere with respect to the lithosphere, which should determine different depth and behavior of the basal decollement planes, the metamorphic and the petrological evolution (Doglioni et al., 2007). Moreover a relatively cooler mantle has been envisaged at the Earth's equator (Bonatti et al., 1993), favoring the idea of a rotational component in mantle differentiation.

The distribution of seismic events for magnitude classes, the Gutenberg-Richter law, shows that large magnitude earthquakes are very rare events (e.g., Stein and Wysession, 2003), thus the energy released by one big earthquake seems to deplete temporally the energy budget of plate tectonics, i.e. a slab interacting with the surrounding mantle is not an isolated system, but it participates to a global expenditure of the stored energy.

5.8 Conclusion

We have seen that the Earth's angular deceleration implies a decreasing of Earth's oblateness that produces stresses acting on the lithosphere. In addition, the periodical oscillation of polar motion and rotation rate cannot induce truly significant deformation.

The most important exciting function inducing large displacements in the lithosphere is the tide potential, however the diurnal and semi-diurnal tides are not able to excite the Earth's rotation vector due to the wave symmetry (sectorial and tesseral). Zonal tides are able to induce LOD oscillations at fortnightly period, but with amplitudes within 1ms, minor than the decadal oscillations. At decadal scale, the polar motion is able to induce displacements of reference sites of 1.5 cm, whereas the LOD of about 0.6 mm radial and 0.2 along the N-S direction.

Anyway, the effect of the Earth's rotation on plate tectonics is supported by the distribution in space and time of seismicity (M≥7), which is latitude dependent (Figure 5.3), being very low in the polar areas. Moreover, the time series of LOD, $\log_{10}E$ and N (Figure 5.4) have significant correlation and spectral coherence, particularly for periodicities longer than 25.5 yr (Figure 5.5, 5.6 and 5.7). The LOD decrease corresponds to an increase of the Earth's oblateness and to a polhody amplitude decrease. Accordingly are modulated the occurrence of large seismic events and the release of seismic energy: as the Earth slows down (increase of LOD) the seismicity (either E or N) increases and vice versa. The energy dissipated by the tidal deceleration

could partially contribute to motion of plates overlying an asthenosphere with lateral viscosity variations within 10^{21} Pa·s (Figure 5.8).

Relatively small forces can move a floating plate horizontally, because no work has to be done against gravity, however this can be true when at the base of the lithosphere there is a low viscosity in the decoupling layer, i.e., the weaker LVZ (Chapter 1) in the upper asthenosphere. Increasing the asthenosphere viscosity, larger forces are required to decouple the lithosphere.

The asymmetries in topography-bathymetry over all the Earth, visible when moving along the tectonic mainstream, show a global tuning, where the E- NE-directed subduction zones are the highest as the "eastern" limb of the rift zones (Figure 5.9).

The lithosphere and underlying mantle represent a self-organized system in a critical state - SOC system (Prigogine and Stengers, 1984) - open to external perturbations; plate tectonics is an example of a self-organizing complex system of hierarchical blocks in a critical state (Stern, 2002).

Plate tectonics is a global phenomenology, and the energy source for its activation is not concentrated in limited zones (e.g., subduction zones), but it acts contemporaneously all over the whole Earth's lithosphere, like the Earth's rotation. Recent papers show that only the global seismicity follows the Gutenberg-Richter law, while this simple SOC relation does not hold when considering smaller portions of the Earth (Molchan et al., 1997). All these evidences and models are in favor, even if not conclusive, of a significant control on plate tectonics by the Earth's rotation.

5.9 Future directions

We have seen that several evidences confirm the hypothesis that plate margins are passive rather than active structures maintaining plate motion.

Can the decadal oscillations of LOD and seismicity corroborate that the effect of the rotational dynamics is a basic ingredient of plate tectonics? According to the periods observed during the last 117 years, we are presently moving into a deceleration of the Earth's spin (the LOD increases) and we would then expect an increase of the seismicity.

We have seen in our model (Chapter 3) that the net rotation of the lithosphere with respect to the asthenosphere may reach 13.4 cm/yr; if this process is generated by the torque acting on the lithosphere due to the tidal bulges of the diurnal and semi-diurnal waves, we should have about 0.2 mm

of relative displacement for each bulge transit. At the same time, we wonder if the decadal oscillation of rotation rate are able to effectively modulate the tidal torque to be more or less effective; that is, when the Earth's spin is faster, the tidal torque is minor, then the effect of brake on the lithosphere is minor and minor is the decoupling with the asthenosphere, thus implying minor seismicity. Are the orders of magnitudes of the involved forces compatible with these hypotheses?

Only the formulation of analytic and realistic models matching an amount of observations rather different by nature, can really provide answers on the plate tectonics engine.

We are aware that the arguments proposed in this Chapter 5 do not unravel the problem, nevertheless they can represent a first step to approach the problem.

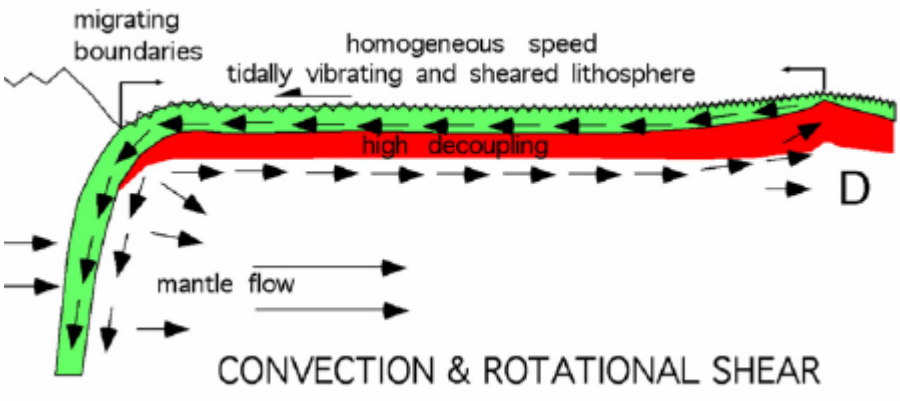

Figure 5.10: The combination of convection and differential rotation due to tidal deceleration, maintaining an east-migrating mantle flow, could drive plate motion (from Doglioni et al., 2007).

Appendix

Solid Earth's energy budget

Table 1 lists the energy sources that keep running the dynamical processes of the Earth and the phenomena that are the most significant consumers of terrestrial energy resources.

Table 1: Solid Earth's energy budgets			
Energy income $\times 10^{21}$ (J/yr)		Energy expenditure $\times 10^{21}$ (J/yr)	
Accretion $\dot{E}_A$	1.9-5.5	Heat Flow $\dot{E}_{HF}$	1.4-1.5
Core formation $\dot{E}_C$	3.2-3.6		
Radioactive decay $\dot{E}_R$	0.2-2.1	Tectonic moment rate $\dot{E}_{TM}$	5.7-7.6
Tidal friction $\dot{E}_T$	0.04-0.12		
Total Energy income	5-11	Total Energy expenditure	7-9

According to Iriyama (1977), the most important sources of energy income rate are the accretion $\dot{E}_A$, the core formation (differentiation) $\dot{E}_C$, the radioactive decay (radiogenic heat production) $\dot{E}_R$ and the tidal friction $\dot{E}_T$. The main components of energy expenditure rate of Earth's planetary energy budget are represented by the heat flow $\dot{E}_{HF}$ and the global tectonic moment rate $\dot{E}_{TM}$, following the global estimation of Kreemer et al. (2002). The annual rates values reported in Table 1 are the results of a compilation of the estimates available in the literature, here briefly discussed.

The real errors of the estimates listed in Table 1 cannot be determined so that we prefer to discuss their order of magnitude. Thus it is natural to assume that the balance is in quasi equilibrium, i.e. there is no statistically meaningful difference between the total of energy rate income and energy rate expenditure.
There are several attempts of estimation of solid Earth's energy rates; consequently we consider useful to report here the minimum and maximum values found in literature.

Energy income rate

- Accretion
The birth and infancy of the Earth was a time of gravitational accumulation and profound differentiation. The total of our knowledge indicates that, in all probability, these events were comparatively rapid and took place very early and simultaneously with the formation of the Earth itself. The time span of accretion and differentiation (core formation) should be between 100 thousand to hundred million years (Monin, 1978; Walter & Trønes, 2004).
The energetics of the gravitational accumulation process has two different scenarios:
-the kinetic energy of the large number of small particles approaching the proto-planet is used for heating
-the kinetic energy of falling bodies is used up for erosion of the globe (cratering, ejection of fragments of rocks from the planet).
The accretion energy rates $\dot{E}_A$ given by different authors, to characterize the accretion process, show relatively significant scatter that depends upon the kind of assumptions made, namely:

- $1.9 \cdot 10^{21}$ J/yr (Sasaki&Nakazawa, 1986)
- $4.9 \cdot 10^{21}$ J/yr (Janle&Meissner, 1986)
- $4.9 \cdot 10^{21}$ J/yr (Verhoogen, 1980)
- $5.6 \cdot 10^{21}$ J/yr (Iriyama, 1977)

thus
$\dot{E}_A \min = 1.9 \cdot 10^{21}$ J/yr (Sasaki&Nakazawa, 1986)
$\dot{E}_A \max = 5.6 \cdot 10^{21}$ J/yr (Iriyama, 1977)

- Core formation

The range of core formation energy rates $\dot{E}_C$ presented in different contributions is relatively small due to the use of more or less similar theoretical models:

- $3.2 \cdot 10^{21}$ J/yr (Flasar & Birch, 1973)
- $3.3 \cdot 10^{21}$ J/yr (Iriyama, 1977)
- $3.5 \cdot 10^{21}$ J/yr (Monin, 1978)
- $3.6 \cdot 10^{21}$ J/yr (Birch, 1965)

thus

$\dot{E}_C \text{ min} = 3.2 \cdot 10^{21}$ J/yr (Flasar & Birch, 1973)

$\dot{E}_C \text{ max} = 3.6 \cdot 10^{21}$ J/yr (Birch, 1965)

- Radioactive decay

In the earliest stage of the Earth's history (4 billion years BP) the radiogenic heat production was about five times higher than at the Present Epoch (Rybach, 1976). Short-lived isotopes with half-lives 10^5-10^7 years, or even much shorter, may have had sufficient effect to melt the central parts of the forming proto-planet. Over the 4.6 Eon (Eon=10^9 years) lifetime of the Earth, four long-life isotopes ^{238}U, ^{235}U ^{232}Th and ^{40}K gave the most important contribution to the radiogenic heat production. The amount of radioactive heat in the crust is 8 TW, in the mantle 23 TW, while in the core it is about 9 TW (Anderson, 1989). More recently Lay et al. (2008) slightly increase these values to a total of 46±3 TW, although a debate on the topic is still alive; for example Hofmeister and Criss (2005) suggest a lower value (31±1 TW). The radioactive annual rates $\dot{E}_R$ published in different scientific contributions are:

- $(2.1 \cdot 10^{20} – 2.1 \cdot 10^{21})$ J/yr (Bott, 1982)
- $1.3 \cdot 10^{21}$ J/yr (Anderson, 1989)
- $2.1 \cdot 10^{21}$ J/yr (Iriyama, 1977)

thus

$\dot{E}_R \text{ min} = 0.2 \cdot 10^{21}$ J/yr (Bott, 1982)

$\dot{E}_R \text{ max} = 2.1 \cdot 10^{21}$ J/yr (Iriyama, 1977)

- Tidal friction

The tidal friction energy rate $\dot{E}_T$ is (0.04-0.12) $\cdot 10^{21}$ J/yr. The value of the despinning rate was five times smaller during Archaikum+Proterozoicum than during the last 570 Ma (Phanerozoicum) (Varga, 2006).

thus

$\dot{E}_T$ min $= 0.04 \cdot 10^{21}$ J/yr (Zschau, 1986)
$\dot{E}_T$ max $= 0.12 \cdot 10^{21}$ this paper

TOTAL ENERGY INCOME rate $\dot{E}_{IN} = (5 \div 11) \cdot 10^{21}$ J/yr
central value $8 \cdot 10^{21}$ J/yr.

Energy expenditure

- *Heat Flow*
$\dot{E}_{HF}$ min $= 1.4 \cdot 10^{21}$ J/yr (Turcotte and Schubert, 2000; Lowrie, 2007)
$\dot{E}_{HF}$ max $= 1.5 \cdot 10^{21}$ J/yr (Lay et al., 2008)

- *Tectonic Moment rate*
Numerically, most of the energy expenditure goes into the global tectonic momentum $\dot{E}_{TM}$ and this shows that most of the energy loss is related to plate tectonic activities. The tectonic moment rate estimated by Kremer et al. (2002) is $7.0 \cdot 10^{21}$ J/yr and is considered by the authors as a minimum value because estimated during a period of low seismic activity and on a short time span. Effectively, the tectonic moment rate strongly depends on the level of seismicity. Consequently we have re-computed this rate on the MGE7 catalog (see the main manuscript) and applying the geometrical mean first on the same time span of Kreemer et al. (2002), obtaining the minimum value; then on the whole catalog, obtaining the maximum value.

$\dot{E}_{TM}$max $= 5.7 \cdot 10^{21}$ J/yr
$\dot{E}_{TM}$max $= 7.6 \cdot 10^{21}$ J/yr

TOTAL ENERGY EXPENDITURE *rate* $\dot{E}_{OUT} = (7 \div 9) \cdot 10^{21}$ J/yr
central value $8 \cdot 10^{21}$ J/yr

ENERGY EXPENDITURE-INCOME $\Delta\dot{E} \approx 0$ J/yr
The balance is in equilibrium, i.e., there is no statistically meaningful difference between the total of energy rate income and expenditure.

References

Almavict, M., Legros, H., 1991. Stresses in the lithosphere induced by geophysical processes of degree two, Manuscripta Geodaetica, 16, 333-352.

Altamimi, Z., Sillard, P., and Boucher, C., 2002 a. ITRF2000: A new release of the International Terrestrial Reference Frame for earth science applications, J. Geophys. Res., 107, B10, 2214, doi:10.1029/2001JB000561.

Altamimi, Z., Sillard, P., and Boucher, C., 2002 b. The impact of No-Net-Rotation Condition on ITRF2000, Geophys. Res. Lett., 30, 2, 1064, doi:10.1029/2002GL016279.

Altamimi, Z., X., Collilieux, J., Legrand, B., Garayt, C., Boucher, 2007. ITRF2005: A new release of the International Terrestrial Reference Frame based on time series of station positions and Earth Orientation Parameters. J. Geophys. Res., 112, B09401, doi:10.1029/2007JB004949

Anderson, D.L., 1989. *Theory of the Earth*, Blackwell Scientific Publications.

Anderson, D.L., 2000. Thermal state of the upper mantle; no role for mantle plumes, Geophys. Res. Lett., 27, 22, 3623-3626.

Anderson, D.L., 2005. Scoring hotspots; the plume & plate paradigms: in *Plates, Plumes and Paradigm*s, G.R. Foulger, J.H. Natland, D.C. Presnall, and D.L. Anderson (Eds), GSA Sp. Paper 388, 31-54.

Anderson, D.L., and Schramm, K.A., 2005. Global hotspot maps; in *Plates, Plumes and Paradigms*, G.R. Foulger, J.H. Natland, D.C. Presnall, and D.L. Anderson (Eds), GSA Sp. Paper 388, 19-29.

Anderson, D.L., 2007. *New Theory of the Earth*, Blackwell Scientific Publications , 1-366.

Aoudia A., Ismail-Zadeh A.T., Romanelli F., 2007. Buoyancy-driven deformation and contemporary tectonic stress in the lithosphere beneath Central Italy, Terra Nova, 19, 490–495.

Arias E. F., Charlot P., Feissel M., Lestrade J.-F., 1995. The Extragalactic Reference System of the International Earth Rotation Service, ICRS, Astron. Astrophys., 303, 604–608.

Argus, D.F., and Gordon, R.G., 1991. No-Net-Rotation model of current plate velocities incorporating plate motion model NUVEL-1, Geophys. Res. Lett., 18, 2038-2042.

Baccheschi, P., L., Margheriti, M. S., Steckler, 2007. Seismic anisotropy reveals focused mantle flow around the Calabrian slab (southern Italy). Geophys. Res. Lett., 34, L05302, doi:10.1029/2006GL028899.

Bally, A. W., L., Burbi, C., Cooper, R., Ghelardoni, 1986. Balanced sections and seismic reflection profiles across the central Apennine, Mem. Soc. Geol. It., 35, 257-310.

Barzaghi, R., Borghi, A., Crespi, M., Pietrantonio, G. and Riguzzi F., 2004. GPS permanent network solution: the impact of temporal correlations, Proceedings of the V Hotine-Marussi Symposium on Mathematical Geodesy , F. Sansò Editor, 127, 179-183, Springer Verlag.

Battaglia, M., M. H., Murray, E., Serpelloni, R., Bürgmann, 2004. The Adriatic region: An independent microplate within the Africa-Eurasia collision zone, Geophys. Res. Lett., 31, L09605, doi:10.1029/2004GL019723.

Beavan, J., 2005. Noise properties of continuous GPS data from concrete pillar geodetic monuments in New Zealand and comparison with data from U.S. deep drilled braced monuments, J. Geophys. Res. 110, doi: 10.1029/2005JB003642.

Bercovici, D., 1998. Generation of plate tectonics from lithosphere-mantle flow and void-volatile self-lubrication, Earth Planet. Sci. Lett., 154, 139–151.

Beutler, G., et al., 2007. Bernese GPS Software, edited by Dach, R., U., Hugentobler, P., Fridez,, M., Meindl, Astronomical Institute, University of Bern.

Biagi, L., Pietrantonio, G., and Riguzzi, F., 2005. Tidal and polar modeling effect on regional GPS networks, poster presented at EGU 2005 General Assembly, Vienna.

Bianco, G., R., Devoti, V., Luceri, 2003. Combination of loosely constrained solutions, IERS Technical Note N. 30, 107-109.

Birch F., 1965. Energetics of core formation, Journal of Geophysical research, 69, 4377-4388.

Bird, P., 2003. An updated digital model of plate boundaries. Geochem. Geophys. Geosyst., 4 (3), 1027. doi:10.1029/2001GC000252.

Bizouard, C. and D. Gambis, 2008. The combined solution C04 for Earth Orientation Parameters, recent improvements, Springer Verlag series.

Blewitt, G., Lavallée, D., Clarke, P., and Nurutdinov, K., 2001. A new global mode of the Earth deformation: Seasonal cycle detected, Science, 294, 2342–2345.

Bonatti, E., 1990. Not So Hot "Hot Spots" in the Oceanic Mantle, Science, 250, 107-111.

Bonatti E., Seyler M., Sushevskay N., 1993. A Cold Suboceanic Mantle Belt at the Earth's Equator, Science, 261, 5119, 315-320.

Bostrom, R.C., 1971. Westward displacement of the lithosphere, Nature, 234, 356-538.

Bostrom, R.C., 2000. Tectonic consequences of the Earth's rotation, Oxford University Press.

Bott M.P.H., 1982. The interior of the Earth: Its structure, construction and evolution, E. Arnold Publ. Ltd

Bott, M.H.P., 1993. Modeling the Plate-Driving Mechanism, Journal of the Geological Society, 150, 941-951.

Boucher, C. and Altamimi, Z., 1996. International Terrestrial Reference Frame, GPS World, 7, 71–74.

Boucher, C., 2001. Terrestrial coordinate systems and frames, in Encyclopedia of Astronomy and Astrophysics, Version 1.0, Nature Publishing Group, and Bristol: Institute of Physics Publishing, 3289–3292.

Bruyninx, C., 2004. The EUREF Permanent Network: a multi-disciplinary network serving surveyors as well as scientists, GeoInformatics, 7, 32-35.

Burke , K., and J. T., Wilson, 1972. Is the African Plate Stationary ?, Nature, 239, 448-449.

Calais, E., et al. 2000. REGAL: a permanent GPS network in the Western Alps. Configuration and first results, C. R. Acad. Sci. Paris, 331, 435-442.

Calcagnile, G., G.F., Panza, 1981. The main characteristics of the lithosphere-

asthenosphere system in Italy and surrounding regions, Pure Appl. Geophys., 119, 865-879.

Calcagnile, G., 1991. Deep structure of Fennoscandia from fundamental and higher mode dispersion of Rayleigh waves, Tectonophysics, 195, 139–149.

Carlson, R.L., 1983. Plate Motions, Boundary Forces, and Horizontal Temperature Gradients: Implications for the Driving Mechanism, Tectonophysics, 99, 149-164.

Carlson, R. L., T. W. C., Hilde ,S., Uyeda, 1983. The driving mechanism of plate tectonics; relation to age of the lithosphere at trenches, Geophys. Res. Lett., 10, 297– 300.

Carminati, E., A. M., Negredo, J. L., Valera, C., Doglioni, 2005. Subduction-related intermediate-depth and deep seismicity in Italy: insights from thermal and rheological modeling, Phys. Earth Planet. Int., 149, 65–79.

Cartwright, D. E. and Tayler, R. J., 1971. New Computations of the Tide-Generating Potential, Geophys. J. Roy. Astr. Soc., 23, 45–74.

Catalano, R., Doglioni, C., Merlini, S., 2001. On the Mesozoic Ionian basin, Geophys. J. Int., 144, 49-64.

Cathles, L. M., 1975. *The viscosity of the earth's mantle*. Princeton, NJ, Princeton University Press.

Channell, J.E.T., 1996. Paleomagnetism and paleogeography of Adria, in Paleomagnetism and Tectonics of the Mediterranean Region, edited by A. Morris and D. H. Tarling, Geol. Soc. Spec. Publ., 105, 119–132.

Chao B.F. and Gross R.S. 2005. Did the 26 December 2004 Sumatra, Indonesia, earthquake disrupt the Earth's rotation as the mass media have said? EOS, 86, 1-2. Soc., 32, 203-217.

Chao, B.F., 1989. Length of day variation caused by El-Nino-Southern Oscillation and Quasi-Biennial Oscillation, Science, 243, 923-925.

Chapanov Y.A., 2006. On the long-periodical oscillations of the Earth Rotation. Proceedings of the "Journées 2005 Systèmes de Référence Spatio-Temporels", A. Brzezinski, N. Capitaine and B. Kolaczek (eds.), Space Research Centre PAS, Warsaw, Poland, s2-12, 129-130.

Chapple, W.M., and Tullis, T.E., 1977. Evaluation of the Forces that Drive the Plates, Journal of Geophysical Research, 82, 1967-1984.

Chase, C. G., 1972. The n-plate problem of plate tectonics, Geophys. J. R. Astr. Soc., 29, 17–122.

Chase, C. G., 1978. Plate kinematic: the America, East Africa and the rest of the world, Earth Planet. Sci. Lett., 37, 355–368.

Chiarabba, C., L., Jovane, R., DiStefano, 2005. A new view of Italian seismicity using 20 years of instrumental recordings, Tectonophysics, 395, 251– 268.

Cochran , E., S., Vidale, J. E., Tanaka, 2004. Earth tides can trigger shallow thrust fault earthquakes, Science, 306, 1164-1166.

Cloetingh, S.P.A.L., M.J.R., Wortel, N.J., Vlaar, 1982. Evolution of passive continental margins and initiation of subduction zones, Nature, 297, 139-142.

Coats, R. R., 1962. Magma type and crustal structure in the Auletian arc, in The Crust of the Pacific Basin, American Geophysical Union Monograph, 6, 92-109.

Conrad, C. P., and C. Lithgow-Bertelloni, 2003. How mantle slabs drive plate tectonics, Science, 298, 207–209.

Corti, G., Cuffaro, M., Doglioni, C., Innocenti, F., Manetti, P., 2006. Coexisting geodynamic processes in the Sicily Channel. In: Y. Dilek and S. Pavlides (Eds), Postcollisional tectonics and magmatism in the Mediterranean region and Asia, Geol. Soc. Am. Sp. Paper, 409, 83-96.

Courtillot V., Davaille, A., Besse J. and Stock J., 2003. Three distinct types of hotspot in the Earth's mantle, Earth Planet. Sci. Lett., 205, 295-308.

Cox, A., Doell, R.R., and Darlymple, G.B., 1963. Geomagnetic polarity epochs and Pleistocene geochronometry, Nature, 198, 1049-1051

Crespi, M., M., Cuffaro, C., Doglioni, F., Giannone, F., Riguzzi, 2007. Space geodesy validation of the global lithospheric flow, Geophys. J. Int., 168, 2, 491-506.

Cruciani, C., Carminati, E., Doglioni, C., 2005. Slab dip vs. lithosphere age: no direct function, Earth Planet. Sci. Lett., 238, 298-310.

Cuffaro M., Caputo M. and Doglioni C., 2004. On the sub-rotation of a plate, Journal of Virtual Explorer, 14.

Cuffaro, M., D. M., Jurdy, 2006. Microplate motions in the hotspot reference frame, Terra Nova, 18, 276–281.

Cuffaro, M., C., Doglioni, 2007. Global kinematics in the deep vs. shallow hotspot reference frames, in *Plates, plumes, and planetary processes*, ed. G. R. Foulger and D. M. Jurdy, Geol. Soc. Am. Spec. Pap., 430, 359–374, doi:10.1130/2007.2430(18).

Cuffaro M., 2007. Plate kinematic models, P.h.D. Earth Sciences Thesis, University of Rome La Sapienza

Cuffaro, M., M., Caputo, C., Doglioni, 2008. Plate sub-rotations, Tectonics, 2710.1029/2007TC002182 TC4007.

Dalrymple, G. B., M. A. Lanphere, and D. A. Clauge, 1980. Conventional and 40Ar–39Ar and K–Ar ages of volcanic rocks from Ojin (site 430), Nintoku (site 432), and Suiko (site 423) seamounts and the chronology of volcanic propagation along the Hawaiian–Empeor chain, Init. Rep. Deep Sea Drill Proj., 55, 659–676.

Davies, G.F., 1988. Ocean bathymetry and mantle convection: 1. large-scale flow and hotspots, J. Geophys. Res., 93, 10467-10480.

Davies, P., G., Blewitt, 2000. Methodology for global geodetic time series estimation: a new tool for geodynamics, J. Geophys. Res., 105, B5, 11083-11100.

D'Agostino, N., G., Selvaggi, 2004. Crustal motion along the Eurasia-Nubia plate boundary in the Calabrian Arc and Sicily and active extension in the Messina Straits from GPS measurements, J. Geophys. Res., 109, B11402, doi:10.1029/ 2004JB002998.

DeMets, C., Gordon, R.G., Argus, F., and Stein, S., 1990. Current plate motions, Geophys. J. Int., 101, 425-478.

DeMets, C., Gordon, R.G., Argus, D.F., S. Stein, 1994. Effect of recent revisions to the geomagnetic reversal time scale on estimates of current plate motions, Geophys. Res. Lett., 21, 20, 2191-2194.

Denis, C., Schreider, A.A., Varga, P., and Zavoti, J., 2002. Despinning of the Earth rotation in the geological past and geomagnetic paleointensities, J. Geodynamics, 34, 667-685.

Dermanis, A., 2001. Global Reference Frames: Connecting Observation to Theory and Geodesy to Geophysics, IAG Scientific Assembly.

Dermanis, A., 2002. The rank deficiency in estimation theory and the definition of reference frames, Proceedings of V Hotine-Marussi

Symposium on Mathematical Geodesy, F. Sanso` Editor, IAG Symposia, vol. 127, 145-156, Springer.

Dermanis, A., 2006. The definition of a meaningful International Terrestrial Reference System. Problems and Prospects, presented at the European Geophysical Union (EGU) General Assembly 2006, 2-7 April, Vienna; http://der.topo.auth.gr/DERMANIS/ENGLISH/Index_ENGLISH.htm

Devoti, R., C., Ferraro, E., Gueguen, R., Lanotte, V., Luceri, A., Nardi, R., Pacione, P., Rutigliano, C., Sciarretta, F., Vespe, 2002. Geodetic control on recent tectonic movements in the central Mediterranean area, Tectonophysics, 346, 151– 167.

Devoti, R., F. Riguzzi, M., Cuffaro, C., Doglioni, 2008. New GPS constraints on the kinematics of the Apennines subduction, Earth Planet. Sci. Lett., 273, 163-174.

Dickey, J.O., Bender, P.L., Faller, J.E., Newhall, X.X., Ricklefs, R.L., Ries, J.G., Shelus, P.J., Veillet, C., Whipple, A.L., Wiant, J.R., Williams, J.G., Yoder, C.F., 1994. Lunar laser ranging: a continual legacy of the Apollo program, Science, 265, 482-490.

Dickey, J. O., 1995. Earth Rotation, in *Global Earth Physics*, A handbook of physical constants, AGU, 356-368.

Doglioni, C., 1990. The global tectonic pattern, J. Geodyn., 12, 21-38.

Doglioni C., 1991. A proposal of kinematic modelling for W-dipping subductions - Possible applications to the Tyrrhenian - Apennines system. Terra Nova, 3, 4, 423-434.

Doglioni, C., 1993. Geological evidence for a global tectonic polarity, Journal of the Geological Society, London, 150, 991-1002.

Doglioni, C., 1994. Foredeeps versus subduction zones, Geology, 22, 3, 271-274.

Doglioni, C., Mongelli, F., Pieri, P., 1994. The Puglia uplift (SE-Italy): an anomaly in the foreland of the Apenninic subduction due to buckling of a thick continental lithosphere, Tectonics, 13, 5, 1309-1321.

Doglioni C., Mongelli F. & Pialli G.P., 1998. Boudinage of the Alpine belt in the Apenninic back-arc. Mem. Soc. Geol. It., 52, 457-468.

Doglioni, C., E., Gueguen, P., Harabaglia, F., Mongelli, 1999. On the origin of W-directed subduction zones and applications to the western

Mediterranean, Geol. Soc. London Sp. Publ., 156, 541-561.

Doglioni, C., Harabaglia, P., Merlini, S., Mongelli, F., Peccerillo, A. and Piromallo, C., 1999. Orogens and slabs vs their direction of subduction. Earth Sci. Reviews, 45, 167-208.

Doglioni, C., Innocenti, F., Mariotti, S., 2001. Why Mt. Etna?, Terra Nova, 13, (1), 25-31.

Doglioni, C., Carminati, E. and Bonatti, E., 2003, Rift asymmetry and continental uplift, Tectonics, 22, 3, 1024, doi:10.1029/2002TC001459.

Doglioni, C., F., Innocenti, C., Morellato, D., Procaccianti, D., Scrocca, 2004. On the Tyrrhenian sea opening, Mem. Descrittive Carta Geologica d'Italia, 64, 147-164.

Doglioni, C., Green, D., and Mongelli, F., 2005. On the shallow origin of hotspots and the westward drift of the lithosphere: in Plates, Plumes and Paradigms, G.R. Foulger, J.H. Natland, D.C. Presnall, and D.L. Anderson (Eds), GSA Sp. Paper 388, 735-749.

Doglioni, C., E., Carminati, M., Cuffaro, 2006. Simple kinematics of subduction zones, Int. Geol. Rev., 48, 479-493.

Doglioni, C., E., Carminati, M., Cuffaro, D., Scrocca, 2007. Subduction kinematics and dynamic constraints, Earth Sci. Rev., 83, 125-175, doi:10.1016/j.earscirev.2007.04.001.

Dow, J.M., R.E. Neilan, G. Gendt, 2005. The International GPS Service (IGS): Celebrating the 10th Anniversary and Looking to the Next Decade, Adv. Space Res., 36, 3, 320-326.

Drewes, H. and Meisel, B., 2003. An Actual Plate Motion and Deformation Model as a Kinematic Terrestrial Reference System, Geotechnologien Science Report No. 3, 40-43, Potsdam.

Duncan, R.A., and I. McDougall, 1976. Linear volcanism in French Polynesia, J. Volcanol. Geotherm. Res., 1,197-227.

Dziewonski, A.M., G. Ekström, and N.N. Maternovskaya, 2000. Centroid-moment tensor solutions for July-September, 1999, Phys. Earth Planet. Int., 119, 311-319.

Egbert, G.D. and R.D., Ray, 2000. Significant dissipation of tidal energy in the deep ocean inferred from satellite altimeter data, Nature 405, 775-778.

Engdahl, E.R. and A. Villaseñor, , 2002. Global Seismicity: 1900-1999, in

W.H.K. Lee, H. Kanamori, P.C. Jennings, and C. Kisslinger (editors), *International Handbook of Earthquake and Engineering Seismology*, Part A, Chapter 41, 665-690, Academic Press.

ESA, 1997. *The Hipparcos and Tycho catalogues*, European Space Agency Publication, Novdrijk, SP–1200, June 1997, 19 volumes.

Ewing, M, J. I., Ewing, M., Talwani, 1964. Sediment distribution in the oceans: the Mid-Atlantic Ridge, Geol. Soc. Am. Bull., 75, 17-36.

Faccenna, C., C., Piromallo, A., Crespo-Blanc, L., Jolivet, F., Rossetti, 2004. Lateral slab deformation and the origin of the western Mediterranean arcs, Tectonics, 23, TC1012, doi:10.1029/2002TC001488.

Fernandes, R.M.S., B.A.C., Ambrosius, R., Noomen, L., Bastos, M.J.R., Wortel, W. Spakman, R., Govers, 2003. The relative motion between Africa and Eurasia as derived from ITRF2000 and GPS data, Geophys. Res. Lett. 30(16), 1828.

Fischer, K.M., Fouch, M.J., Wiens, D.A., and Boettcher, M.S., 1998. Anisotropy and Flow in Pacific Subduction Zone Back-arcs, Pure appl. geophys. 151, 463–475.

Flasar F., Birch F., 1973. Energetics of core formation: A correction, Journal of Geophysical Research, 78, 6101-6103.

Forsyth, D., and Uyeda, S., 1975. On the relative importance of driving forces of plate motion, Geophys. J. R. Astron. Soc., 43, 163-200.

Foulger, G.R., Natland, J.H., Presnall, D.C. and Anderson, D.L., 2005. Plates, Plumes and Paradigms, GSA Sp. Paper 388, 1-861.

Fowler, C.M.R., 2005. *The Solid Earth, an introduction to Global Geophysics*, Second Edition, Cambridge University Press.

Frepoli, A., G. Selvaggi, C. Chiarabba, and A. Amato, 1996. State of stress in the Southern Tyrrhenian subduction zone from fault–plane solutions, Geophys. J. Int., 125, 879– 891.

Georgieva, K., 2002. Long-term changes in atmospheric circulation, earth rotation rate and north-south solar asymmetry, Physics and Chemistry of the Earth, 27, 433–440.

Gipson, J.M., Ma, C., 1998. Site displacement due to variation in Earth rotation, J. Geophys. Res., 103, B4, 7337-7350.

Giunchi and Spada, 2000. Postglacial rebound in a non-Newtonian spherical Earth, Geophys. Res. Lett., 27, 2065-2068.

Goes, S., D., Giardini, S., Jenny, C., Hollenstein, H.-G., Kahle, A., Geiger, 2004. A recent tectonic reorganization in the south-central Mediterranean, Earth Planet. Sci. Lett., 226, 335– 345.

Gordon, R.G., 1995. Present plate motion and plate boundaries, Glob. Earth Phys., AGU Ref. Shelf, 1, 66-87.

Grenerczy, G., G., Sella, S., Stein, A., Kenyeres, 2005. Tectonic implications of the GPS velocity field in the northern Adriatic region, Geophys. Res. Lett., 32, L16311, doi:10.1029/2005GL022947.

Gripp, A.E. and Gordon, R.G., 1990. Current plate velocities relative to the hotspots incorporating the NUVEL-1 global plate motion model. Geophys. Res. Letts, 17, 1109-1112

Gripp, A.E., and Gordon, R.G., 2002. Young tracks of hotspots and current plate velocities, Geophys. J. Int., 150, 321-361.

Gross R. S., 2000. The excitation of the Chandler wobble, Geophys.Res. Lett. 27 (15), 2329-2332.

Gueguen, E., C., Doglioni, M., Fernandez, 1997. Lithospheric boudinage in the Western Mediterranean back-arc basins, Terra Nova, 9, 4, 184-187.

Gutenberg, B., C.F., Ricther, 1942. Earthquake magnitude, intensity, energy and acceleration, Bull. Seismol. Soc. Am, 32, 163-191.

Gutenberg, B., C.F., Ricther, 1954. Seismicity of the Earth and associated phenomena, Princeton, N.J., Princeton University Press.

Heflin, M., et al., 2004, http://sideshow.jpl.nasa.gov/mbh/series.html.

Henderson, D.M., 2001. New visualizations of global tectonic plate motions and plate boundary interactions, Terra Nova, 13, 70-78.

Herring T.A., J.L., Davis, I.I., Shapiro, 1990. Geodesy by radio interferometry: The application of Kalman filtering to the analysis of very long baseline interferometry data, J. Geophys. Res., 95 (B8), 12561–12581.

Herring, T. A., D.-N. Dong, and R. W. King, 1991. Submilliarcsecond determination of pole position by GPS measurements, Geophys. Res. Lett., 18, 1893-1896.

Herring, T. A., 1992. Modeling Atmospheric Delays in the Analysis of Space Geodetic Data, Proceedings of Refraction of Transatmospheric Signals in Geodesy, Netherlands Geodetic Commission Series, 36, The Hague, Netherlands, pp. 157–164.

Hess, H. H., 1962. History of ocean basins, in Petrologic studies: a volume in honor of A. F. Buddington, edited by A. E. J. Engel, H. L. James, and B. F. Leonard, Geol. Soc. Am.

Heuret, A., S., Lallemand, 2005. Plate motions, slab dynamics and back-arc deformation, Phys. Earth Planet. Int., 149, 31-51.

Hide R. and J. O. Dickey, 1991. Earth's variable rotation, Science, 253, 629-637.

Hirth, G., and Kohlstedt, D.L., 1996. Water in the oceanic upper mantle: implications for rheology, melt extraction and the evolution of the lithosphere: Earth Planet. Sci. Lett., v. 144, p. 93-108.

Hofmeister, A.M. and Criss, R.E., 2005. Earth's heat flux revised and linked to chemistry. Tectonophysics 395, 159–177.

Hofmann-Wellenhof B., H. Lichtenegger, J. Collins, 2001. *GPS Theory and Practice*, Springer Wien NewYork.

Hollenstein, Ch., H.-G., Kahle, A., Geiger, S., Jenny, S., Goes, D., Giardini, 2003. New GPS constraints on the Africa-Eurasia plate boundary zone in southern Italy, Geophys. Res. Lett., 30(18), 1935, doi:10.1029/2003GL017554.

Holtzman, B.K., Groebner, N.J., Zimmerman, M.E., Ginsberg, S.B., and Kohlstedt, D.L., 2003. Stress-driven melt segregation in partially molten rocks: G3, v. 4, 8607, doi:10.1029/2001GC000258.

Holmes, A., 1928. Theory of continental drift: a symposium on the origin and movement of land masses, both inter-continental and intra-continental, as proposed by Alfred Wegener, Nature, 122, 431-433.

Hunstad, I., Selvaggi, G., D'Agostino, N., England, P., Clarke, P., Pierozzi, M., 2003. Geodetic strain in peninsular Italy between 1875 and 2001, Geophys. Res. Lett., 30, 4, 1181, doi:10.1029/2002GL016447.

Iriyama J., 1977. Energy balance in the Earth's interior, Tectonophysics, 40, 243-249.

Isacks, B., and P. Molnar (1971), Distribution of stresses in the descending lithosphere from a global survey of focal–mechanism solutions of mantle earthquakes, Rev. Geophys., 9, 103–174.

Jacoby, W.R., 1980. Plate Sliding and Sinking in Mantle Convection and the Driving Mechanism, *In*:

Janle P., Meissner R., 1986. Structure and evolution of the terrestrial planets, Surveys in Geophysics, 8, 107-186.

Jault, D. and J. Le Mouel, 1990. Core-mantle boundary shape: constraints inferred from the pressure torque acting between the core and mantle, *Geophys.J. Int.*, 101, 233–241.

Jault, D., C. Gire, and J. J. Le Mouel, 1988. Westward drift, core motions and exchanges of angular momentum between core and mantle, Nature, 333, 353–356.

Jenny, S., S., Goes, D., Giardini, H.-G., Kahle, 2006. Seismic potential of Southern Italy, Tectonophysics, 415, 81-101.

Jeffreys, H., 1975. *The Earth*, Cambridge University Press.

Johnson, H.O., D. C., Agnew, 1995. Monument motion and measurements of crustal velocities, Geophys. Res. Lett. 22 N. 21, 2905-2908.

Jordan, T.H., 1974. Some Comments on Tidal Drag as a Mechanism for Driving Plate Motions: J. Geophys. Res., 79, 14, 2141-2142.

Jordan, T.H., 1975. The continental tectosphere, Reviews of Geophysics, 13, 1–12.

Jurdy, D.M., M., Stefanick, 1988. Plate-driving forces over the Cenozoic era, J. Geophys. Res., 93, 11833–11844.

Jurdy, D.M., 1990. Reference frames for plate tectonic and uncertainties, Tectonophysics, 182, 373-382.

Kanamori H., 1977. The energy release in great earthquakes, J. Geophys. Res., 82, 20, 2981-2987.

Kane R.P. and Trivedi N.B. 1990. Decade fluctuations in the rotation rate of the Earth in the last 200 years. Pageoph, 132, 4, 771-799.

Kendrick, E., Bevis, M., Smalley, Jr.R., Brooks, B., Barriga Vargas, R., Laurìa, E., and Souto Fortes, L.P., 2003. The Nazca–South America Euler vector and its rate of change, J. South Amer. Earth Sci., 16, 125-131.

Klyashtorin, L.B., 2001. Climate change and long term fluctuations of commercial catches: the possibility of forecasting, FAO Fisheries Technical Paper, 410, FAO, Rome.

Knopoff, L., 1972. Observation and inversion of surface-wave dispersion, Tectonophysics, 13, 1-4, 497-519.

Knopoff, L., and Leeds, A., 1972. Lithospheric Momenta and the Deceleration of the Earth, Nature, 237, 12, 93-95.

King, R.W., Y., Bock, 2002. Documentation for the GAMIT analysis software, release 10.1, Massachusetts Institute of Technology, Cambridge, MA.

Kostrov, V.V., 1974. Seismic moment and energy of earthquakes, and seismic flow of rocks, Izv. Acad. Sci. USSR Phys. Solid Earth, 1, Eng. Transl., 23-44.

Kovalevsky, J., Mueller, I. I., and Kolaczek, B., (Eds.), 1989. *Reference Frames in Astronomy and Geophysics*, Kluwer Academic Publisher, Dordrecht.

Kovalevsky, J., Lindegren, L., Perryman, M. A. C., Hemenway, P. D., Johnston, K. J., Kislyuk, V. S., Lestrade, J.-F., Morrison, L. V., Platais, I., R¨oser, S., Schilbach, E., Tucholke, H.-J., de Vegt, C., Vondr´ak, J., Arias, F., Gontier, A.-M., Arenou, F., Brosche, P., Florkowski, D. R., Garrington, S. T., Preston, R. A., Ron, C., Rybka, S. P., Scholz, R.-D., and Zacharias, N., 1997. The Hipparcos Catalogue as a realization of the extragalactic reference system, Astron. Astrophys., 323, 620–633.

Kreemer, C., W. E., Holt, A. J., Haines, G. Blewitt and D. Lavallée, 2000. On the determination of a global strain rate model, Earth Planets and Space, 52, 765-770.

Kreemer, C., W. E., Holt, 2001. A no-net-rotation model of present-day surface motion, Geophys. Res. Lett., 28, 4407-4410.

Kreemer, C., W. E., Holt, A. J., Haines, 2003. An integrated global model of present-day plate motions and plate boundary deformation, Geophys. J. Int., 154, 8-34.

Lay T., Hernlund J., Buffet B.A, 2008. Core-mantle boundary heat flow, Nature Geoscience, 1, 25-32.

Lambeck, K., 1980. *The Earth's variable rotation: geophysical causes and consequences*. Editors Batchelor, G.K. and Miles, J.W., Cambridge University Press, Cambridge.

Lambeck, K., 1988. *Geophysical Geodesy*, *The slow deformations of the Earth*, Oxford University Press.

Le Pichon, X., 1968. Sea-floor spreading and continental drift, J. Geophys. Res., 73: 12, 3661-3697.

Lister, C. R. B., 1975. Gravitational drive on oceanic plates caused by thermal contraction, Nature, 257, 663-665.

Lliboutry, L., 1974. Plate movement relative to a rigid lower mantle, Nature, 250, 298– 300.

Lowrie W., 2007. Fundamentals of Geophysics, Cambridge University Press

Lucente, F.P., Margheriti, L., Piromallo, C., Barruol, G., 2006. Seismic anisotropy reveals the long route of the slab through the western-central Mediterranean mantle, Earth Planet. Sci. Lett., 241, 3-4, 517-529.

Ma, C. and Shaffer, D. B., 1991. Stability of the extragalactic reference frame realized by VLBI, in Reference Systems, Hughes, J. A., Smith, C. A., and Kaplan, G. H. (eds), U. S. Naval Observatory, Washington, pp. 135–144.

Maley, A., 1991. *Classroom practice: an overview*, in R. Bowers and C. Brumfit eds.

Mao, A., C. G. A., Harrison, T. H., Dixon, 1999. Noise in GPS coordinate time series, J. Geophys. Res. 104 N. B2, 2797-2816.

Marcus, S.L., Chao, Y., Dickey, J.O., Gegout, P., 1998. Detection and modeling of nontidal oceanic effects on Earth's rotation rate, Science, 281, 1656-1659.

Maslov, L.A., 1991. Geodynamics of the Pacific segment of the Earth. Nauka, Moscow.

Mathews, P. M., Herring T. A., and Buffet, B. A., 2002. Modeling of nutation-precession: New nutation series for nonrigid Earth, and insights into the Earth's interior, J. Geophys. Res., 107, B4, 10.1029/2001JB000390.

McCarthy, D. D., and Petit, G., 2004. IERS Conventions (2003), IERS Technical Note No.32, Verlag des Bundesamts für Kartographie uns Geodäsie, Frankfurt am Main.

McKenzie, D. P., and R. L. Parker, 1967. The North Pacific: an example of tectonics on a sphere, Nature, 216, 1276–1280.

McKenzie, D. P., 1967. Some remarks on heat flow and gravity anomalies, J. Geophys. Res., 72, 6261-6273.

McKenzie, D.P., 1968. The Influence of the Boundary Conditions and Rotation on Convection in the Earth's Mantle, The Geophysical Journal, 15, 457-500.

McKenzie, D.P., 1969. Speculations on the Consequences and Causes of Plate Motions, The Geophysical Journal, 18, 1-32.

Melchior, P.J., 1983. *The tides of the planet Earth*, Pergamon.

Melini, D, V Cannelli, A Piersanti, G Spada, 2008. Post-seismic rebound of a spherical Earth: new insights from the application of the Post-Widder inversion formula, Geophys. J. Int., 174, 4, 672-695.

Melosh, H.J., 1977. Global tectonics of a despun planet, Icarus, 31, 221-243.

Meijer, P. Th., and M. J. R., Wortel, 1992. The Dynamics of Motion of the South American Plate, J. Geophys. Res., 97(B8), 11915–11931.

Minster, J. B., and T. H, Jordan, 1978. Present-day plate motions, J. Geophys. Res., 83, 5331–5354.

Molchan, G., Kronrod, T. and Panza, G.F., 1997. Multi-scale seismicity model for seismic risk, BSSA, 87, 5, 1220-1229.

Monin A.S., 1978. On some problems of geophysical fluid dynamics. Proceedings of National Academy of Sciences USA, 75, 1, 34-39.

Montagner, J.-P., 2002. Upper mantle low anisotropy channels below the Pacific Plate, Earth Planet. Sci. Lett., 202, 263-274.

Montuori, C., G. B., Cimini, P., Favali, 2007. Teleseismic tomography of the southern Tyrrhenian subduction zone: New results from seafloor and land recordings, J.G. Res.112, doi:10.1029/2005JB004114.

Moore, G.W., 1973. Westward tidal lag as the driving force of plate tectonics, Geology, 1, 99–100.

Morgan, W. J., 1968. Rises, trenches, great faults and crustal blocks, J. Geophys. Res., 73, 1959–1982.

Morgan, W.J., 1971. Convection plumes in the lower mantle, Nature, 230, 42-43.

Morgan, W. J., 1972. Plate motions and deep mantle convection, Studies in Earth and Space Sciences, Geol. Soc. Am. Mem., 132, 7–22.

Morgan, W.J., 1983. Hotspot tracks and the early rifting of the Atlantic, Tectonophysics, 94, 123–139.

Mueller, I.I., 1971. *Spherical and Practical Astronomy as Applied to Geodesy*, Ungar, New York.

Mueller, I.I., 1985. Reference coordinate systems and frames: Concepts and realization, Bull. Geod., **59**, 181-188.

Mueller I., Beutler G., 1992. The International GPS Service for Geodynamics - Development and Current Status, Proceedings 6th International Geodetic Symposium on Satellite Positioning, 2, 823-835, Ohio State University, Columbus, Ohio.

Müller, R.D., Sdrolias, M., Gaina, C., Roest, W.R., 2008. Age, spreading rates and spreading symmetry of the world ocean crust, Geochem. Geophys. Geosyst., 9, Q04006, doi:10.1029/2007GC001743.

Natland, J.H. and Winterer, E.L., 2005. Fissure control on volcanic action in the Pacific. In: in Plates, Plumes and Paradigms, G.R. Foulger, J.H. Natland, D.C. Presnall, and D.L. Anderson (Eds), GSA Sp. Paper 388,

Nocquet, J.-M., E., Calais, 2004. Geodetic Measurements of Crustal Deformation in the Western Mediterranean and Europe, Pure Appl. Geophys. 161.

Nocquet, J.-M., E., Calais, Z., Altamimi, P,. Sillard, C., Boucher, 2001. Intraplate deformation in western Europe deduced from an analysis of the International Terrestrial Reference Frame 1997 (ITRF97) velocity field, J. Geophys. Res., 106, B6, 11,239-11,257.

Norton, I. O., 1995. Plate motions in the North Pacific; the 43 Ma non event, Tectonics, 14, 1080-1094.

Norton, I. O., 2000. Global hotspot reference frames and plate motion, in *The history and dynamics of global plate motions*, ed. M. A. Richards, R. G. Gordon and R. D. V. der Hilst, Geophys. Monograph.

O'Connell, R., Gable, C.G., and Hager, B., 1991. Toroidal-poloidal partitioning of lithospheric plate motions. In: Glacial Isostasy, Sea-Level and Mantle Rheology (Ed. by R. Sabadini et al.), Kluwer Academic Publisher, 334, 535-551.

Oldow, J.S., L., Ferranti, D. S., Lewis, J. K., Campbell, B., D'Argenio, R., Catalano, G., Pappone, L., Carmignani, P., Conti, C., Aiken, 2002. Active fragmentation of Adria, the north Africa promontory, central Mediterranean orogen, Geology, 30, 779-782.

Oliver, J., B., Isacks, 1967. Deep earthquake zones, anomalous structures in

the upper mantle, and the lithosphere, J. Geophys. Res., 72, 4259-4275.

Orfanidis, S.J., 1996. Optimum Signal Processing. An Introduction, 2nd Edition, Prentice-Hall, Englewood Cliffs, NJ.

Pany T., P., Pesec, G., Stangl, 2001. Network monitoring at the OLG analysis centre, Euref Symposium 2001, available at http://www.epncb.oma.be/_newsmails/papers/

Panza, G., 1980. Evolution of the Earth's lithosphere. In: Mechanisms of continental drift and plate tectonics, Ed. By P.A. Davies and S.K. Runcorn, Academic Press, 75-87.

Panza, G.F., A., Pontevivo, G., Chimera, R., Raykova, A., Aoudia, 2003. The Lithosphere-Asthenosphere: Italy and surroundings, Episodes, 26, 3, 169-174.

Panza, G.F., R., Raykova, E., Carminati, C., Doglioni, 2007. Upper mantle flow in the western Mediterranean, Earth Planet. Sci. Lett., 257, 1-2, 200-214.

Paquet P., V., Dehant, C., Bruyninx, 1997. Earth rotation observations and their geophysical implications, Bull. Astron. Belgrade, 156, 89-108.

Paulson, A., Zhong, S., Wahr J., 2007. Limitations on the inversion for mantle viscosity from postglacial rebound, Geophys. J. Int, 168, 1195-1209.

Pearlman, M.R., Degnan, J.J., and Bosworth, J.M., 2002. The International Laser Ranging Service, Advances in Space Research, 30, 2, 135-143.

Pondrelli, S., C., Piromallo, E., Serpelloni, 2004. Convergence vs. retreat in Southern Tyrrhenian Sea: Insights from kinematics, Geophys. Res. Lett., 31, L06611, doi:10.1029/2003GL019223.

Press, W.H., Teukolsky, S.A., Vetterling. W.T. and Flannery, B.P., 1992. Numerical Recipes in FORTRAN – The Art of Scientific Computing, Cambridge University Press.

Press F. and Briggs P., 1975. Chandler Wobble, earthquakes, rotation, and geomagnetic changes. Nature, 256, 270-273.

Prigogine and Stengers, 1984. Order Out of Chaos. New York: Bantam.

Ranalli, G., 2000. Westward drift of the lithosphere: not a result of rotational drag, Geophys. J. Int., 141, 535-537.

Ray, R. D., Steinberg, D. J., Chao, B. F., and Cartwright, D. E., 1994. Diurnal and Semidiurnal Variations in the Earth's Rotation Rate Induced by Oceanic Tides, Science, 264, 830–832.

Ray R., 2001. Tidal friction in the Earth and Ocean, Journées Luxembourgeoises de Géodynamique´, JLG 89th, Nov. 12-14, http://www.ecgs.lu/.

Reilinger, R., S., McClusky, P., Vernant, S., Lawrence, S., Ergintav, R., Cakmak, H., Ozener, F., Kadirov, I., Guliev, R., Stepanyan, M., Nadariya, G., Hahubia, S., Mahmoud, K., Sakr, A., ArRajehi, D., Paradissis, A., Al-Aydrus, M., Prilepin, T., Guseva, E., Evren, A., Dmitrotsa, S. V., Filikov, F., Gomez, R., Al-Ghazzi, G., Karam, 2006. GPS constraints on continental deformation in the Africa-Arabia-Eurasia continental collision zone and implications for the dynamics of plate interactions, J. Geophys. Res., 111, B05411, doi:10.1029/2005JB004051

Ricard, Y., Doglioni, C., and Sabadini, R., 1991. Differential rotation between lithosphere and mantle: a consequence of lateral viscosity variations, J. Geophys. Res., 96, 8407-8415.

Richardson, R.M., 1992. Ridge Forces, Absolute Plate Motions, and the Intraplate Stress Field, Journal of Geophysical Research, 97, 11,739-11,748.

Ritsema, J., and Allen, R.M., 2003, The elusive mantle plume, Earth Planet. Sci. Lett., 207, 1-12.

Roure, F., P., Casero, R., Vially, 1991. Growth processes and melange formation in the southern Apennines accretionary wedge, Earth Planet. Sci. Lett., 102, 395 – 412.

Rybach L., 1976: Radioactive heat production in rocks and its relation to other petrophysical parameters, PAGEOPH, 114, 309-317

Rychert, C.A., Fischer C.M., Rondenay, S., 2005. A sharp lithosphere–asthenosphere boundary imaged beneath eastern North America. Nature, 436, 542-545.

Rutherford, E., 1905 a. Radium - the cause of the Earth's heat, Harpers Mag, 390-396.

Rutherford, E., 1905 b. Slow transformation products of Radio, Nature, 71, 341-342.

Sagnotti, L., Meloni, A., 1993. Pleistocene rotations and strain in southern Italy: the example of the Sant'Arcangelo basin, Annali di Geofisica, 36, 2,

83-95.

Sasaki S., Nakazawa K., 1986. Metal-silicate fractionation in the growing Earth: Energy source for the terrestrial magma ocean, Journal of Geophysical Research, 91, 9231-9238

Savage, M.K., 1999. Seismic anisotropy and mantle deformation: What have we learned from shear wave splitting?, Reviews of Geophysics, 37, 1, 65–106.

Scherneck, H. G., 1993. Ocean Tide Loading: Propagation of Errors from the Ocean Tide into Loading Coefficients, Man. Geod., 18, 59–71.

Schettino, A., 1999. Computational methods for calculating geometric parameters of tectonic plates, Computers & Geosciences, 25, 897-907.

Schuh, H., Nagel, S., Seitz, T., 2001. Linear drift and periodic variations observed in long time series of polar motion, J. of Geodesy, 74, 701-710.

Schlüter W., D. Behrend, 2007. The International VLBI Service for Geodesy and Astrometry (IVS): current capabilities and future prospects", Journal of Geodesy, 81, 6–8, 379–387.

Scoppola, B., Boccaletti, D., Bevis, M., Carminati, E., and Doglioni, C., 2006. The westward drift of the lithosphere: a rotational drag?, Bull. Geol. Soc. Am., 118, in press.

Scrocca, D., C., Doglioni, F., Innocenti, P., Manetti, A., Mazzotti, L., Bertelli, L., Burbi, S., D'Offizi, 2003. CROP Atlas: seismic reflection profiles of the Italian crust, Mem. Descrittive Carta Geologica d'Italia, *62*, 194.

Scrocca, D., E., Carminati, C., Doglioni, 2005. Deep structure of the Southern Apennines (Italy): thin-skinned or thick-skinned?, Tectonics, 24, doi:10.1029/2004TC001634.

Searle, R.C., 1986. GLORIA investigations of oceanic fracture zones: comparative study of the trasform fault zone, J. Geol. Soc., London, 143, 743-756.

Sella, G. F., T. H., Dixon, A., Mao, 2002. REVEL: A model for recent plate velocity from space geodesy, J. Geophys. Res., 107, B4, 2081, doi:10.1029/2000JB000033.

Selvaggi, G., and RING working group, 2006. La Rete Integrata Nazionale GPS (RING) dell'INGV: una infrastruttura aperta per la ricerca scientifica, X Conferenza nazionale dell'ASITA, Bolzano (Italy) 14-17 November.

Sengoku, A., 1998. A plate motion study using Ajisai SLR data, Earth Planets Space, 50, 611–627

Serpelloni, E., M., Anzidei, P., Baldi, G., Casula, A., Galvani, 2005. Crustal velocity and strain-rate fields in Italy and surrounding regions: new results from the analysis of permanent and non-permanent GPS networks, Geophys. J. Int., 161, 3, 861-880, doi: 10.1111/j.1365-246X.2005.02618.x

Serpelloni, E., G., Vannucci, S., Pondrelli, A., Argnani, G., Casula, M., Anzidei, P., Baldi, P., Gasperini, 2007. Kinematics of the Western Africa-Eurasia plate boundary from focal mechanisms and GPS data, Geophys. J. Int, doi: 10.1111/j.1365-246X.2007.03367.x

Silver, P.G., and Holt, W.E., 2002. The Mantle Flow Field Beneath Western North America, Science, 295, 1054-1057.

Smith, A.D., 1993. The continental mantle as a source for hotspot volcanism, Terra Nova 5, 452–460.

Smith, D.E, Kolenkiewicz,_R. , Nerem, R.S., Dunn, P.J. , Torrence, M.H., Robbins, J.W., Klosko, S.M., Williamson, R.G., Pavlis, E.C., 1994. Contemporary global horizontal crustal motion, Geophys. J. Int, 119, 2, 511-520.

Smith, A.D. and Lewis, C., 1999. The planet beyond the plume hypothesis, Earth Sci. Rev., 48, 135-182.

Solomon, S. C., and N. H. Sleep, 1974. Some simple physical models for absolute plate motions, J. Geophys. Res., *79*, 2557–2567.

Stein, S., 1993. Space geodesy and plate motions, Amer. Geophys. Union, Geodynamics Series, 23, 5-20.

Stein S., Wysession M. 2003. *Introduction to Seismology, Earthquakes, & Earth Structure*, Blackwell Publishing.

Stern, R. J., 2002. Subduction zones, Rev. Geophys., 40, 1012.

Stüwe, K., 2002. *Geodynamics of the lithosphere: An Introduction,* Springer.

Tanaka , S., Ohtake, M., and Sato, H., 2004. Tidal triggering of earthquakes in Japan related to the regional tectonic stress, Earth Planets Space, 56, 511-515.

Tavernier, G., Fagard, H., Feissel-Vernier, M., Le Bail, K., Lemoine, F., Noll, C., Noomen, R., Ries, J.C., Soudarin, L., Valette, J.J., Willis, P. 2006. The

International DORIS Service: genesis and early achievements, in DORIS Special Issue, P. Willis (Ed.), J. of Geodesy, 80, 8-11, 403-417.

Thybo, H., 2006. The heterogeneous upper mantle low velocity zone, Tectonophysics, 416, 53-79.

Turcotte, D.L., and Schubert, G., 1982. *Geodynamics*, Wiley, New York.

Varga P., Gambis D., Bus Z., Bizouard Ch., 2005. The relation between the global seismicity and the rotation of the Earth, Observatoire de Paris, Systémes de reference temps-espace UMR8630/CNRS, 115-121.

Varga, P., Groten, E., Satori, G., Zavoti, J., 2005. The rotation vector of the Earth and the global temperature, Geophysical Research Abstracts of the European Geosciences Union, 7, 02441.

Varga P., 2006. Temporal variation of geodynamical properties due to tidal friction, J. Geodyn., 41, 140-146.

Verhoogen J., 1980: Energetics of the Earth, University of California, National Academy of Science.

Vespe, F., G., Bianco, M., Fermi, C., Ferraro, A., Nardi, C., Sciarretta, 2000. The Italian GPS Fiducial Network: Services and Products, J. Geodyn., 30, 327-336.

Vigny, C., *et al*., 1991. The Driving Mechanism of Plate Tectonics, Tectonophysics, 187, 345-360.

Vine, F. J., 1966. Spreading of the ocean floor: new evidence, Science, 154, 1405–1415.

Vine, F. J., and D. H. Matthews, 1963. Magnetic anomalies over oceanic ridges, Nature, 199, 947–949.

Vlaar, N. J. and Wortel, M. J. R., 1976. Lithospheric aging, instability and subduction, Tectonophysics, 32, 331-351.

Von Kármán, T., and Biot , M. A., 1951. Metodi matematici nell'ingegneria, Einaudi edition, in Italian.

Walter M.J., Trønes R.G., 2004. Early Earth differentiation, Earth and Planetary Science Letters, 225, 253-269

Wang Q.-L. Chen Y.-T. Cui D.-X., Wang W.-P. and Liang W.-F., 2000. Decadal correlation between crustal deformation and variation in length of day of the Earth, Earth Planets Space, 52, 989–992.

Ward, S., 1994. Constraints on the seismotectonics of the central Mediterranean from very long baseline interferometry, Geophys. J. Int., 11, 441– 452.

Wahr, J. M., 1988. The Earth's rotation, Ann. Rev. Earth Planet. Sci., 16, 231-249.

Wegener, A., 1915. Die Entstehung der Kontinente und der Ozeae: Samml. Vieweg, Braunschweig, 23, 1-94.

Weil, A. B., 1996. Plate Driving forces and tectonic stress, http://www.umich.edu/~gs265/tecpaper.htm, Seminar of the University of Michigan.

Wessel, P., Smith, W. H. F., 1995. *The Generic Mapping Tools (GMT) version 3.0*. Technical Reference & Cookbook, SOEST/NOAA.

Williams, S. D. P., 2003. The effect of coloured noise on the uncertainties of rates estimated from geodetic time series, J. Geodesy, 76, 483-494.

Williams, S. D. P., Y., Bock, P., Fang, P., Jamason, R. M., Nikolaidis, L., Prawirodirdjo, M., Miller, D. J., Johnson, 2004. Error analysis of continuous GPS position time series, J. Geophys. Res., 109.

Wilson, J.T., 1963. A possible origin of the Hawaiian Islands, Canadian Journal of Physics, 41, 863-870.

Wilson, J.T., 1965. A new class of faults and their relation to continental drift, Nature, 207, 343-347.

Wilson, J.T., 1973. Mantle plumes and plate motions., Tectonophysics, 19, 149–164.

Wilson, M., 1993. Plate-moving Mechanisms: Constraints and Controversies, Journal of the Geological Society, 150, 923-926.

Yoder, C. F., Williams, J. G., and Parke, M. E., 1981. Tidal Variations of Earth Rotation, J. Geophys. Res., 86, 881–891.

Ziegler, P.A., 1993. Plate-moving Mechanisms: their Relative Importance, Journal of Geological Society, 150, 927-940.

Zschau, J., 1983. Rheology of the Earth's mantle at tidal and Chandler Wobble periods, Proc. Ninth Int. Symp. Earth Tides, New York, 1981, Kuo, J. T. (ed.), Schweitzerbart'sche Verlagsbuchhandlung, Stuttgart, 605–630.

List of Tables

List of Figures

Internet sites

ASI	Agenzia Spaziale Italiana	http://www.asi.it/
DoD	U.S. Department of Defense	http://www.defenselink.mil/
EPN	EUREF Permanent Network	http://www.epncb.oma.be/
ESA	European Space Agency	http://www.rssd.esa.int/
EUREF	European Reference Frame	http://www.euref-iag.net/
IDS	International DORIS Service	http://ids.cls.fr/
IERS	International Earth Rotation and Reference Systems Service	http://www.iers.org/
IERS EOP PC	IERS Earth Orientation Parameters Paris Center	http://hpiers.obspm.fr/eop-pc/
IGS	International GNSS Service for Geodynamics	http://igscb.jpl.nasa.gov/
ILRS	International Laser Ranging Service	http://ilrs.gsfc.nasa.gov/
ITRF	International Terrestrial Reference Frame	http://itrf.ensg.ign.fr/
IVS	International VLBI Service for Geodesy and Astrometry	http://ivscc.gsfc.nasa.gov/
JPL	Jet Propulsion Laboratory of the California Institute of Technology	http://www.jpl.nasa.gov/
NEIC	National Earthquake Information Center	http://earthquake.usgs.gov/regional/neic/
RING	Rete Integrata Nazionale GPS	http://ring.gm.ingv.it/
SLR	Satellite Laser Ranging	http://ilrs.gsfc.nasa.gov/
UNAVCO	University NAVSTAR Consortium	http://www.unavco.org/

Acronims

AAM	Atmospheric Angular Momentum
AGU	American Geophysical Union
AM	Absolute Model
APKIM	Actual Plate KInematic and deformation Model
ARE	Austrian Reference Extended
ASI	Agenzia Spaziale Italiana
BIH	Bureau International de l'Heure
CAM	Core Angular Momentum
CERGOP	Central European Research Geodynamic Project
CIO	Conventional International Origin
CRF	Celestial Reference Frame
CRS	Celestial Reference System
CTP	Conventional Terrestrial Pole
DORIS	Doppler Orbitography and Radio-positioning Integrated by Satellites
EOP	Earth Orientation Parameters
EPN	EUREF Permanent Network
ESA	European Space Agency
EUREF	EUropean REference Frame
GIA	Glacial Isostatic Adjustment
GLONASS	GLObal NAvigation Satellite System
GNSS	Global Navigation Satellite Systems
GPS	Global Positioning System
GSRM	Global Strain Rate Model
HAM	Hydrological Angular Momentum
HSRF	Hotspot Reference Frame
HS	HotSpot
ICRS	International Celestial Reference System
ICRF	International Celestial Reference Frame
IDS	International DORIS Service
IERS	International Earth Rotation and Reference Systems Service
IGFN	Italian GPS Fiducial Network

IGS	International GPS Service
ILRS	International Laser Ranging Service
INGV	Istituto Nazionale di Geofisica e Vulcanologia
ITRF	International Terrestrial Reference Frame
ITRS	International Terrestrial Reference System
IVS	International VLBI Service for Geodesy & Astrometry
JPL	Jet Propulsion Laboratory
LLR	Lunar Laser Ranging
LOD	Length Of Day
LVZ	Low Velocity Zone
NASA	National Aeronautics and Space Administration
NEIC	National Earthquake Information Centre
NNR	No Net Rotation
NUVEL	Northwestern University VELocity model
OAM	Oceanic Angular Momentum
OLG	Observatory Lustbuehel Graz
PB	Plate Boundary
REGAL	REGional ALpine
REVEL	REcent VELocity model
RING	Rete Integrata Nazionale GPS
RM	Relative Model
SLR	Satellite Laser Ranging
SINEX	Software INdependent EXchange
SOPAC	Scripps Orbit and Permanent Array Center
TRF	Terrestrial Reference Frame
TRS	Terrestrial Reference System
UT	Universal Time
VLBI	Very Long Baseline Interferometry
WGS84	World Geodetic System 1984

Acknowledgments

I am arrived now at the acknowledgments section with the clear feeling that the conclusion of my thesis does not represent the end of an intellectually exciting period; indeed, I consider it a step ahead for future works and constructive contacts with truly interesting persons and colleagues.

I wish to express all my gratitude and admiration to Carlo Doglioni, my dear advisor and friend, whose unconventional sight and contagious enthusiasm have been a thoughtful and pleasant guidance of this work.

Since the beginning of my Ph.D. research, in 2005, I have had contacts with many people, who have helped and supported me in different ways. In particular, I am indebted with Mattia Crespi, Marco Cuffaro, Roberto Devoti, Giuliano Panza, Grazia Pietrantonio and Peter Varga, from their scientific inputs I have learnt so much.

A special thank is due to Maurizio Battaglia and Fernando Sansò, they have exerted all their patience to revise my thesis, giving useful suggestions to its improvement.

Yet, I remember the helpful discussions or e-mail exchanging with Riccardo Barzaghi, Christian Bizouard, Alessandra Borghi, Giancarlo D'Agostino, Veronique Dehant, Paola De Michelis, Rita Di Giovambattista, Bob Engdahl, Gillian Foulger, Richard Gordon, Robert King, Korneè Kreemer, Sonny Mathews, Vadim Milyukov, Riccardo Riva, Roberto Sabadini and Antonio Villaseñor.

I am also grateful to all the persons working on GPS permanent networks and data bank maintenance (ARE, ASI, EUREF, NASA, REGAL, RING, SOPAC) and many Italian institutions, universities and agencies; a conspicuous part of this research is based on their work.

In the end, the last thought is for my father, uncommon example of goodness, whose passion for life, mountains and physics has become also my passion.